

# Real-Time Simulation of a Microgrid System with Distributed Energy Resources

By  
Onyinyechi Nzimako

A thesis submitted to  
the Faculty of Graduate Studies  
of the University of Manitoba  
in partial fulfilment of  
the requirements for the degree of  
Master of Science

Department of Electrical and Computer Engineering  
Faculty of Engineering  
University of Manitoba  
Winnipeg, Manitoba

August 2015

© Copyright  
2015, Onyinyechi Nzimako

# Abstract

Microgrids are local groups of electricity generation, storage and loads that can operate in parallel with the grid or autonomously as a power island. Accurate and detailed microgrid simulation models are required for studying the operation, control and protection issues related to microgrids.

A real-time simulation model of a medium voltage microgrid with distributed energy resources (DERs) was developed using the RTDS™ real-time digital simulator. The DERs in this microgrid include a diesel generator, a photovoltaic (PV) system, and a doubly-fed induction generator (DFIG) wind turbine system. The average-value models for the PV and DFIG power electronic interfaces were developed to reduce the hardware requirements on the RTDS. The steady state and transient response of the microgrid when in the grid-connected and islanded modes of operation was shown to give satisfactory performance. The microgrid was interfaced to a protection relay to demonstrate hardware in the loop simulations.

# Acknowledgments

I would like to thank Dr. Athula Rajapakse for his invaluable guidance throughout the duration of my graduate studies.

I would like to thank RTDS Technologies Inc. for the hardware and software resources as well as the engineering work experience, which have been instrumental factors to the completion of this thesis.

I would like to thank Dr. Lidula Arachchige for discussing microgrid concepts and simulations with me at the initial phase of the research. I also would like to thank Yue Chen from RTDS Technologies Inc. for taking her time to discuss protection concepts with me.

I would like to sincerely thank my family and friends for encouraging me to complete this graduate program. I am truly humbled and blessed for all your support, especially from my amazing twin sister Oluchi who inspires me to keep learning and growing in all areas of life. I am deeply indebted to my parents, Cliff and Chinwe Nzimako for their unwavering love and support throughout my undergraduate and graduate studies in Canada.

# Dedication

My thesis is dedicated to my husband Ikenna Durunna who goes above and beyond to support me in all my endeavors. Thank you for all the encouragements and dedication you showed during this thesis. I also dedicate this work to our son, Muna who gives us a reason to live every day with love and joy.

# Contents

## Front Matter

Acknowledgements.....	i
Dedication.....	ii
Contents .....	iii
List of Tables.....	vi
List of Figures .....	vii
List of Symbols .....	xiv
List of Abbreviations .....	xix
<b>1 Introduction</b>	<b>1</b>
1.1 Background and Motivation.....	1
1.2 Research Objectives.....	4
1.3 Thesis Organization .....	5
<b>2 Literature Review</b>	<b>6</b>
2.1 Introduction .....	6
2.2 Definitions and Concepts .....	6
2.3 Microgrid Stability and Control.....	7
2.4 Microgrid Protection.....	9
2.5 Microgrid Islanding .....	11
2.5.1 Local Islanding Detection Techniques .....	12
2.5.2 Remote Detection Islanding Techniques .....	13
2.6 Synchronization of Microgrids .....	14
2.7 Voltage unbalance in Microgrids .....	15
2.8 Simulation Tools for Microgrid Studies.....	17
2.8.1 Real-Time Digital Simulation for Microgrid Studies .....	18

2.9	Concluding Remarks .....	25
<b>3</b>	<b>Modeling of Distributed Energy Resources</b>	<b>26</b>
3.1	Introduction .....	26
3.2	Diesel Generator Model.....	26
3.2.1	Synchronous Generator Model .....	27
3.2.2	Modeling the Diesel Engine and Speed Governor .....	29
3.2.3	Modeling the Excitation System .....	32
3.2.4	Modeling the Power System Stabilizer .....	34
3.2.5	Simulation of the Diesel Generation System.....	36
3.3	Photovoltaic Energy System Model .....	38
3.3.1	PV Array Model.....	39
3.3.2	Modeling the PV System Power Converter.....	44
3.3.3	Modeling the PV Control System .....	48
3.3.4	Simulation of the PV System .....	57
3.4	Wind Energy System Model.....	62
3.4.1	Doubly Fed Induction Generator (DFIG).....	63
3.4.2	Modeling the DFIG control system .....	68
3.4.3	Simulation of the DFIG Wind System. ....	76
3.5	Conclusions .....	80
<b>4</b>	<b>Average Value Modeling of Voltage Source Converters</b>	<b>81</b>
4.1	Introduction .....	81
4.2	Average Value Models .....	81
4.3	AVM in the $dq$ reference Frame.....	83
4.4	Comparing AVM and Detailed VSC .....	85
4.4.1	Comparing the AVM and Full VSC for the DFIG system.....	86
4.4.2	Comparing the AVM and Full VSC for the PV system .....	90
4.5	Conclusions .....	93

<b>5</b>	<b>Microgrid System Analysis</b>	<b>94</b>
5.1	Introduction .....	94
5.2	Microgrid Structure .....	94
5.2.1	Load shedding scheme .....	96
5.2.2	Implementation of microgrid in RTDS .....	98
5.3	Grid connected operation of microgrid.....	100
5.3.1	Microgrid transient response in grid-connected mode .....	101
5.4	Microgrid Operation in islanded mode .....	104
5.4.1	Case A: Change from Grid-connected to Islanded operation	104
5.4.2	Case B: Temporary fault in islanded mode.....	108
5.5	Microgrid Synchronization.....	110
5.6	Interfacing a Physical Relay with the Microgrid System .....	115
5.6.1	Interface between the microgrid model and the relay .....	116
5.7	Conclusions .....	123
<b>6</b>	<b>Conclusions and Future Work</b>	<b>124</b>
6.1	Conclusions .....	124
6.2	Future Work .....	126
	<b>References</b>	<b>128</b>

# List of Tables

Table 2-1 Synchronization Limits [15].....	15
Table 3-1 Synchronous machine parameters [31] .....	28
Table 3-2 Excitation system parameters .....	33
Table 3-3 Power system stabilizer parameters.....	36
Table 3-4 Comparing efficiency of commercial silicon solar cells [48] .....	40
Table 3-5 PV Array Parameters .....	57
Table 3-6 Proportional and Integral gains for PV controllers.....	54
Table 3-7 DFIG RSC and GSC Control Parameters.....	76
Table 3-8 DFIG System Parameters [31].....	77
Table 5-1 Transmission line data .....	96
Table 5-2 Load Data .....	97
Table 5-3 Load shedding criteria .....	97
Table 5-4 Per RMS Line phase voltages on bus 1-7 of the microgrid.....	100
Table 5-5 Average LL rms voltages and % Voltage unbalance .....	101

# List of Figures

Figure 1-1 Network benchmarks for DER integration [1].....	2
Figure 2-1 Islanding Detection Techniques [17] .....	12
Figure 2-2 Local islanding detection techniques [17].....	12
Figure 2-3 Remote islanding detection techniques [17] .....	14
Figure 2-4 Norton equivalent of an electrical circuit using the EMTP Dommel Algorithm [32].....	19
Figure 2-5 Microgrid simulation using the RTDS .....	22
Figure 2-6 Screen shot of RSCAD Draft Module [31] .....	23
Figure 2-7 HIL testing using the Real Time Digital Simulator [31].....	23
Figure 3-1 Diesel Generating System in RSCAD/Draft .....	27
Figure 3-2 Block diagram model of diesel engine and speed governor .....	30
Figure 3-3 Diesel engine and speed governor model in RSCAD/Draft.....	31
Figure 3-4 Block Diagram of Excitation System.....	33
Figure 3-5 Excitation System in RSCAD/Draft.....	34
Figure 3-6 Block diagram of the power system stabilizer. ....	34
Figure 3-7 Power System Stabilizer in RSCAD\Draft .....	36
Figure 3-8 Diesel generator real power, per unit angular speed, and mechanical torque (Tm) .....	37
Figure 3-9 Diesel generator reactive power, terminal bus voltage and excitation field voltage.....	38
Figure 3-10 PV system modeled in RSCAD draft.....	39

Figure 3-11 PV Cell - Module - Array [49] .....	40
Figure 3-12 Practical model of a solar cell .....	41
Figure 3-13 I-V and P-V curve of a PV cell/module/array.....	42
Figure 3-14 Solar cell model with shunt resistance neglected.....	43
Figure 3-15 RSCAD PV Model [31] .....	44
Figure 3-16 Single stage PV converter topology .....	45
Figure 3-17 Dual stage PV converter topology .....	45
Figure 3-18 Single-Stage, Grid-connected PV system .....	46
Figure 3-19 3-phase, 2-level Voltage Source Converter .....	46
Figure 3-20 Small time step simulation of the VSC in RSCAD [31].....	47
Figure 3-21 Phase locked loop and $dq$ transform of AC side voltages and currents .....	50
Figure 3-22 Decoupled dq current control.....	50
Figure 3-23 Methods to obtain q current control reference .....	52
Figure 3-24 PV DC link voltage regulation and MPPT control .....	53
Figure 3-25 Maximum power point tracking techniques.....	55
Figure 3-26 Flowchart of incremental conductance algorithm.....	56
Figure 3-27 RSCAD Runtime for PV Simulation .....	57
Figure 3-28 I-V curves for different insolation at $T=25^0$ C .....	58
Figure 3-29 P-V curves for different insolation at $T=25^0$ C .....	58
Figure 3-30 Interfacing the PV array with the 2-level VSC in RSCAD.....	59
Figure 3-31 DC Bus voltage response to changing insolation.....	60
Figure 3-32 Increasing PV array power (DC and AC side) to increasing insolation .....	60
Figure 3-33 Grid response to varying solar insolation.....	61

Figure 3-34 Step Change in Load for PV voltage regulation .....	61
Figure 3-35 PV-grid PCC bus response to step change in load with and without voltage regulation. ....	62
Figure 3-36 DFIG wind energy system .....	63
Figure 3-37 Power coefficient curves ( $C_p$ ) vs tip speed ratio (TSR) ( $\lambda, \beta$ ) [31] .....	65
Figure 3-38 Two mass model of the wind turbine drive train .....	65
Figure 3-39 RSCAD Model of Wind Turbine and Drive Train [31] .....	66
Figure 3-40 DFIG Crowbar Circuit. ....	67
Figure 3-41 Wind system power-speed curves [68] .....	68
Figure 3-42 Pitch angle control.....	69
Figure 3-43 Optimal torque control for DFIG MPPT method.....	70
Figure 3-44 GSC voltages and currents .....	71
Figure 3-45 Grid side converter $dq$ current control .....	72
Figure 3-46 Phase locked loop of grid three phase voltages .....	72
Figure 3-47 dq transform of GSC AC voltages and currents.....	72
Figure 3-48 Firing pulse generation for GSC using SPWM.....	72
Figure 3-49 Rotor side converter voltages and currents .....	73
Figure 3-50 ABC-dq RSC.....	74
Figure 3-51 RSC dq current control.....	75
Figure 3-52 RSC Firing pulse generation using SPWM.....	76
Figure 3-53 DFIG System in RSCAD [31] .....	77
Figure 3-54 Pitch angle response to wind speed ramp .....	78

Figure 3-55 Power and speed response of DFIG wind system to ramp change in wind speed. .....	79
Figure 3-56 Grid power response to ramp change in wind speed.....	79
Figure 4-1 Switching state representation.....	82
Figure 4-2 AVM for PV VSC.....	84
Figure 4-3 AVM for DFIG VSC.....	85
Figure 4-4 Comparing the AVM and Fully Switched DFIG VSC .....	86
Figure 4-5 GSC and RSC AVM voltage source representation in RSCAD/Draft .....	86
Figure 4-6 DC Bus link for the AVM.....	87
Figure 4-7 DFIG Real and Reactive Power .....	88
Figure 4-8 DFIG Speed.....	88
Figure 4-9 DC Bus Voltage .....	88
Figure 4-10 Grid side converter dq voltage references.....	89
Figure 4-11 Rotor side converter dq voltage references.....	89
Figure 4-12 q current reference for RSC and d current reference for GSC .....	89
Figure 4-13 Switching frequency dynamics in DFIG Full VSC.....	90
Figure 4-14 Simulation case for comparing the FULL and AVM VSC for the PV system .....	91
Figure 4-15 Real power output and DC bus voltage of FULL and AVM model to three phase line to ground fault.....	91
Figure 4-16 Per unit voltage at PV-grid point of connection and reactive power of FULL (black) and AVM(red) model to three phase line to ground fault. ....	92

Figure 4-17 dq modulation indices response to three phase line to ground fault with FULL (black) and AVM (red) VSC models .....	92
Figure 4-18 Real and Reactive power at grid side response to three phase line to ground fault with FULL (black) and AVM (red) VSC models.....	93
Figure 5-1 Microgrid structure.....	95
Figure 5-2 RSCAD Runtime model of microgrid with the DERs .....	98
Figure 5-3 Processor assignment using fully switched VSC models .....	99
Figure 5-4 Processor assignment using the average-value VSC models .....	99
Figure 5-5 Line to Line Voltages response to 3 Phase line to ground fault at BUS6.....	102
Figure 5-6 Fault currents at Bus 6 with a 5 cycle, 0.1 ohm line to ground fault with no DERs (Blue), DERs with full VSC model (Black) and DERs with AVM models(Red) in the microgrid.....	102
Figure 5-7 Real and reactive power supplied by the individual DERs and consumed for the AVM (black) and FULL (red) VSC converter models during .....	103
Figure 5-8 Microgrid frequency response to 3PH, line to ground fault at BUS 6 for the AVM(black) and FULL VSC (red) converter DERs.....	104
Figure 5-9 Microgrid Frequency before and after islanding with the AVM VSC (black) and FULL VSC Models(Red). Load shedding is not activated.....	105
Figure 5-10 Total real and reactive power supplied by the GRID and DERs and consumed by the LOADS for both the AVM(black) and FULL (red) VSC converter models. ....	105
Figure 5-11 Per Unit average RMS Bus Voltage and Load Response on Bus 5-7 for AVM (Black) and Full VSC Model (Red) .....	106

Figure 5-12 Per Unit average RMS Bus Voltage and Load Response on Bus 1-4 or AVM (Black) and Full VSC Model (Red) .....	107
Figure 5-13 Voltage unbalance of the islanded microgrid using the FULL(black) and AVM(red) VSC Converter models for the Solar and DFIG DERs. ....	108
Figure 5-14 Fault current level for islanded microgrid with line to ground fault at BUS 6 using the AVM (black) and FULL(red) VSC model of the DFIG and SOLAR DERs..	109
Figure 5-15 Microgrid Frequency during islanded fault condition activates load shedding .....	109
Figure 5-16 Response of total real and reactive power supplied by the DERs and consumed by the LOADS for both the AVM(black) and FULL (red) VSC converter models during temporary fault in islanded microgrid.....	110
Figure 5-17 RTDS Synchro-check element for microgrid synchronization.....	111
Figure 5-18 Voltage and phase difference between microgrid and grid at PCC after islanding using the FULL (red) and AVM(black) converter based DERs, .....	112
Figure 5-19 Voltage difference at Microgrid PCC after turning on the switched shunt capacitors .....	112
Figure 5-20 Phasor diagram representation of microgrid (blue) and grid (red) bus voltages .....	113
Figure 5-21 Reconnecting the microgrid with the grid.....	113
Figure 5-22 Microgrid frequency synchronized to grid frequency power with the AVM(black) and FULL(red) VSC converter based models.....	114
Figure 5-23 Grid, Load and DER power before and after resynchronisation with the AVM(black) and FULL(red) VSC converter based models.....	115

Figure 5-24 Interface between Microgrid System and a Physical Relay .....	116
Figure 5-25 Measured primary RMS voltage and RMS current signals in the relay .....	117
Figure 5-26 Measured primary RMS voltage (kV) and RMS current (A) in the RTDS simulation.....	117
Figure 5-27 Overcurrent Element of Protection Relay .....	118
Figure 5-28 Grid Connected Mode: Phase A Line to Ground Fault Current.....	119
Figure 5-29 Fault Detection in Relay.....	119
Figure 5-30 Fault and relay trip signal in simulated system grid connected operation ..	120
Figure 5-31 CT currents in the Relay .....	120
Figure 5-32 CT currents in the RTDS.....	121
Figure 5-33 Fault Current - Islanded Mode .....	122
Figure 5-34 Fault and relay trip signal in islanded operation .....	122
Figure 6-1 Diesel Generator with associated pollution (blackened walls) .....	127

# List of Symbols

$\rho$	Air density
$\omega_{\text{ref}}$	Angular speed reference
$\omega$	Angular speed
$\delta$	Compensation angle
$\lambda$	Flux linkages
$\phi_m$	Phase compensation angle
$\theta_{\text{slip}}$	Slip angle
$\theta_s$	Stator angle
$\theta_r$	Rotor angle
$\tau_{\text{cc}}$	Current controller time constant
$\Delta T$	Simulation Time Step
$\beta$	Pitch angle
$a$	Diode ideality factor
$A_f$	Frequency modulation index
$A_m$	Amplitude modulation index
$B_0$	Zero sequence susceptance
$B_p$	Positive sequence susceptance
$C_p$	Blade power coefficient
$E_{\text{field}}$	Exciter field voltage
$f$	Frequency

fresonant	Resonant frequency
fs	Rated stator frequency
fswit	Switching frequency of voltage source converter
G	Solar insolation
H	inertia constant
ia	Alternating current in phase A
ib	Alternating current in phase B
ic	Alternating current in phase C
id	D-axis direct current
Impp	Maximum power point current
Io	Diode saturation current
Iph	Photocurrent
iq	Q-axis direct current
Isc	Short circuit current
k	Boltzmann factor
Ka	Amplifier gain
Kd	First order transfer fuction
Kdgov	Governor derivative gain
Ke	Exciter gain
Ki	Integral gain
ki_cc	Current controller integral gain
Kigov	Governor integral gain
Kp	Proportional gain

$k_{p\_cc}$	Current controller proportional gain
$K_{pgov}$	Governor proportional gain
$K_{pss}$	Power system stabilizer gain
$L$	Inductance
$L_{eq}$	Equivalent inductance
$m_d$	D-axis modulation magnitude
$m_q$	Q-axis modulation magnitude
$n_p$	Number of parallel connected cells
$N_p$	Number of parallel connected modules
$n_s$	Number of series connected cells
$N_s$	Number of series connected modules
$P$	Rated real power
$p_f$	Number of field poles
$q$	Electronic charge
$R$	Droop factor
$R$	Resistance
$R_a$	Stator resistance
$R_s$	Series resistance
$R_{sh}$	Shunt resistance
$R_w$	Wind turbine blade length
$S$	Rated apparent power
$T_a$	Amplifier time constant
$T_{cell}$	Cell Temperature

$T_d$	Engine time delay
$T_{d1}$	First order time constant
$T_{do}'$	Unsaturated transient open time constant d axis
$T_{do}''$	Unsaturated sub transient open time constant d axis
$T_e$	Exciter time constant
$T_m$	Maximum torque constant
$T_{max}$	Maximum torque constant
$T_{min}$	Minimum torque constant
$T_{qo}'$	Unsaturated transient open time constant q axis
$T_{qo}''$	Unsaturated sub transient open time constant q axis
$T_r$	Voltage transducer time constant
$T_w$	Washout time constant
$V_{amax}$	Maximum voltage of amplifier
$V_{amin}$	Minimum voltage of amplifier
$V_{DC}$	DC Bus voltage
$V_{mpp}$	Maximum power point voltage
$V_N$	Negative DC node voltage
$V_{oc}$	Open circuit voltage
$V_P$	Positive DC node voltage
$V_{prim}$	Primary voltage
$V_{pu}$	Per unit terminal voltage
$V_{ref}$	Terminal voltage reference
$V_{rmax}$	Maximum voltage of voltage regulator

$V_{rmin}$	Minimum voltage of voltage regulator
$V_{sec}$	Secondary voltage
$V_t$	Diode thermal voltage
$V_w$	Wind speed
$X$	Reactance
$X_a$	Stator leakage reactanc
$X_d$	Unsaturated reactance d axis
$X_d'$	Unsaturated transient reactance d axis
$X_d''$	Unsaturated sub-transient reactance d axis
$X_q$	Unsaturated reactance q axis
$X_q'$	Unsaturated transient reactance q axis
$X_q''$	Unsaturated sub transient reactance q axis

# List of Abbreviations

AC	Alternating Current
ATP	Alternative Transient Program
AVM	Average Value Model
DC	Direct Current
DERS	Distributed Energy Resources
DFIG	Doubly Fed Induction Generator
EMTP	Electromagnetic Transient Program
HDUT	Hardware Device Under Test
HIL	Hardware In The Loop
IGBT	Insulated Gate Bipolar Transistor
LVUR	Line Voltage Unbalance Rate
PCC	Point Of Common Connection
PID	Proportional Integral Derivative Controller
PLL	Phase Locked Loop
PSCAD	Power System Computed Aided Design
PSS	Power System Stabilizer
PV	Photovoltaic
PVUR	Phase Voltage Unbalance Rate
RTDS	Real Time Digital Simulator
SPWM	Sinusoidal Pulse Width Modulation
STC	Standard Test Conditions
VSC	Voltage Source Converter
VUB	Voltage Unbalance

# Chapter 1

## Introduction

### 1.1 Background and Motivation

The conventional power grid with centralized generation is evolving to include comparatively small-scale Distributed Energy Resources (DERs) and loads connected as microgrids [1]. Microgrids are local groups of electricity generation, energy storage, and loads that can be controlled to operate in parallel with the power grid or autonomously as a power-island [2]. The technical and economic benefits of microgrids include increasing use of renewable energy and distributed energy resources to reduce carbon emissions from fossil fuel energy sources, increased power supply reliability during power outages, increased revenue to operators from energy sales as well as ancillary grid services, and accessible, affordable energy to remote areas where power grid infrastructure is non-existent [3]. Recent experience has shown that microgrids can help to supply electricity to critical facilities such as health care and telecommunication, and grid restoration during natural disasters that cause large-scale damages to power transmission grids [4].

In [1], it is predicted that DERs will constitute 30 percent of the energy market by 2030. The increasing penetration of DERs changes the dynamics and operation of the traditional grid. The power provided by the integration of DERs must be delivered to consumers within acceptable limits of current, voltage and frequency to ensure power quality and reliability. The simple methods used for voltage control and protection of traditional radial distribution systems will no longer be adequate as power flow directions are changed with the availability of DERs or with fluctuations in the energy sources such as wind and solar radiation. Thus the integration of DERs using the microgrid concept requires the development of intelligent controllers and new protection techniques. Therefore, accurate simulation models of microgrids are needed to study the impact of DER on the network and the efficacy of new control and protection systems. The CIGRE Task Force C6.04.02 was established to address the need for a commonly accepted basis for testing methods and techniques of DER integration [1]. The Task Force developed several benchmark networks at different levels for DER integration studies. The relationship between the different benchmark networks is shown in Figure 1-1 [1].

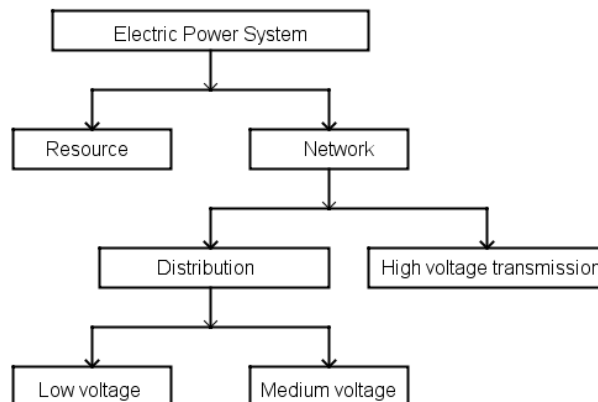


**Figure 1-1 Network benchmarks for DER integration [1]**

Examples of DER integration studies that can be performed using such benchmark networks include [1, 5] :

- Power electronic topologies for DER integration;
- DC bus voltage control options;
- Maximum power tracking;
- Islanding;
- Interaction of control of two parallel DER units;
- Impact of various DERs on the power flow, voltage profile, reliability, stability and power quality;
- Methodologies and techniques for designing control, protection and energy management systems.

Models of the CIGRE bench mark distribution systems have been implemented on several offline simulation tools [6]. Such models have been used for the above mentioned DER integration studies. The importance of modeling microgrids in real-time simulators is the ability to interface real hardware control and protection equipment to test their operation in real-time operating conditions. Additionally real-time simulators offer faster speed of computation as the solution of the overall network is completed in one simulation time step compared to several minutes or longer in offline simulators. Therefore the motivation for this research is to model a microgrid system based on the CIGRE medium voltage (MV) distribution network on a real-time digital simulator.

## 1.2 Research Objectives

The objective of the research is to develop a real-time simulation model of a microgrid system to study DER integration at the distribution level. Developing a real-time microgrid system model will allow accurate and reliable testing of protection and control devices under actual operating conditions. To fulfill the research objectives, the following tasks will be accomplished in this thesis:

- Literature review on microgrids with a focus on the technical issues facing the interconnection of DERs to the distribution network.
- Literature review on the modeling and analysis of DERs and their associated controls and power electronic systems.
- Development of detailed models of several DERs including a diesel generator, PV system, and a DFIG wind energy system.
- Development of average-value models for the PV and DFIG converter systems to reduce the hardware resources required for real-time simulation.
- Implementation of a complete real-time simulation model of a microgrid system with DERs based on the CIGRE C6.04.02 benchmark North American MV distribution network using the RTDS™ simulator.
- Analysis of the steady state and transient response of the microgrid system when in grid-connected and autonomous operation under different operating scenarios.
- Interfacing a protective relay with the microgrid system in a hardware in the loop simulation.

## 1.3 Thesis Organization

Chapter 1 provides a background introduction to the thesis as well as the motivation and objectives of the research.

Chapter 2 provides a literature review of the definitions and concepts of microgrids as well as technical issues facing microgrid applications. A discussion on real-time digital simulation is also provided.

Chapter 3 describes the modeling of the DERs and their control systems.

Chapter 4 describes the modeling of the average-value models (AVM) for the converter interfaced DERs and shows how using AVM reduces the amount of hardware resources but at a trade-off of simulation details.

Chapter 5 describes the microgrid structure and provides a discussion on the challenges of modeling distribution networks using a real-time digital simulator. An analysis of the real-time steady state and transient response of the microgrid system when in grid-connected and islanded operation is provided. A hardware in the loop simulation with the microgrid system and a protection relay is implemented and discussed.

Chapter 6 gives the conclusions and future work.

# Chapter 2

## Literature Review

### 2.1 Introduction

This chapter provides a literature review of the definitions and concepts of microgrids as well as technical challenges facing microgrid implementation. This chapter also includes a brief discussion on the RTDS, an EMTP-based real-time digital simulator.

### 2.2 Definitions and Concepts

Microgrids are localized groups of electricity generation, energy storage, and loads typically located downstream at the low (LV) or medium voltage (MV) distribution level. Microgrids can be controlled to operate in parallel with a conventional centralized grid or autonomously as a power island [2]. A power island is defined as a portion of the distribution network that has been electrically isolated from the main utility but is kept energized by the operation of the local DERs [7]. The DERs used in microgrid applications

include wind, solar, synchronous generators driven by diesel, steam or hydro turbines, combined heat and power plants, fuel cells, micro-turbines and engine-generator sets operated with biofuels. Microgrids can provide additional voltage support to the transmission system, reduce losses on distribution networks, and improve overall power supply reliability [8]. In addition, microgrids can be used to provide back-up power supply to critical loads during grid fault events.

Microgrids are a key concept towards the development of smart power systems of the future where large conventional fossil fueled power generation plants will be replaced with reduced scale DERs situated closer to the demand side. Microgrids are rapidly gaining interest in campus environments, military operations, community and utility systems, commercial and industrial markets, and remote/off-grid settings. An overview of existing microgrid architectures and designs around the world is provided in [9].

Despite the benefits of the microgrid concept, its implementation is faced with significant technical challenges due to its relative novelty when compared to the conventional power grid. The following sections provide a literature review of some of the technical challenges faced with microgrid applications. A discussion on simulation models and tools for microgrid studies is also provided.

## **2.3 Microgrid Stability and Control**

An important aspect in microgrid control is maintaining system stability when in grid-connected and islanded modes under different operating conditions. The integration of DERs changes the unidirectional power flow nature of traditional distribution networks

affecting the operation of the control and protection devices. When in grid-connected operation, disturbances on the utility side can adversely affect the operation of the DERs in the microgrid. For enhanced stability, electrical isolation between the utility and the microgrid is required to protect equipment and personnel [10].

Microgrid control must regulate the power, voltage, and frequency when in grid-connected or islanded operation within specified thresholds of power quality and reliability. Microgrid control should transition from grid-connected mode to autonomous mode with minimum voltage and frequency fluctuations. Load shedding schemes must be designed for cases where the power available from the DERs is insufficient to supply the loads in the islanded microgrid or when fault events cause the voltage and currents to rise to levels above the equipment ratings. Load shedding control should operate rapidly to restore the power balance in the microgrid to avoid voltage and frequency collapse. After the system is restored, the microgrid control should seamlessly reconnect the microgrid with the main utility by ensuring the voltage, frequency and phase angle of the microgrid and utility meet synchronization and voltage balancing requirements at the PCC.

The microgrid control is done using a central controller (CC) and microsource controller (MC) [11]. The role of the CC is to coordinate the overall microgrid control and protection functions [11]. Typically, the control objectives of the CC are achieved by using real and reactive power control during grid-connected operation and voltage and frequency control during islanded operation [12]. In grid-connected operation, the CC should operate the microgrid in synchronism with the main grid. In islanded operation, the CC should coordinate the operation of load shedding controls to restore power balance in the microgrid [11].

Several MC and CC control strategies have been proposed in literature to improve the transient response of microgrids with different types of DERs. DERs are classified based on their dynamic response and power flow into inertial/non-inertial and dispatchable/non-dispatchable) systems [13]. Wind and solar systems are non-dispatchable/non-inertial as their power output largely depends on the environmental conditions and they are interfaced with power converters, which have low-inertia characteristics [13]. This is a major concern in grid-connected systems with renewables, as power fluctuations caused by changing environmental conditions could cause voltage and frequency instability. Properly designed voltage and frequency control as well as protection techniques have to be used by grid operators to mitigate these issues, increasing the cost and complexity of integrating large-scale, distributed grid-connected systems with renewable energy resources. Diesel generators are dispatchable/inertial DERs as their power output can be adjusted to a set reference point and they have high-inertia characteristics due to the presence of large rotating masses. Voltage, frequency, and angle droop control methods are commonly employed in microgrid control systems [10].

## 2.4 Microgrid Protection

A significant challenge facing microgrid applications is the impact on protection systems caused by DER integration. Traditional distribution protection schemes are based on fault current levels with no generation at the distribution substation. The integration of DERs changes the magnitude, duration and direction of the fault currents in the distribution network. The contribution to fault current levels depends on the size and type of DERs. Converter-interfaced DERs have a small contribution to fault current levels due to the current

limits of the converters control systems. DERs with synchronous generators contribute a continuous fault current level while DERs with induction generators contribute to the fault current levels in one or two cycles [14]. The change in the fault current level may cause the fault to go undetected by the protection devices or create nuisance tripping. Other technical impacts on distributed system protection caused by DER integration is discussed in [14]. The protection scheme should be designed to cover all possible operating scenarios and should clear fault events within the specified operating limits to avoid exceeding the current and voltage ratings of the connected DERs and loads. Protection devices for converter interfaced DERs must be designed to operate with low values of fault currents and high DC voltages. Traditional protection schemes such as overcurrent, differential, and impedance protection can be used for microgrids having synchronous generators or energy storage devices. However, traditional protection schemes have high non-detection probabilities due to the low levels of fault current contribution by converter interfaced DERs. To overcome these limitations, novel protection schemes based on symmetrical components as well as adaptive schemes based upon intelligent algorithms to adjust the protection settings have been proposed in literature [14]. However, this increases the complexity of the protection design and in some cases increases the detection time of the fault event as this could require the use of additional devices such as dedicated circuit breakers, fuses, reclosers, or advanced protection and communication schemes [14].

## 2.5 Microgrid Islanding

Islanding refers to the situation where the DERs continue to supply power to a portion of the distribution network even though that portion has been disconnected from the main utility. There are two types of islanding operation namely *intentional* and *unintentional* island operation [15]. Unintentional islands create a hazardous situation for equipment and service personnel who may be unaware that the DG has kept a portion of the lines and devices energized. Unintentional islands are required to be detected and disconnected from the main grid within two seconds of the islanding event [15]. Intentional islands could be used as backup power supply for critical loads such as hospitals or to improve the power quality and reliability of the distribution network. Fast and reliable microgrid islanding detection techniques are therefore required to avoid power instability, equipment damage, as well as injury to utility personnel. The main requirements of an islanding detection scheme is to differentiate between transients caused by normally occurring events such as faults, load switching, or equipment start up and transients caused as a result of loss of the main grid. It also needs to coordinate among the protection devices to avoid unnecessary tripping of the DERs [16]. The selection of the DER and grid parameters as well as the islanding detection and transition times depends on the type of DERs and their implemented control schemes [16]. Several standards such as IEEE 1547-2003 define requirements for islanding detection and transition times. Islanding detection techniques are classified as shown in Figure 2-1.

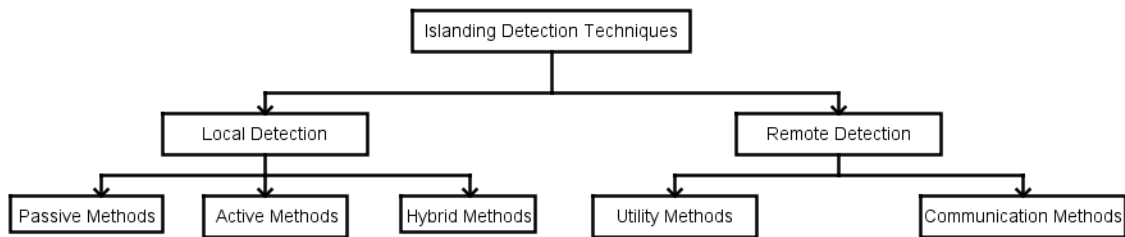


Figure 2-1 Islanding Detection Techniques [17]

### 2.5.1 Local Islanding Detection Techniques

Figure 2-2 shows the classification of local islanding detection techniques. Passive detection use measured deviations in the DER and grid parameters within specified limits from the steady operation to establish if an islanding event has occurred [17]. Passive techniques offer fast response to deviations and are simple to implement; however, their major drawback is the high probability of non-detection zones especially when the DER generation matches the load demand [17]. A modified passive technique using data mining and decision-tree classifiers to reduce the non-detection zone is discussed in [18].

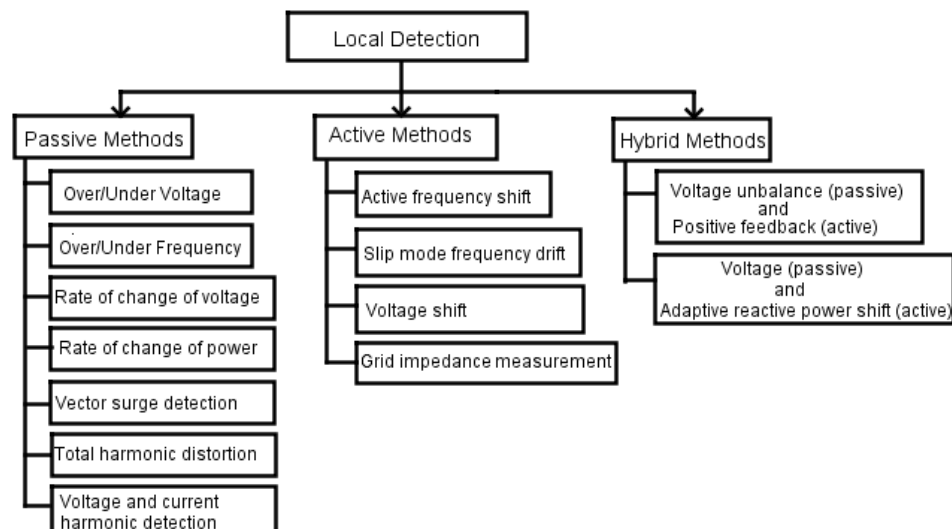


Figure 2-2 Local islanding detection techniques [17]

Active techniques detect islanding events by injecting disturbances to the power system and monitoring the system response [17]. The idea is that during islanding operation, the DERs in the island will have a different response to the injected disturbances than when in parallel operation with the power system [17, 18]. Active detection methods have a reduced non-detection zone compared to passive techniques; however, the detection time of active methods tends to be much slower than passive techniques. In addition, the injected disturbances create power quality issues in power networks with high integration of DERs [16]. Active methods are generally applied for converter-interfaced DER systems while a combination of passive methods are commonly used for rotating machine DER units [16]. Typically synchronous generator DER units employ over/under frequency, over/under voltage as well as directional relay protection schemes to detect islanding when the DER power output is lower than the load on the feeders as the, real and reactive power, voltage and frequency of the synchronous generator tend to vary rapidly when islanding occurs [16].

Hybrid methods combine passive and active techniques to detect islanding events. Typically they use passive methods to detect the islanding event and only inject disturbances after the islanding event is detected by the passive technique [17].

### **2.5.2 Remote Detection Islanding Techniques**

The remote islanding techniques rely on active communication between the DERs and the grid. Remote detection techniques have the highest probability of detecting islanding events with zero non-detection zones when DER generation matches the load demand.

However, a major drawback is that remote techniques are more complicated and expensive to implement than active and passive techniques and may not be economically viable in small to medium DER applications [17, 19]. Figure 2-3 shows the classification of remote detection islanding techniques [17].

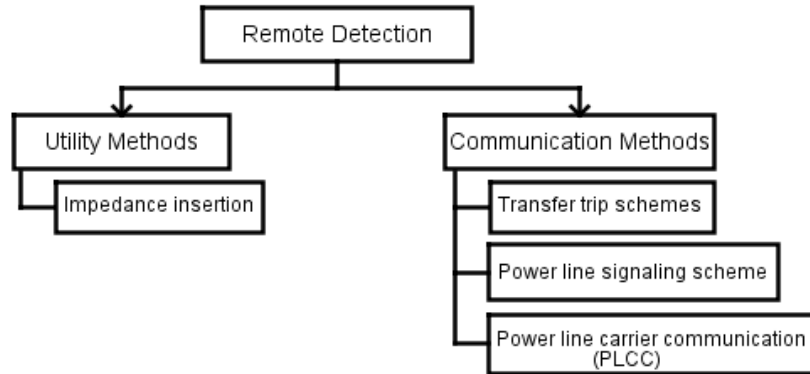


Figure 2-3 Remote islanding detection techniques [17]

## 2.6 Synchronization of Microgrids

Before an islanded microgrid is reconnected to the main grid its voltage, frequency, and phase angle must be matched to those of the grid network within specified limits to avoid transient instability caused by differences in the real and reactive power at the PCC. According to IEEE 1547.2-2008 the “*DR unit shall parallel with the Area EPS without causing a voltage fluctuation at the PCC greater than  $\pm 5\%$  of the prevailing voltage level of the Area EPS at the PCC*” [15].

Microgrid synchronization methods fall into three categories namely: (i) **active synchronization methods**, which use communication and control systems to exchange information between the micro-grid DERs and the main utility (ii) **passive synchronization**

*methods*, which use devices such as synchro-check relays to monitor the voltage, phase and frequency at the PCC, and (iii) *open-transition transfer* where the microgrid is re-connected to the main grid only after the DERs and loads in the microgrid have been de-energized [6]. Table 2-1 shows synchronization parameter limits defined by IEEE 1547-2003 for synchronous interconnection of an energized microgrid to the main grid [15].

Table 2-1 Synchronization Limits [15]

Aggregate rating of DER Units (kVA)	Frequency Difference ( $\Delta f$ , Hz)	Voltage difference ( $\Delta V$ , %)	Phase angle difference ( $\Delta\phi$ , °)
0-500	0.3	10	20
>500-1500	0.2	5	15
1500- 10000	0.1	3	10

## 2.7 Voltage unbalance in Microgrids

LV or MV distribution networks have uneven distribution of loads, which create voltage unbalance on the phases of the network. Voltage unbalance causes adverse effects on the equipment and loads in the network. For DERs using induction machines, unbalanced stator voltages cause unequal heating in the stator phase windings [20]. In converter-interfaced DERs, voltage unbalance creates uncharacteristic harmonics, which increases the heating losses in the power electronic switches. Unbalanced voltages and currents have to be properly mitigated within acceptable limits to avoid damage to components in the network. Several standards define the voltage unbalance in the network [21].

- The Institute of Electrical and Electronic Engineers (IEEE) defines the percentage phase voltage unbalance rate (PVUR) as [21]:

$$\%PVUR = \frac{|\Delta V_{average\_phase}|}{V_{average\_phase}} \quad (2.1)$$

- The National Electrical Manufacturers Association (NEMA) defines the percentage line voltage unbalance as [21]:

$$\%LVUR = \frac{|\Delta V_{average\_line}|}{V_{average\_line}} \quad (2.2)$$

- A widely accepted method that uses the negative and positive sequence RMS voltages to calculate the percentage voltage unbalance factor is given as [21].

$$\%VUF = \frac{\textit{negative sequence voltage}}{\textit{positive sequence voltage}} \quad (2.3)$$

IEEE Std.1547.2-2008 states that a voltage unbalance greater than 2.5-3% is significant enough to cause three-phase motors or other devices to overheat [22]. Methods to mitigate voltage unbalance include using SVCs, STATCOMs, energy storage devices, switched shunt capacitors, automatic load tap changing transformers, or voltage regulation using the reactive power capability of the DERs [6, 22, 23].

Due to increasing levels of DER integration, there is a growing interest to allow DERs to contribute to the voltage and reactive power regulation. Previous versions of the IEEE 1547.1 standard for DER integration required DERs to operate at a fixed power factor (typically unity power factor) without actively regulating the reactive power and subsequently the PCC voltage in the distribution network [23]. This stipulation is currently being reviewed and modified for future revisions of the IEEE 1547 DER integration standard. Several benefits of using the reactive power capability of DERs include reduced transmission line losses (which increases the system capacity), low voltage ride through during faults, and voltage unbalance mitigation [24, 25, 26]. Voltage regulation using the

reactive power capability of synchronous generators is achieved by controlling the reactive power output using a reactive droop characteristic on the high voltage transmission side or by regulating the terminal voltage at the low voltage machine terminals using an automatic voltage regulator [23]. Reactive power capability is achieved in wind and PV systems by either a reactive power dispatch or volt/var controllers [23].

The reactive power capability for DERs is specified at the PCC based on power factor requirements. Typically a power factor range of “*0.95 lead to lag at full rated power*” is specified for converter interfaced DERs [23]. For synchronous generators, the reactive power capability is typically specified at “*0.90 lagging power factor to 0.95 leading power factor*” to allow a voltage regulation range from 90-110% [23]. IEEE 1547.1 requires the power factor to be at or higher than 0.85 lead/lag [23].

## 2.8 Simulation Tools for Microgrid Studies

The discussed technical challenges associated with grid-integration of distributed energy resources using the microgrid concept can be studied using simulation tools with detailed models of power system components and their associated control and protection devices. In [27], a detailed review on mathematical models of hybrid renewable energy systems for a hydro-solar and wind power generation is given and presented. In [28], a microgrid model with a solar panel, hydrogen fuel cell stack, electrolyzer and a radial distribution network was developed using a JAVA-based software to study the optimum design and operation of the microgrid. In [29], simulation tools that include a PV array model, maximum point tracking controller model, and a grid integrated inverter was developed for DER interconnection studies using an electromagnetic transient simulation program

(EMTP) developed by the Manitoba Hydro Research Center called PSCAD/EMTDC. In [6], a voltage balancing and synchronization scheme was developed for a microgrid with highly unbalanced loads using PSCAD/EMTDC. In [30], the active power/frequency and reactive power/voltage droop control strategies of a microgrid with dynamic models of a PV cell, wind turbine was developed using the open-source EMTP/Alternative Transient Program (ATP).

In the above mentioned references, the simulation tools have been developed on a purely software platform; however, the growing trend is in performing such simulation studies using real-time simulators to enable hardware-in-the-loop (HIL) simulations. In HIL simulations, parts of the power system are modeled in a software environment and interfaced with a physical hardware device under test (HDUT) using a real-time operating system [31]. Hardware-in-the-loop simulations provide a cost effective and safe method to test the operation of physical devices before connection to the actual power system [31]. This research focuses on developing a microgrid system with detailed models of distributed energy resources namely a PV array, wind turbine and diesel generator using a real-time digital simulator to be used for hardware-in-the-loop simulations.

### 2.8.1 Real-Time Digital Simulation for Microgrid Studies

The microgrid system is developed using a real-time EMTP based simulator developed by RTDS Technologies Inc. The EMTP algorithm originally developed by H.W Dommel uses the trapezoidal rule of integration to discretize the differential equations of power system components [32]. EMTP based simulations are widely adopted in the power system industry for performing detailed transient simulation studies for AC and DC power

systems [32]. In Dommel's EMTP algorithm, the differential equations of an inductor and capacitor are discretized to represent a Norton equivalent circuit having a conductance value in parallel with a current source. The conductance value is an instantaneous expression that links the current and voltage at the current-time step while the current source represents an expression of the relationship between the current injection and voltage at the previous time step [32]. Nodal analysis is then used to obtain the time domain solution of the equivalent representation of the discretized power system network. The Dommel EMTP algorithm representation of an electric circuit with passive components is shown in Figure 2-4.

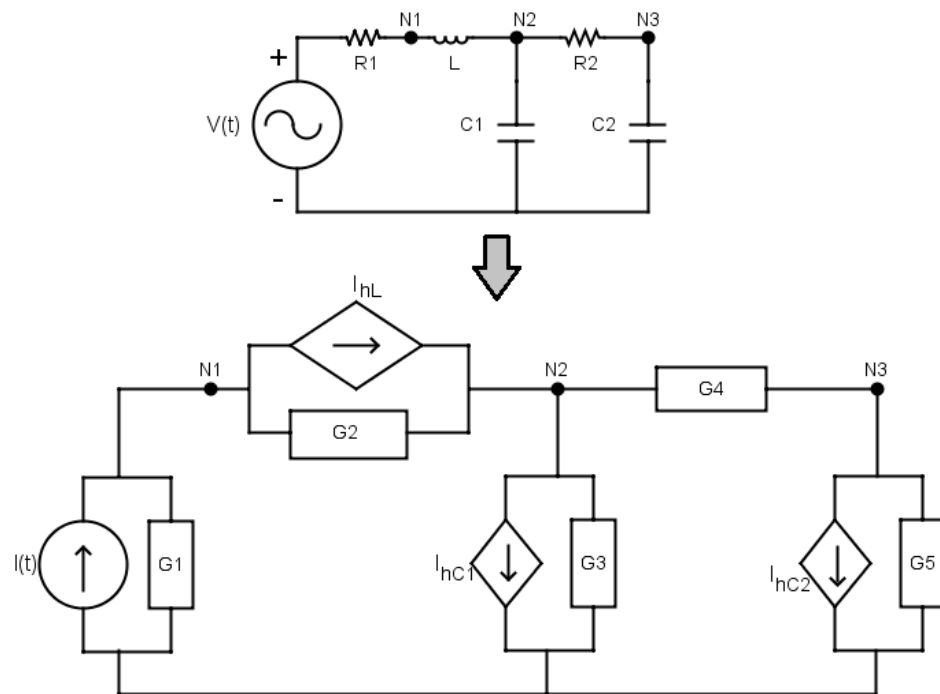


**Figure 2-4 Norton equivalent of an electrical circuit using the EMTP Dommel Algorithm [32]**

The power system solution of the Norton equivalent circuit is obtained by the nodal equation given by [32]:

$$[G]\mathbf{v}(t) = \mathbf{i}(t) + \mathbf{I}_{history} \quad (2.4)$$

where:

$\mathbf{v}(t)$  is the node voltages vector.

$\mathbf{i}(t)$  is the vector of current sources obtained from Norton equivalent of voltage sources in the network.

$\mathbf{I}_{history}$  is the vector of history term currents obtained from the trapezoidal integration representation of the power system components.

$[G]$  is the conductance matrix obtained from the transforming the electric circuit into the Norton equivalent using the EMTP algorithm.

From the nodal analysis of Figure 2-5, equation 2.4 becomes:

$$\begin{bmatrix} G_1 + G_2 & -G_2 & 0 \\ -G_2 & G_2 + G_3 + G_4 & -G_4 \\ 0 & -G_4 & G_4 + G_5 \end{bmatrix} \begin{bmatrix} V_{N_1} \\ V_{N_2} \\ V_{N_3} \end{bmatrix} = \begin{bmatrix} I(t) \\ 0 \\ 0 \end{bmatrix} + \begin{bmatrix} -I_{hL} \\ I_{hL} - I_{hC1} \\ -I_{hC2} \end{bmatrix} \quad (2.5)$$

$$I(t) = \frac{V(t)}{R_1} \quad (2.6)$$

The conductance terms are defined by:

$$G_1 = \frac{1}{R_1} ; \quad G_2 = \frac{\Delta T}{2L} ; \quad G_3 = \frac{2C_1}{\Delta T} ; \quad G_4 = \frac{1}{R_2} ; \quad G_5 = \frac{2C_2}{\Delta T} \quad (2.7)$$

The history current equations for the inductor and capacitor are given by:

$$I_{hL} = i_L(t - \Delta T) + \frac{\Delta T}{2L} v_L(t - \Delta T) \quad (2.8)$$

$$I_{hC1} = -i_{C_1}(t - \Delta T) + \frac{2C_1}{\Delta T} v_{C_1}(t - \Delta T) \quad (2.9)$$

$$I_{hC2} = -i_{C_2}(t - \Delta T) + \frac{2C_2}{\Delta T} v_{C_2}(t - \Delta T) \quad (2.10)$$

For a given time step  $\Delta T$ , the node voltages are solved by the matrix multiplication of the inverted the conductance matrix  $[G]^{-1}$  with current and calculated history term currents vectors obtained from the previous time step.

$$\mathbf{v}(t) = [G]^{-1}[\mathbf{i}(t) + \mathbf{I}_{history}] \quad (2.11)$$

In steady state operation, the conductance matrix is constant at every time step; however, in real power system networks the conductance matrix is constantly changing due to the presence of switching transients such as the faults, power converter switching and breaker operation [32]. Therefore in real-time digital simulations, the network voltages and currents need to be calculated at every time step because at any time a controller could trigger a change in the switching state of the network requiring the network conductance matrix to be inverted at each time step [31]. As the size of the power system network increases, so does the computational effort required to invert the conductance matrix and obtain the network solution at each time step. To achieve real-time performance, the RTDS simulator uses high speed parallel processors to share the computation burden and accelerate the network solution as illustrated in Figure 2-5 [31].

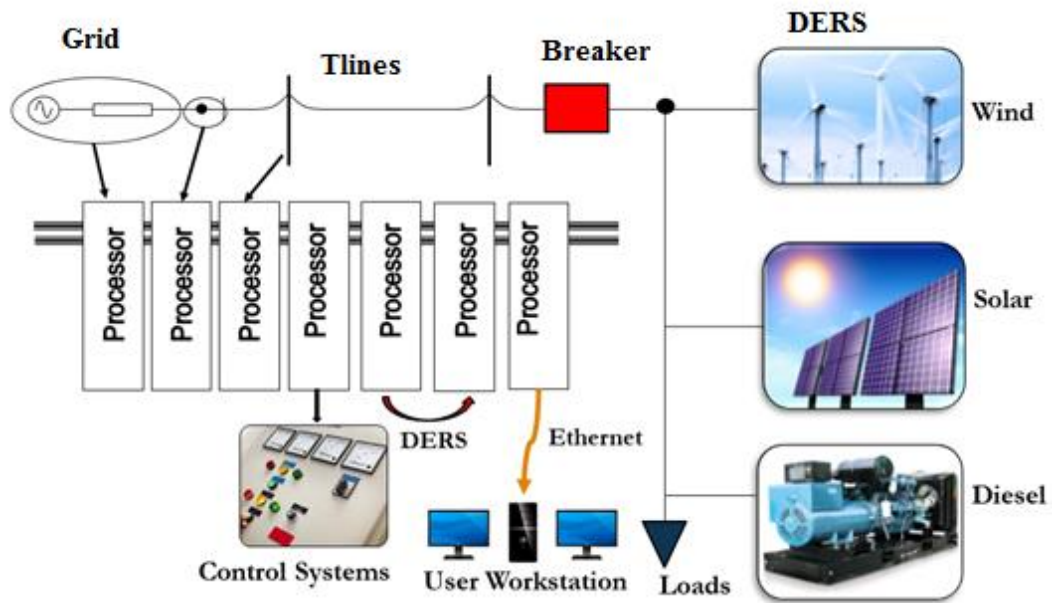


Figure 2-5 Microgrid simulation using the RTDS

The power and control components are assigned to different processors, which communicate with each other to obtain the overall solution of the system [31]. Maintaining real-time performance for 50/60Hz systems requires simulation time steps around  $50\mu\text{s}$  to solve for all possible switching states of the network. For power electronic converters having high switching frequencies (in the kHz range), smaller simulation time steps around  $1\text{-}3\mu\text{s}$  are required to represent the converter switching dynamics. The RTDS uses dedicated processors as well as predefined power system and control components for modeling power converters with simulation time steps between  $1\text{-}3\mu\text{s}$  [31].

The RTDS hardware is interfaced to a software called RSCAD where the simulation case is assembled using either user-defined or pre-defined components from the RSCAD library [31]. The RSCAD Draft module shown in Figure 2-7 provides the ability to organize simulation cases, automate or interact with the simulator operation for true real-time performance as well as analyze and post-process the simulation results [31].

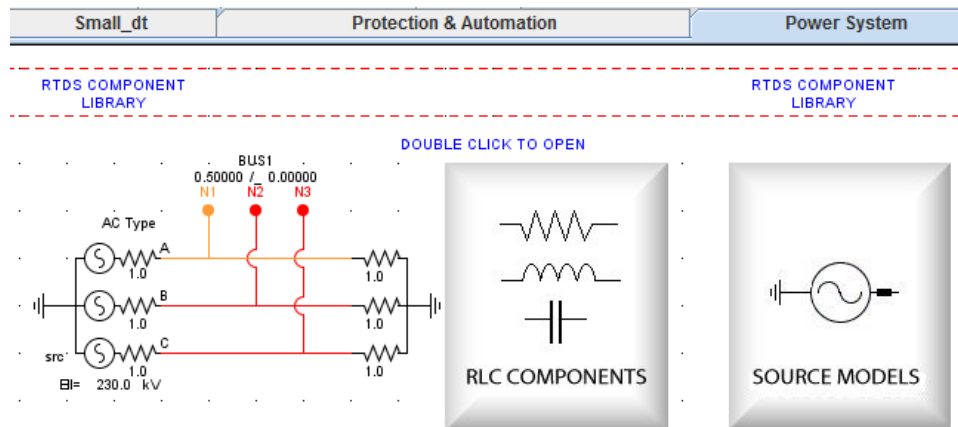


Figure 2-6 Screen shot of RSCAD Draft Module [31]

A significant benefit of using real-time digital simulators is the ability to connect physical devices such as control and protection equipment as shown in Figure 2-8. Hardware-in-the-loop simulations provide a cost effective and safe method for operators and researchers to thoroughly test and analyze the operation of physical devices under real-time conditions before they are installed in the actual system [31]. HIL simulations are used in various industries ranging from aeronautics, manufacturing, automotive, and robotics for testing and validating equipment design [33].

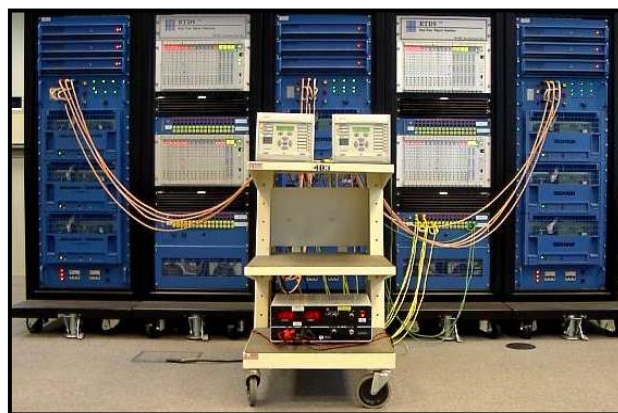


Figure 2-7 HIL testing using the Real Time Digital Simulator [31]

To enable HIL simulations, the RTDS supports data exchange between external devices and the software simulation using several interface cards that can send/receive analog input and output signals, digital input and output signals as well as network communication protocols such as supervisory control and data acquisition (SCADA), distributed network protocol (DNP), phasor measurement units (PMU), generic substation events and sampled values based on the international electro technical commission (IEC) 61850 standard [31]. In addition, actual recorded data can be used as input to the simulation using a play back feature to validate the simulation models [31].

Typically, HIL simulations in the power system industry have focused on control and protective relay testing. In [34], the HIL capability with the RTDS is demonstrated for testing a power electronic converter controller. In [35], a HIL method using the RTDS is proposed to test functions of control and operation of a developed microgrid management system (MMS). More recently due to increasing integration of distributed energy resources and power electronic converters with the distribution grids, interest in HIL simulations is shifting towards more power hardware-in-the-loop (PHIL) simulations [33]. PHIL is a more challenging interface than control and protection testing as the device under test (such as motors, generators, wind turbines, power inverters) produces power at high voltages and currents. In [36], the complexities and challenges of obtaining stable and reasonably accurate PHIL simulations are discussed. Continued research is required to develop interface and testing techniques that can be used to validate PHIL simulations for DER integration studies [36]. The goal of this research is to develop a microgrid case that can be used for DER integration studies using hardware-in-the-loop applications.

## 2.9 Concluding Remarks

Grid-integration of distributed energy resources offers several advantages such as reduced greenhouse gas emissions and increased power system reliability. Despite the mentioned benefits, several technical challenges have to be addressed to ensure the successful integration of these DERs using the microgrid concept. In this chapter, a discussion of some of the technical challenges has been provided highlighting the need for developing detailed benchmark simulation models for microgrid studies as will be discussed in Chapter 3. In addition, a discussion on a real-time transient simulation tool based on the electromagnetic transient program (EMTP), which offers a wide range of modeling capabilities used to represent the electromagnetic and control system transients of a power system was provided. However, due to the computational effort required to maintain real-time simulation, the size of the network is limited by the available hardware resources, Chapter 4 will discuss the use of average-value models to address this issue. The RTDS allows realistic and accurate analysis of the dynamics of power system and control components. Physical power, control and protection devices can be interfaced to the RTDS for hardware in the loop simulations making it a useful simulation tool in understanding the operation of distribution networks integrated with DERs in a microgrid concept. The modeling of a distribution power system network integrated with DERs using the RTDS as well as a hardware in the loop interface with a protective relay is discussed in Chapter 5.

# Chapter 3

## Modeling of Distributed Energy Resources

### 3.1 Introduction

This chapter discusses modeling of the distributed energy resources and their associated control systems. The DERs discussed are a diesel generator, a photovoltaic system and a doubly-fed wind turbine generator system.

### 3.2 Diesel Generator Model

Diesel generators are used as backup power supply during power outages, or to generate power in off-grid applications such as remote locations or large ships. Diesel generators are also used to provide ancillary services such as voltage control, load regulation and frequency control [37]. Currently, most microgrid implementations rely on diesel generating

systems [38]. The role of the diesel generator in the microgrid system discussed in this research is to regulate the microgrid frequency when in islanded operation as well as to provide real and reactive power in both grid-connected and islanded operation. The diesel generator is modeled as a synchronous generator with an excitation system driven by a diesel engine and speed governor. The diesel generating system modeled in RSCAD/Draft is shown in Figure 3-1.

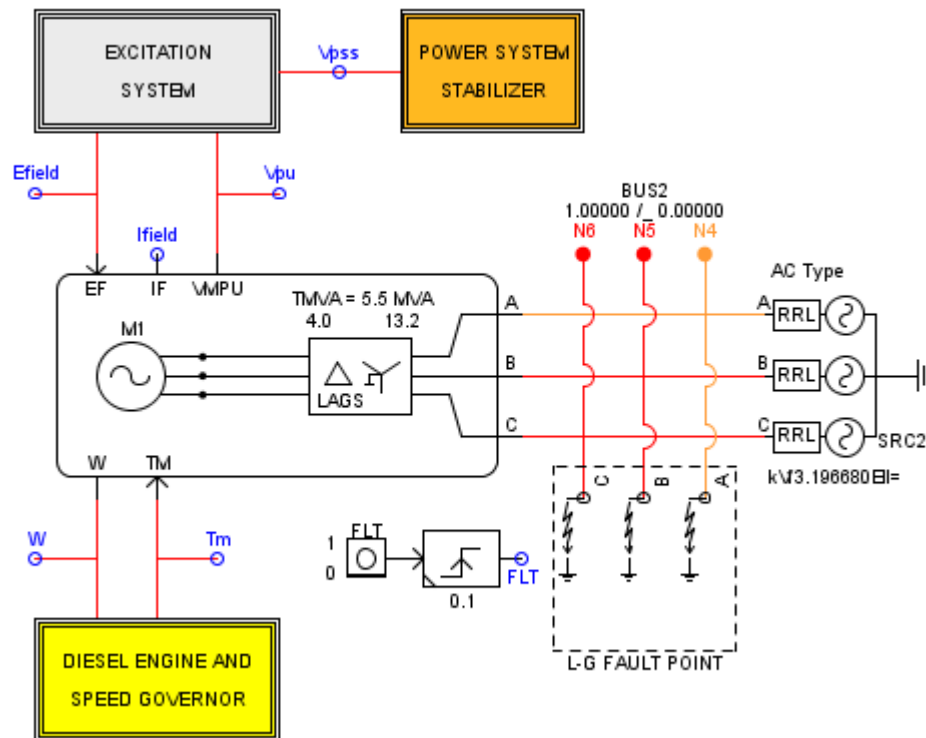


Figure 3-1 Diesel Generating System in RSCAD/Draft

### 3.2.1 Synchronous Generator Model

Synchronous generators are used in power systems to convert mechanical power to electrical power. The synchronous speed  $n_s$  in revolutions per minute (RPM) is given by equation 3.1, where  $f$  is the grid frequency in Hertz and  $p_f$  is the number of field poles [39].

$$n_s = \frac{120 * f}{p_f} \quad (3.1)$$

The synchronous generator model used in this thesis is a salient pole generator with a stationary stator (armature) winding and a rotating rotor (field) winding. The rotor holds the field winding which produces the magnetic field required to induce a voltage on the armature windings mounted on the stator. When supplying a load, the three-phase currents in the armature winding produce a synchronously rotating magnetic field [39]. Damper or amortisseurs windings are included in the rotor to reduce oscillations caused by abrupt load changes when the generator is in steady state operation [39]. Detailed analysis on the mathematical modeling of salient pole synchronous generators can be found in [39] and is omitted in this thesis. For the simulations carried out in this thesis, the synchronous generator model available in the RSCAD software shown in Figure 3-1 was used with appropriate parameters given in Table 3-1.

**Table 3-1 Synchronous machine parameters [31]**

Rated MVA <b>S</b>	5.5
Power MW <b>P</b>	3.0
Vrated_primary <b>Vprim</b>	13.2 kV LL rms
Vrated_secondary <b>Vsec</b>	4.00 kV LL rms
Frequency <b>F</b>	60 Hz
Stator leakage reactance <b>X<sub>a</sub></b>	0.130 pu
d axis unsaturated reactance <b>X<sub>d</sub></b>	1.790 pu
d axis unsaturated transient reactance <b>X'<sub>d</sub></b>	0.169 pu
d axis unsaturated sub – transient reactance <b>X''<sub>d</sub></b>	0.135 pu
q axis unsaturated reactance <b>X<sub>q</sub></b>	1.710 pu
q axis unsaturated transient reactance <b>X'<sub>q</sub></b>	0.228 pu
q axis unsaturated sub – transient reactance <b>X''<sub>q</sub></b>	0.200 pu
Stator resistance <b>R<sub>a</sub></b>	0.002 pu
d axis unsaturated transient open time constant <b>T'<sub>do</sub></b>	4.300 sec
d axis unsaturated sub – transient open time constant <b>T''<sub>do</sub></b>	0.032 sec
q axis unsaturated transient open time constant <b>T'<sub>qo</sub></b>	0.850 sec
d axis unsaturated sub – transient open time constant <b>T''<sub>qo</sub></b>	0.050 sec
Inertia constant <b>H</b>	3.030 MWs/MVA

An optional Wye-Delta transformer can be included in the generator model to help reduce the node requirements in the power system network [31]. From Figure 3-1, the generator control inputs to the generator model are the excitation field voltage and the mechanical torque. The RSCAD generator model and its associated controls can be initialized from an initial steady state point to avoid large transients when the simulation starts [31]. The initial mechanical torque and initial field voltage required to initialize the generator and its generator controls are calculated from the entered machine parameters and steady state (load flow) conditions [31]. The rotor angle of the generator can be locked to its initial value during simulation start up and freed when the generator settles to its steady state (load flow) condition [31]. The Lock/Free feature in the RSCAD generator model helps in the initialization and tuning of the generator controls as the presence of a large transient when the generator is changed from Lock to Free mode indicates that the generator controls were not properly initialized to the steady state condition and/or appropriate parameters were not used in the generator controls [31].

### **3.2.2 Modeling the Diesel Engine and Speed Governor**

Diesel engines are a type of internal combustion engine (ICE) that produce power through the compression of air and burning of diesel fuel inside one or multiple cylinders [40]. The power produced by the diesel engine drives the shaft of the synchronous generator, which converts the mechanical power to electrical power to supply the grid and/or loads. Compared to other internal combustion engines such as gasoline engines, diesel engines have a simpler structure, higher efficiency, and are more cost effective due to their long operating life [40].

In [41], a detailed mathematical model of a diesel engine and its control process is provided; however the described level of complexity is not required for transient simulation studies and can be replaced with appropriate simplified models with minimal impact on the simulation accuracy. The key parameters required for a sufficient model of a diesel engine are the gain and time constant of the actuator which controls the fuel injection to the cylinders, the diesel engine inertia which can be lumped with the inertia of the synchronous generator, the droop factor that regulates the engine speed, and the time delay in the diesel engine fuel combustion process [42]. This simplified representation is sufficient as the dynamics of the speed governor is the key factor that determines the transient stability of the diesel generating system. In this work, the diesel engine dynamics is represented using a first-order transfer function with gain  $K_d$  and time constant  $T_{d1}$ . The values for  $K_d$  and  $T_{d1}$  were set to set to 1 and 0.1secs. A delay component  $T_d$  is used to represent the time delay between fuel combustion in the diesel engine cylinders and torque production [38, 43]. Typical range of the delay values are 0.01 – 0.4 secs. Figures 3-2 and Figure 3-3 show the block diagram model of the diesel engine and speed governor and its implementation in RSCAD/Draft respectively.

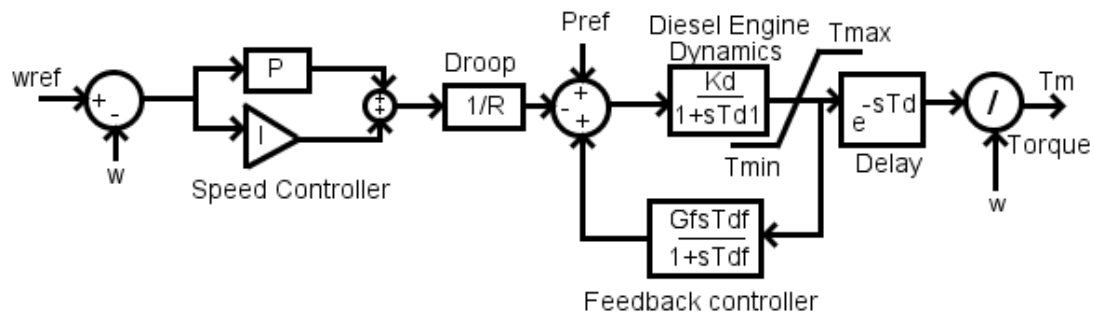


Figure 3-2 Block diagram model of diesel engine and speed governor

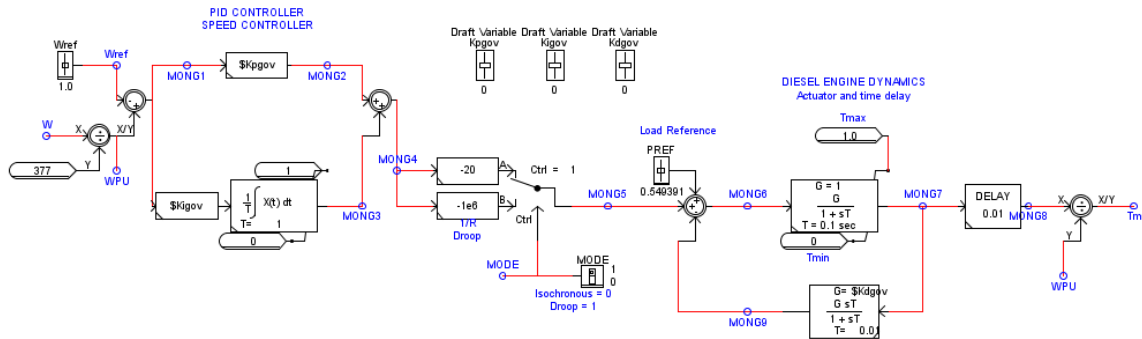


Figure 3-3 Diesel engine and speed governor model in RSCAD/Draft

The inputs to the diesel engine and speed governor model are the per unit speed reference  $\omega_{ref}$  and the per unit diesel generator speed  $\omega$ . The output is the mechanical torque  $T_m$ , which drives the shaft of the synchronous generator. The output torque is limited by the maximum and minimum torque limits  $T_{max}$  and  $T_{min}$  which are set to 1.0 pu and 0.0 pu, respectively. The function of the speed governor controller is to regulate the shaft speed and subsequently the frequency of the synchronous generator.

The droop factor or speed regulation factor ( $R$ ) defined by equation 3.2 describes the relationship between changes in the generator speed to load changes [44].

$$R(\%) = \frac{\text{No load speed} - \text{Full load speed}}{\text{No load speed}} \quad (3.2)$$

In grid-connected operation, the diesel generator operates in speed-droop mode ( $R$  is set to 5%) and supplies the specified power at the grid frequency. In island operation, the diesel generator is operated in isochronous mode ( $R$  is set at 0.01%) to maintain a constant speed under varying load conditions. PID controllers are commonly implemented for the speed governor due to the ease in tuning the parameters and minimum implementation complexity compared to other speed control models [43]. A PI (Proportional-Integral) controller with derivative feedback is used in this work to implement the speed governor. The speed controller regulates the speed  $\omega$  (rad/sec) of the diesel generator to the given reference

value  $\omega_{\text{ref}}$ (rad/sec) under steady state and transient conditions [44]. The PI parameters were obtained by adjusting the proportional gain  $K_{\text{pgov}}$ , integral gain  $K_{\text{igov}}$ , and feedback derivative gain  $K_{\text{dgo}}$  until a satisfactory response was observed. The gain parameters were adjusted using the RSCAD script feature which enables automatic/batch mode operation. Batch mode operation is defined as the ability to compile RSCAD/draft and run various test cases on the RTDS with minimal or no user interaction [31].

### 3.2.3 Modeling the Excitation System

The primary role of the excitation system is to provide direct current (DC) to the generators field winding and regulate the generator terminal voltage to a specified reference value [44]. The components in an excitation system include exciters to provide direct current to the field windings, automatic voltage regulators for controlling the exciters to a specified terminal voltage level, voltage transducers that change the alternating current (AC) of the generator terminal voltage to a DC value, limiters and protection to keep the exciters and generator quantities within safe limits of operation, and power system stabilizers that provide supplementary signals for damping out power oscillations [39].

Excitation systems are classified as either DC, AC or static excitation systems and a detailed explanation of these classes can be found in [39]. Several advanced models of these classes of excitation systems used in the control of power systems are provided in standards such as the IEEE Recommended Practice for Excitation System Models for Power System Stability Studies [45]. To reduce the modeling complexity of tuning the parameters of the excitation systems for power system stability studies, a simplified model of the amplifier

and exciter that neglects saturation effects and represents the exciter and amplifier dynamics using a first order transfer function is used in this research [44]. A PID (Proportional-Integral-Derivative) controller is used to improve the transient response and reduce the steady state error of the automatic voltage regulator (AVR). The block diagram of the excitation system used in this research is shown in Figure 3-4.

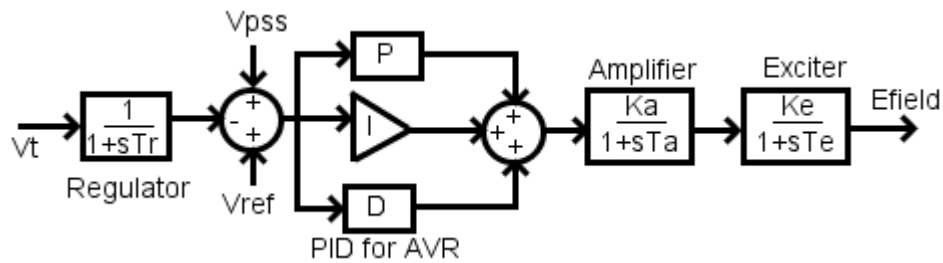


**Figure 3-4 Block Diagram of Excitation System**

The inputs to the exciter are the terminal voltage reference  $V_{ref}$ , the power system stabilizing signal  $V_{pss}$  and the per unit terminal voltage of the synchronous generator  $V_{pu}$  measured through a voltage transducer with time constant  $T_r$ .  $K_A$  and  $T_A$  are the gain and time constant of the amplifier and  $K_E$  and  $T_E$  are the exciter gain and time constant. The output of the excitation system is the field voltage for the generator field windings  $E_{field}$ . Table 3-2 gives typical ranges used to select the gain and time constant values for the exciter, amplifier and voltage transducer [44].

**Table 3-2 Excitation system parameters**

Parameter	Value or range
$T_r$	0.01 – 0.2 (secs)
$K_a$	10 - 400
$T_a$	0.02 – 0.1 (secs)
$K_e$	1
$T_e$	0.01– 0.5 (secs)

Figure 3-5 shows the block diagram of the excitation system implemented in RSCAD/Draft where  $V_{rmax}$ ,  $V_{rmin}$  and  $V_{amax}$ ,  $V_{amin}$  are the maximum and minimum limits for the output of the PID AVR control and exciter amplifier respectively. The derivative portion

of the PID control is implemented as a washout block to minimize noise caused by using the derivative function.

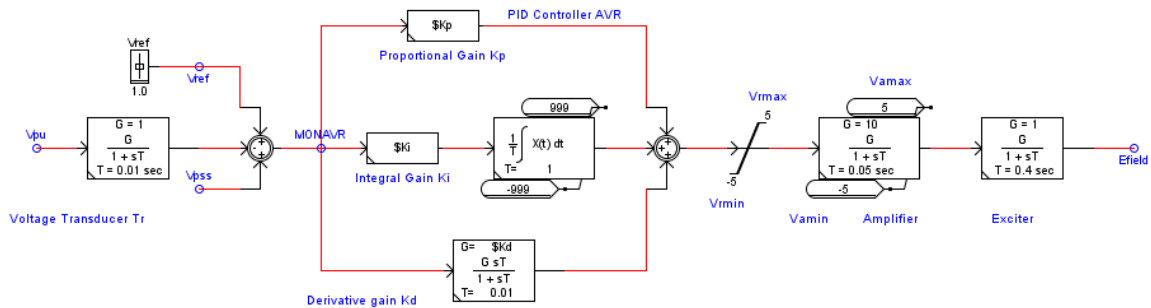


Figure 3-5 Excitation System in RSCAD/Draft

The manual tuning method described for the diesel governor parameters was used to obtain an acceptable set of parameters for the proportional  $K_p$ , integral  $K_i$  and derivate  $K_d$  gains for the automatic voltage regulator. The proportional, integral and derivative gains are adjusted in a script file until a satisfactory response is obtained.

### 3.2.4 Modeling the Power System Stabilizer

Power system stabilizers (PSS) are used to provide an additional stabilizing signal to the excitation system of the synchronous generator [39]. The PSS model implemented in this work is shown in Figure 3-6 with the generator angular speed used as the input.

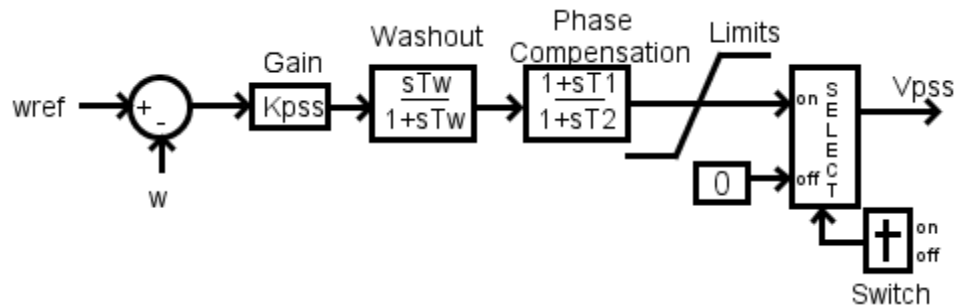


Figure 3-6 Block diagram of the power system stabilizer.

The components of the PSS include a phase compensation block, washout filter, gain, and output limits. The gain  $K_{pss}$  is selected to provide adequate damping to the generators rotor

oscillations without compromising the system stability [39]. The phase compensation time constants  $T_1$  and  $T_2$  are used to compensate for the phase lag between the excitation input and generators electrical torque [39]. The washout block  $T_w$  ensures that the dc value is not affected by the controller values and allows the PSS to respond to speed variations associated with oscillations in the rotor frequency [39]. The limits are selected to provide a suitable range of control while maintaining acceptable transient response [39].

The dynamic response of the diesel generating system with or without the PSS can be observed by using a signal select switch. The PSS output is set to zero when the switch is turned off. When the switch is on, the PSS provides the stabilizing signal using the generator speed deviation as a control input. The lead and lag time constants ( $T_1$  and  $T_2$ ) are determined from the phase compensation  $\phi_m$  according to the following equations [39]:

$$G_{comp}(s) = \frac{sT_1 + 1}{sT_2 + 1} = \frac{sT + 1}{s\alpha T + 1} \quad (3.3)$$

$$\sin \phi_m = \frac{1 - \alpha}{1 + \alpha} \quad (3.4)$$

$$\omega_m = \frac{1}{T\sqrt{\alpha}} \quad (3.5)$$

where  $\omega_m$  is taken as the frequency of the rotor oscillations. Typically the rotor oscillation frequency range of interest for power system stability is 0.8 – 2Hz and a satisfactory value of the time constant  $T_w$  of the washout filter for this frequency range is 1.5 seconds [39]. The PSS gain is selected to provide adequate damping, however high gain values may result in further instability to the response of the AVR system [39]. Table 3-3 shows the range of values used for tuning the PSS parameters [39].

Table 3-3 Power system stabilizer parameters

PSS Parameters	Value or range
PSS Gain $K_{pss}$	1 - 400
Washout time constant $T_w$	1.5(secs)
Phase compensation $\phi_m$	30 – 60 (degrees)
PSS Limits	$\pm 0.2$ pu

Figure 3-7 shows the PSS model implemented in RSCAD/Draft with the phase compensation  $\phi_m$  selected to be  $30^\circ$  with the rotor oscillation frequency  $\omega_m$  taken as 10 radians/second.

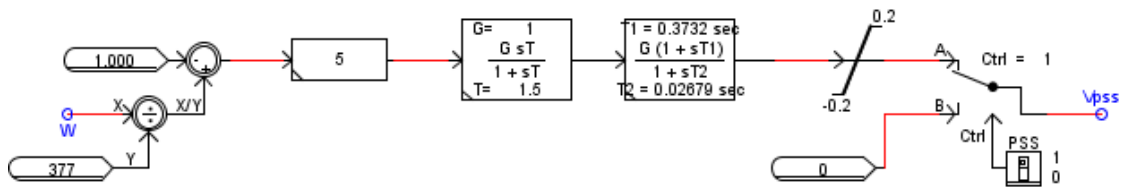


Figure 3-7 Power System Stabilizer in RSCAD/Draft

### 3.2.5 Simulation of the Diesel Generation System

The steady state real and reactive power of the synchronous generator in Figure 3-1 is given as 3MW and 0.08 MVar. The given initial mechanical torque and field voltage required to initialize the generator controls to meet the steady state machine conditions calculated from the RSCAD synchronous machine program are 0.55 pu and 1.42 pu, respectively. Initialization of the generator control parameters to a new steady state condition is required when the diesel generator is used in a different system. The diesel generator is connected to a grid with impedance  $10\angle 86^\circ \Omega$ . The objective is to compare the generator response with and without the PSS for different values of the AVR PID gains with the governor PID gains set to 3, 1 and 0.2, respectively. The diesel generator response to a 0.1 second, 0.1 $\Omega$ , three phase line to ground fault with the power system stabilizer turned on is shown in Figure 3-

8 and Figure 3-9. An improved transient response is obtained with the AVR gain set to 1.0, 0.4 and 0.2 and the PSS turned on (blue curve).

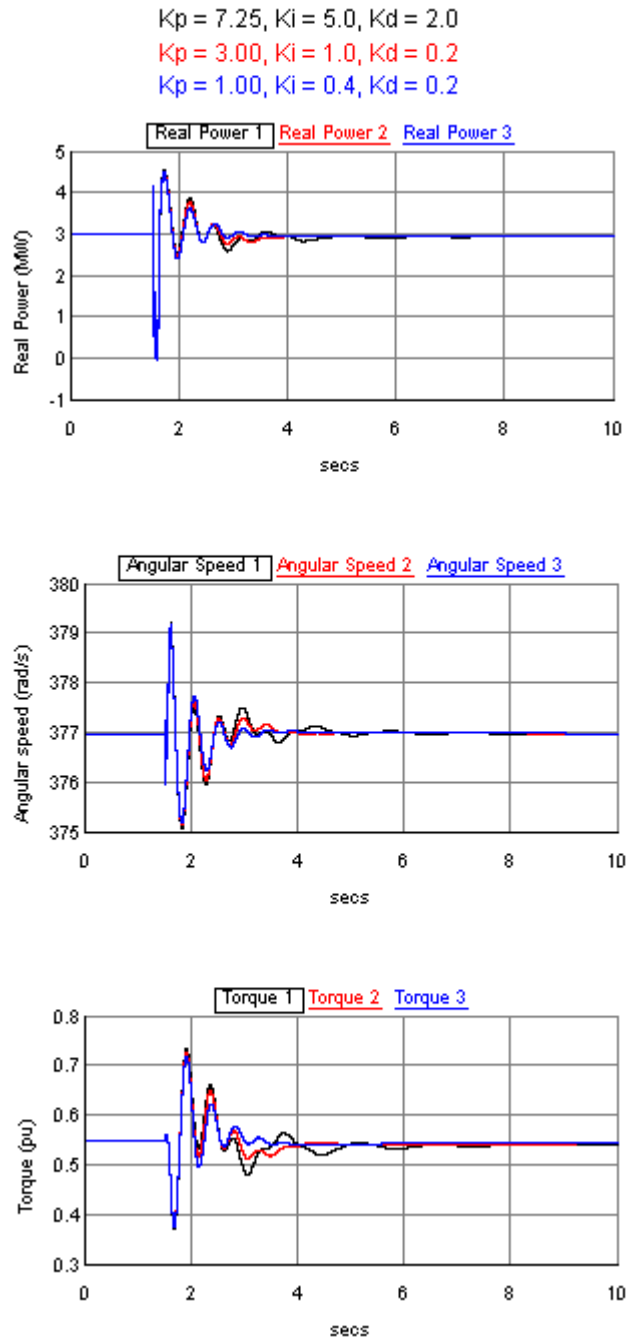


Figure 3-8 Diesel generator real power, per unit angular speed, and mechanical torque ( $T_m$ )

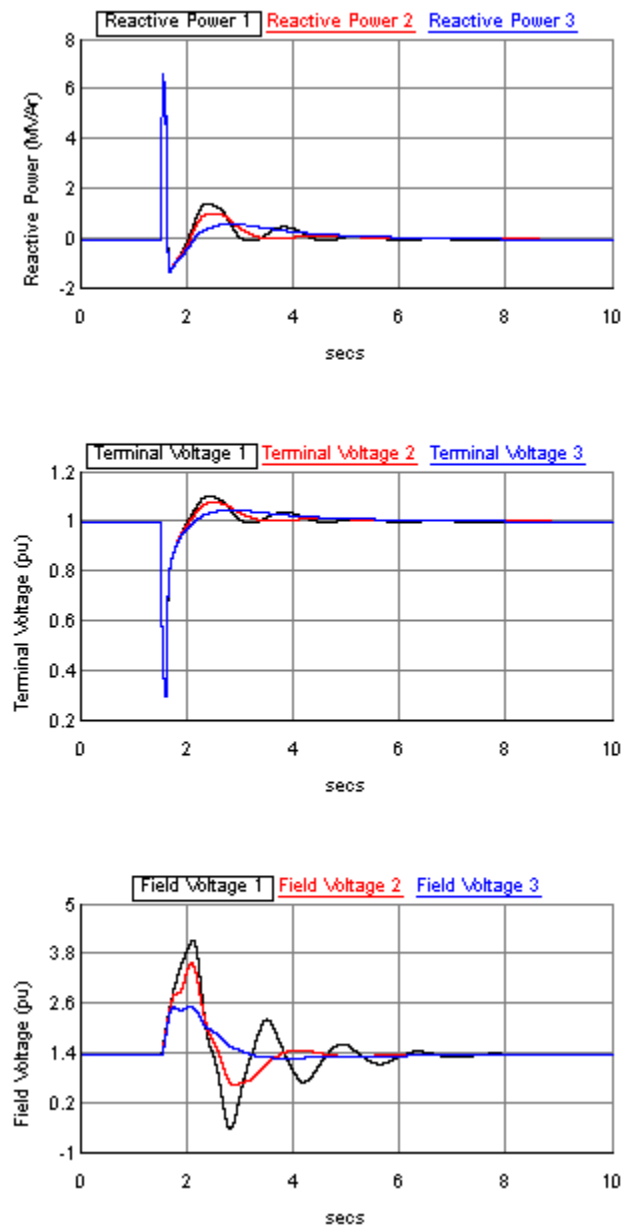


Figure 3-9 Diesel generator reactive power, terminal bus voltage and excitation field voltage

### 3.3 Photovoltaic Energy System Model

Photovoltaic (PV) systems convert the energy from the sun into electricity. Demand for solar energy is rising due to technological advances in solar cell manufacturing, increasing

solar cell power conversion efficiency, and decreasing PV installation and maintenance costs [46]. Figure 3-10 shows the PV system modeled in RSCAD/Draft. The components of the PV system include a solar array, power converter, associated controllers, and a grid interfacing transformer and a load.

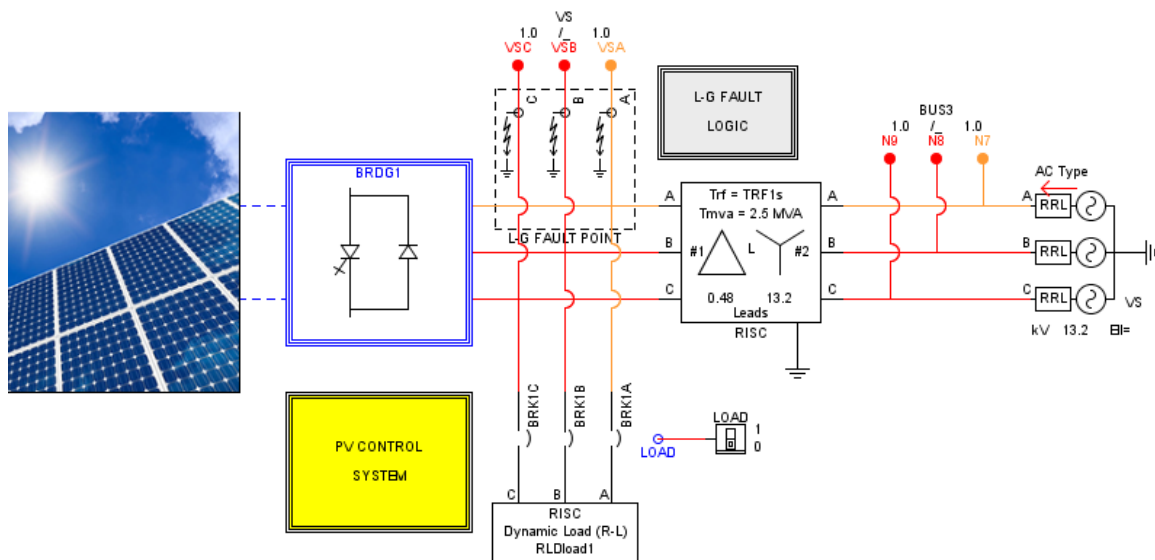


Figure 3-10 PV system modeled in RSCAD draft

### 3.3.1 PV Array Model

The fundamental component of a PV array is the solar cell. Solar cells are manufactured using semiconductor materials that produce an electric charge when exposed to light. Semiconductors require a certain amount of energy called the bandgap energy to release electrons which participate in the conduction of electric charge across the p-n junction in the semiconductor [47]. A properly designed p-n junction structure in the semiconductor can cause separation of these charges to create a voltage source. The most commonly used semiconductor in solar cells is silicon which can be in the form of mono-crystalline, polycrystalline or amorphous [47]. Table 3-4 shows the energy conversion efficiency of these forms of silicon solar cells.

Table 3-4 Comparing efficiency of commercial silicon solar cells [48]

	<b>Monocrystalline</b>	<b>Polycrystalline</b>	<b>Amorphous</b>
<b>Efficiency</b>	15-20%	13-16%	6-8%

A typical silicon solar cell produces a voltage of about 0.7 V. In order to achieve useful voltage and current levels, solar cells are commonly connected in series and/or parallel to form PV modules, which produce higher voltages in the range of 16V – 36V. To produce large amounts of voltage (kV) and current (kA) for practical applications, PV modules are combined in series and parallel to form PV arrays as shown in Figure 3-11.

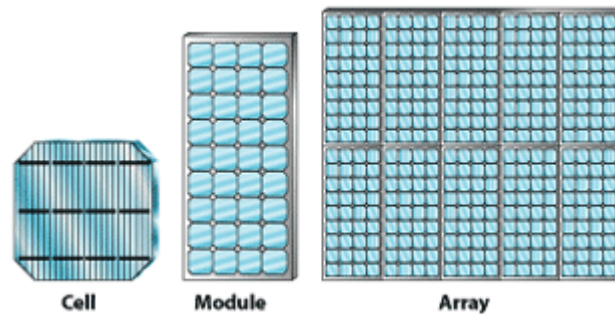


Figure 3-11 PV Cell - Module - Array [49]

The parameters used to specify how the cells are interconnected to form arrays in a series-parallel connected PV array are the number of series connected cells in a module  $n_s$ , the number of parallel connected cells in a module  $n_p$ , the number of series connected modules  $N_s$  and the number of parallel connected modules  $N_p$  [31]. A commonly used practical solar cell which includes a series and shunt resistance to model the non-linear behaviour of a solar cell is shown in Figure 3-12 [50].

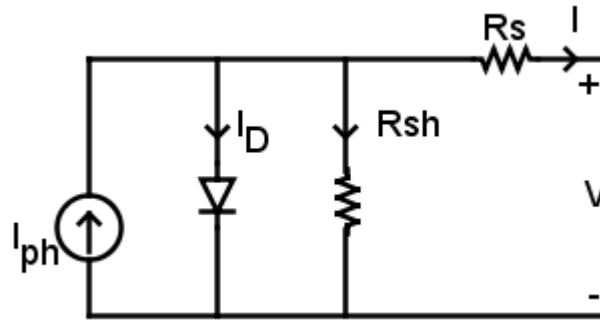


Figure 3-12 Practical model of a solar cell

The current-voltage relationship of the solar cell model in Figure 3-12 is given by [50]:

$$I = I_{ph} - I_D - I_{sh} \quad (3.6)$$

$$I = I_{ph} - I_o \left( \exp \left( \frac{V + R_s I}{n_s a V_t} \right) - 1 \right) - \left( \frac{V + R_s I}{R_{sh}} \right) \quad (3.7)$$

The photocurrent  $I_{ph}$  is the current induced by the incidence of sunlight on the solar cell [50, 51]. The diode current  $I_D$  produces the I-V characteristic of the PV cell where  $I_o$  is the diode reverse saturation current [50, 51]. The diode ideality factor  $a$  is a measure of how closely the diode matches the ideal diode equation [50, 51]. The series resistance  $R_s$  is the sum of several structural resistances in the solar cell while the shunt resistance  $R_{sh}$  represents the leakage current of the p-n junction of the semiconductor material and the manufacturing process of the solar cell [50, 51].  $V_t$  is the diode thermal voltage, which is a constant defined at any given temperature  $T$  (in K) by [50, 51]:

$$V_t = \frac{kT}{q} \quad (3.8)$$

$k$  is the Boltzmann constant ( $1.3806503 \times 10^{-23}$  J/K) and  $q$  is the magnitude of an electron charge ( $1.602176 \times 10^{-19}$  C). The operating current and voltage depends on the variation of

the solar cell parameters with a given insolation  $G$  ( $\text{W}/\text{m}^2$ ) and temperature  $T$  (K) as described by equations (3.9) – (3.11) where  $k_i$  is the short circuit current temperature coefficient ( $\%/^{\circ}\text{C}$  or  $\text{A}/^{\circ}\text{C}$ ) and  $E_g$  is the energy gap (eV) of the solar cell semiconductor material.

$$I_{ph} = \frac{G}{G_{stc}} * (I_{ph_{stc}} + k_i(T - T_{stc})) \quad (3.9)$$

$$I_o = I_{ostc} \left( \frac{T}{T_{stc}} \right)^3 \exp\left( \frac{E_g}{aV_t} \left( 1 - \frac{T_{ref}}{T} \right) \right) \quad (3.10)$$

$$a = a_{stc} \left( \frac{T}{T_{ref}} \right) \quad (3.11)$$

The relationship between the current and voltage of a PV cell is shown in Figure 3-13. The current-voltage curve ranges from the short circuit current ( $I_{sc},0$ ) to the open circuit voltage ( $0,V_{oc}$ ) with a knee point ( $I_{mp}, V_{mp}$ ) defined as the maximum power point where the PV array generates maximum electrical power  $P_{max}$ .

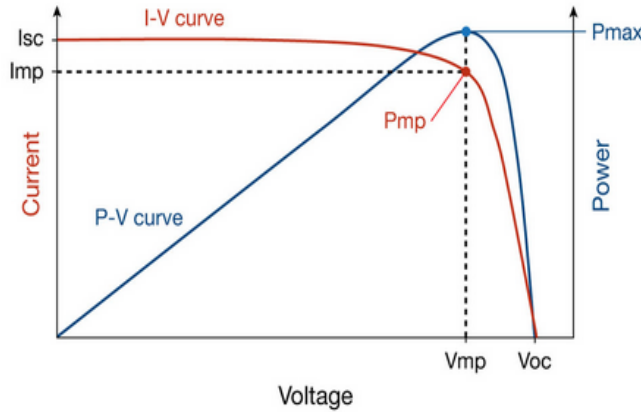
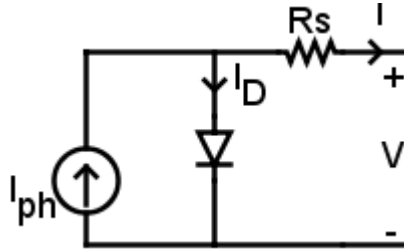


Figure 3-13 I-V and P-V curve of a PV cell/module/array

The required parameters at standard test conditions  $I_{ph_{stc}}, I_{ostc}, a_{stc}, R_s, R_{sh}$  are generally not provided in the PV data sheets and have to be estimated from the available data namely  $I_{sc_{stc}}, V_{oc_{stc}}, I_{m_{stc}}, V_{m_{stc}}, R_{s_{stc}}, R_{sh_{stc}}$  specified at standard test conditions ( $G_{stc} = 1000 \frac{\text{W}}{\text{m}^2}, T_{stc} = 25^{\circ}\text{C}$ ). Methods used to approximate the unknown solar

cell parameters include analytical approximations, iterative algorithms, or curve fitting methods [50, 52]. The complexity of modeling the solar cell increases with the number of unknown parameters to be estimated. To reduce the modeling complexity, the solar cell model can be simplified by neglecting the effect of the shunt resistance as shown in Figure 3-14.



**Figure 3-14 Solar cell model with shunt resistance neglected**

The current-voltage equations for the solar cell model in Figure 3-14 is given as:

$$I = I_{ph} - I_o \left( \exp \left( \frac{V + R_s I}{n_s a V_t} \right) - 1 \right) \quad (3.12)$$

The four unknown parameters ( $I_{ph_{stc}}$ ,  $I_{o_{stc}}$ ,  $a_{stc}$ ,  $R_s$ ) are estimated using the analytical approximations given in [53]:

$$I_{ph_{stc}} = I_{sc_{stc}} \quad (3.13)$$

$$I_{o_{stc}} = \frac{I_{sc_{stc}}}{\left( \exp \left( \frac{V_{oc_{stc}}}{n_s a_{stc} V_t} \right) - 1 \right)} \quad (3.14)$$

$$R_s = \frac{n_s a_{stc} V_t \ln \left( 1 - \frac{I_{m_{stc}}}{I_{sc_{stc}}} \right) + (V_{oc_{stc}} - V_{m_{stc}})}{I_{m_{stc}}} \quad (3.15)$$

$$a_{stc} = \frac{q(2V_{m_{stc}} - V_{oc_{stc}})}{n_s kT \left[ \frac{I_{sc_{stc}}}{I_{sc_{stc}} - I_{m_{stc}}} + \ln \left( 1 - \frac{I_{m_{stc}}}{I_{sc_{stc}}} \right) \right]} \quad (3.16)$$

The total PV array current and power is calculated as:

$$I_{pv} = n_p N_p I_{ph} - n_p N_p I_o \left( \exp \left( \frac{V_{pv} + \frac{N_s}{n_p N_p} R_s I_{pv}}{n_s N_s a V_t} \right) - 1 \right) \quad (3.17)$$

$$P_{pv} = V_{pv} I_{pv} \quad (3.18)$$

The solar cell model in RSCAD/Draft shown in Figure 3-15 is used with the assumption that the effect of the shunt resistance is negligible ( $R_{sh} > 1000 \text{ ohms}$ ). The inputs to the PV model are the insolation ( $\text{Watts/m}^2$ ) and temperature ( $^{\circ}\text{C}$ ) and the outputs are the positive and negative DC node voltages  $V_P$  and  $V_N$ .

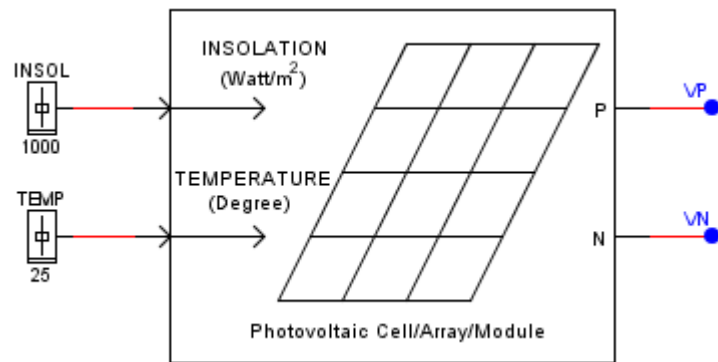


Figure 3-15 RSCAD PV Model [31]

### 3.3.2 Modeling the PV System Power Converter

Power converters are required to connect the PV array to the grid. PV arrays can be interfaced to the grid through a single stage or dual stage power converter topology as shown in Figure 3-16 and Figure 3-17 respectively.

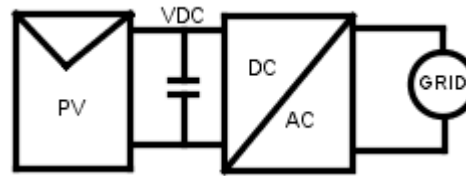


Figure 3-16 Single stage PV converter topology

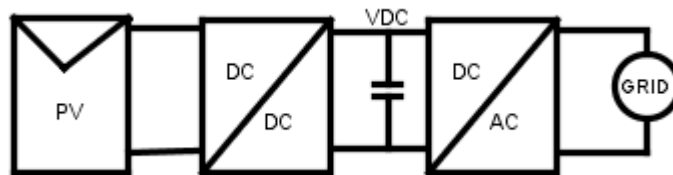


Figure 3-17 Dual stage PV converter topology

The dual stage topology uses a DC/DC converter to first step up or step down the PV voltage followed by a DC/AC converter to interface with the grid. The single stage topology uses only a DC/AC converter to interface with the grid. The single stage topology has a higher power efficiency than the dual stage; however, the design of the control scheme is more complex as the DC/AC converter handles all the control functions to transfer the maximum available power from the PV array to the grid [54]. The single stage, grid-connected PV system shown in Figure 3-18 is implemented in this research. A DC capacitor is used to reduce oscillations on the DC voltage. A delta-wye transformer is used to step up the VSC AC side voltage to the grid level and further minimize harmonic current injections to the grid. Interface reactors and capacitive filters are used to interface the VSC's AC side and the grid at the point of connection (PCC) and to minimize the converter harmonics injected to the grid [55].  $R$  represents the internal resistance of the interface reactor  $L$ , which is selected such that the resonant frequency of the equivalent inductance seen by the filter with the capacitance  $C$  is smaller than the power converters switching frequency

but larger than the grid frequency [56]. The equivalent inductance  $L_{eq}$  is the sum of the grid inductance, transformer leakage reactance and the interface reactor [56].

$$f_{grid\_60Hz} < \left( f_{resonant} = \frac{1}{\sqrt{L_{eq}C}} \right) < f_{swit\_VSC} \tag{3.19}$$

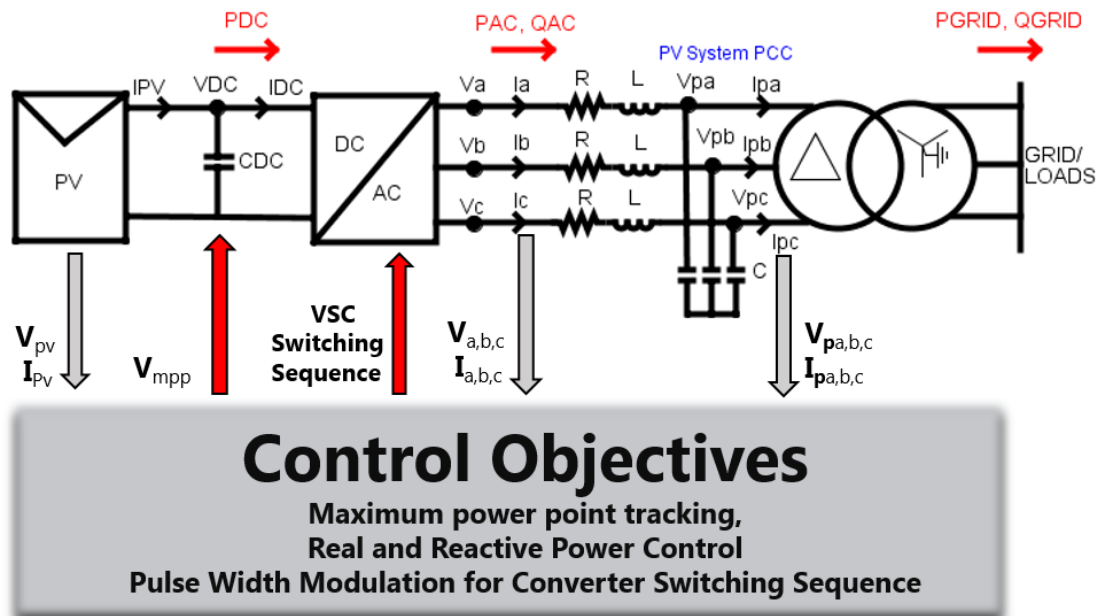


Figure 3-18 Single-Stage, Grid-connected PV system

Several DC/AC power converter topologies exist to interface the PV array with the grid. A commonly used converter topology is the two-level voltage source converter (VSC) shown in Figure 3-19.

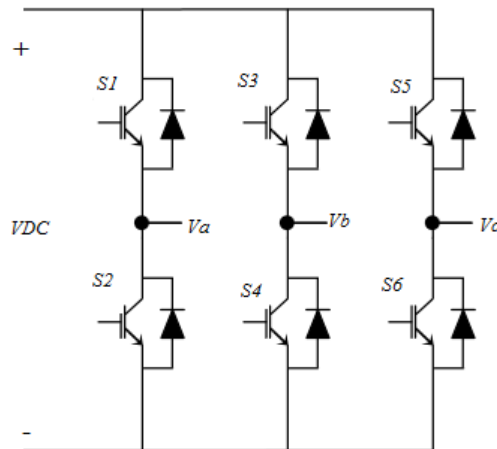
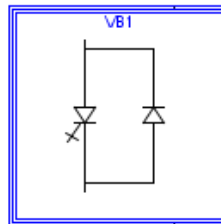


Figure 3-19 3-phase, 2-level Voltage Source Converter

The two level, three phase VSC has three legs each with two valves having an insulated-gate bipolar transistor (IGBT) semiconductor power device and an anti-parallel diode. Each leg of the VSC is connected to one phase of the grid where the AC side phase voltages can adopt either of two voltage levels,  $-V_{DC}$  when the bottom switches are turned ON or  $+V_{DC}$  when the top switches are turned ON with reference to the DC side mid-point [55]. The VSC switching frequencies are commonly in the 1- 4 kHz range. Higher switching frequencies (4-20 kHz) may be used to improve the output waveform but with an increase in the VSC power losses. The 2-level, VSC is modeled in the RSCAD using a small time step subnetwork shown in Figure 3-20. The small time step subnetwork is solved in RSCAD within a time step of 1.4–3 $\mu$ secs enabling the simulation of the high switching frequency dynamics of the VSC [31].

Small-Time Step Subnetwork

**Figure 3-20 Small time step simulation of the VSC in RSCAD [31]**

The switching of the VSC valves is done using sinusoidal pulse width modulation (SPWM) due to its simplicity and minimized lower order harmonics [57]. In SPWM, the output voltage waveforms are generated by comparing a high frequency triangular carrier wave with a low frequency sinusoidal modulation signal. The comparison of these two signals generate firing pulses that control the switching of each valve in the VSC bridges. The parameters that determine the magnitude and harmonic content of the output voltage are the amplitude modulation index  $m$  and the frequency modulation index  $mf$  [57].

$m$  is defined as the ratio of the amplitude of the modulating signal,  $A_c$ , to the amplitude of the carrier signal,  $A_m$ . For  $-1 \leq m \leq 1$ , the VSC operates in a linear modulation range between the carrier signal and the output voltages. For  $m \geq 1$ , the VSC becomes over modulated degrading the quality of the output voltage waveforms [57]. The modulation waveforms are symmetric, sinusoidal signals generated by the PV control scheme and given by:

$$m_a(t) = m \cos(\omega t + \theta) = \frac{A_m}{A_c} \cos(\omega t + \theta) \quad (3.20)$$

$$m_b(t) = m \cos\left(\omega t + \theta - \frac{2\pi}{3}\right) = \frac{A_m}{A_c} \cos\left(\omega t + \theta - \frac{2\pi}{3}\right) \quad (3.21)$$

$$m_c(t) = m \cos\left(\omega t + \theta - \frac{4\pi}{3}\right) = \frac{A_m}{A_c} \cos\left(\omega t + \theta - \frac{4\pi}{3}\right) \quad (3.22)$$

$mf$  is defined as the ratio of the frequency of the carrier signal to the frequency of the modulation signal.

$$m_f = \frac{f_c}{f_m} \quad (3.23)$$

To generate symmetric three phase waveforms,  $mf$  should be an integer multiple of 3 of the modulation frequency  $m_f = 3k, (k \in N)$  [57]. The SPWM procedure for the VSC shown for switches in leg 1 (phase A) shown in Figure 3-19 is described by:

- $A_m > A_c$ , S1 is ON, S2 is OFF,  $V_{out} = +VDC$
- $A_m < A_c$ , S1 is OFF, S2 is ON,  $V_{out} = -VDC$
- 

### 3.3.3 Modeling the PV Control System

The main objective of the PV control system as shown in Figure 3-18 is to transfer the maximum power available from the PV array to the grid [58]. The real and reactive power exchanged between the PV system and the grid is controlled in the  $dq$  reference frame

using a decoupled current-mode scheme. The control in the  $dq$  reference frame transforms the instantaneous, steady-state AC voltages and currents into DC signals, which simplifies the control design and parameter tuning process [55]. Current-mode control protects the VSC against high current conditions and provides robust dynamic response to transient events in the PV-grid system [58]. The AC-side dynamics of the PV-grid system shown in Figure 3-18 is described by:

$$v_a - v_{pa} = m_a \frac{V_{DC}}{2} - v_{pa} = Ri_a + L \frac{di_a}{dt} \quad (3.24)$$

$$v_b - v_{pb} = m_b \frac{V_{DC}}{2} - v_{pb} = Ri_b + L \frac{di_b}{dt} \quad (3.25)$$

$$v_c - v_{pc} = m_c \frac{V_{DC}}{2} - v_{pc} = Ri_c + L \frac{di_c}{dt} \quad (3.26)$$

The transformation of the AC voltages and currents to the  $dq$  reference frame is done using a transform angle  $\rho$  obtained by tracking the frequency of the grid side voltages (on the delta side of the transformer shown in Figure 3-18) using a phase locked loop (PLL) control. A prebuilt PLL component available in the RSCAD library was used to implement the PLL controller [31].

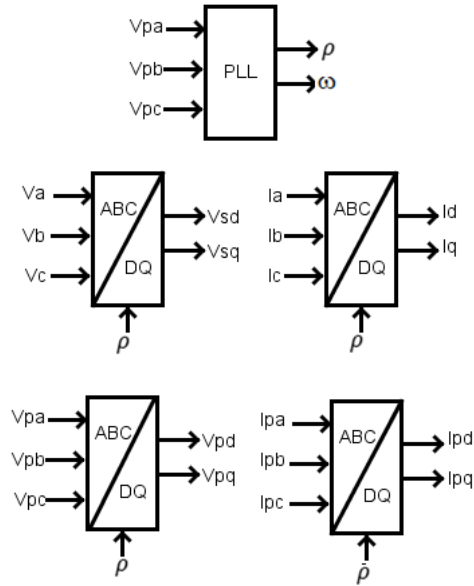


Figure 3-21 Phase locked loop and dq transform of AC side voltages and currents

Figure 3-22 shows the decoupled dq current control scheme described:

$$V_{sd} - V_{pd} = m_d \frac{V_{DC}}{2} - V_{pd} = Ri_d + L \frac{d}{dt} i_d - L\omega i_q \tag{3.27}$$

$$V_{sq} - V_{pq} = m_q \frac{V_{DC}}{2} - V_{pq} = Ri_q + L \frac{d}{dt} i_q + L\omega i_d \tag{3.28}$$

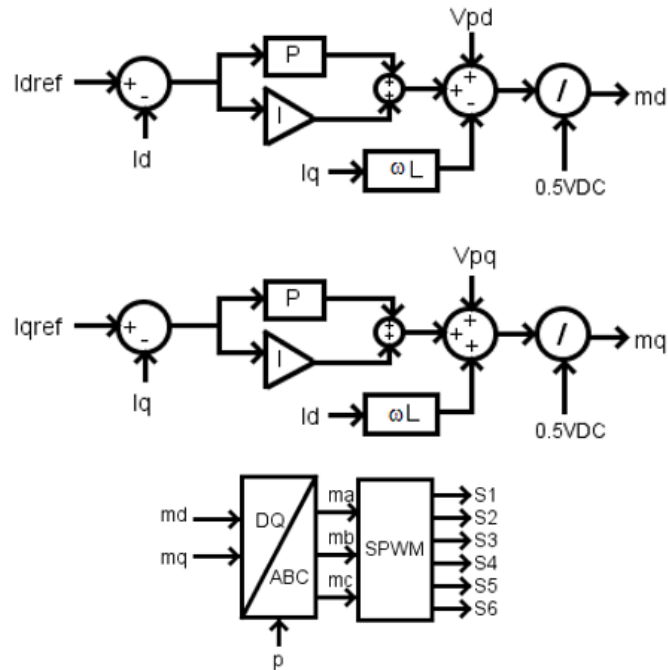


Figure 3-22 Decoupled dq current control

The output of the current controllers are the  $dq$  modulation indices,  $m_d$  and  $m_q$ , which are transformed to sinusoidal, three-phase signals and used as the modulation waveforms in the SPWM control described in section 3.3 to generate the firing pulses of the 2-level, VSC valves S<sub>1</sub>-S<sub>6</sub>. The proportional  $k_{p_{cc}}$  and integral gain  $k_{i_{cc}}$  parameters for the current control are selected using the following relationship given in [55]:

$$k_{p_{cc}} = \frac{L}{\tau_{cc}} \quad (3.29)$$

$$k_{i_{cc}} = \frac{R}{\tau_{cc}} \quad (3.30)$$

where  $\tau_{cc}$  is a design choice that determines the current control response time and is chosen such that the closed loop bandwidth of the current control is smaller than the VSC switching frequency [55]. Typical range of values for  $\tau_{cc}$  are 0.5msecs-5msecs [55].

The  $dq$  reference currents are obtained from the power balance between the DC side and AC side given by:

$$P_{DC} = V_{DC}I_{DC} = P_{AC} + P_{loss_{VSC}} \quad (3.32)$$

$$P_{GRID} = P_{AC} + P_{loss_R} + P_{loss_{Trf}} \quad (3.33)$$

$$Q_{GRID} = Q_{AC} + Q_{filt_c} \quad (3.34)$$

$$P_{AC} = v_a i_a + v_b i_b + v_c i_c \quad (3.35)$$

$$Q_{AC} = \frac{v_a * (i_b - i_c) + v_b * (i_c - i_a) + v_c * (i_a - i_b)}{\sqrt{3}} \quad (3.36)$$

The power balance in the  $dq$  reference frame, assuming negligible losses and that at steady state the  $q$  component of the grid voltage  $V_{pq}$  is regulated to zero by the PLL, is given by:

$$P_{ref} = \frac{3}{2} (V_{pd} i_{dref}) \quad (3.37)$$

$$Q_{ref} = \frac{3}{2}(-V_{pd} i_{qref}) \tag{3.38}$$

From the power balance equations, the  $d$  axis and the  $q$  axis current controllers independently regulate the real and reactive power exchanged in the PV-grid-connected system. Typically,  $Q_{ref}$  is set to zero for unity power factor operation so the PV system does not regulate the AC voltage at the point of connection. The advantage of using the reactive power capability was discussed in Chapter 2.  $Q_{ref}$  can be set to a value within the reactive power limits of the PV inverter. For example, if the PV converter system is rated at 2MW with a power factor of  $\pm 0.95$  (lag/lead), the reactive power can range between  $\pm 0.6574$  MVAR within the reactive power capability of the power converter.  $Q_{ref}$  can also be set by a voltage regulation control, which maintains the PCC voltage at the reference level by delivering a certain amount of reactive power [55]. Figure 3-23 shows the two methods for setting the q current reference with a compensation factor for the AC filter capacitance included to obtain the desired current reference for the current control loop.  $V_{pdref}$  is set to the nominal peak value of the line to neutral voltage at the PV-grid system PCC [55].

$$V_{pdref} = \frac{\sqrt{2}|v_{pd}|_{LL,rms}}{\sqrt{3}} \tag{3.39}$$

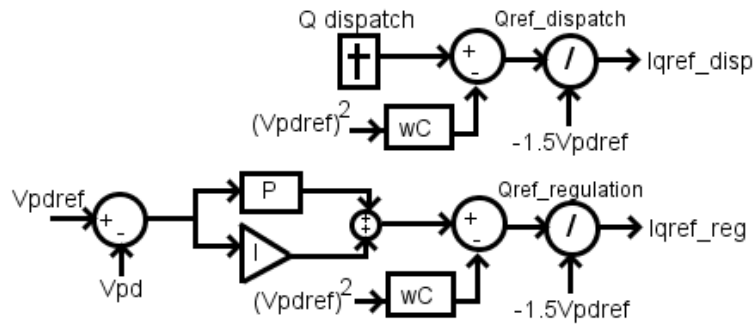


Figure 3-23 Methods to obtain q current control reference

A method to obtain suitable parameters for the proportional  $k_{pvac}$  and integral gain  $k_{i\_vac}$  for the AC bus voltage regulation control is discussed in [55] and described by:

$$k_{p\_vac} = C\omega_m \quad (3.40)$$

$$k_{i\_vac} = \alpha_{vac}k_{p\_vac} \quad (3.41)$$

$$\omega_m = \sqrt{\tau_{cc}^{-1}\alpha_{vac}} \quad (3.42)$$

$$\sin\delta_{vac} = \frac{1 - \tau_{cc}\alpha_{vac}}{1 + \tau_{cc}\alpha_{vac}} \quad (3.43)$$

Where  $\delta_{vac}$  is a compensation angle selected in the range of  $30^0 - 90^0$ .

$P_{ref}$  is obtained using a DC link voltage regulation control shown in Figure 3-24, which controls the DC bus voltage  $V_{DC}$  to the given reference voltage obtained from a maximum power point tracking control [55].

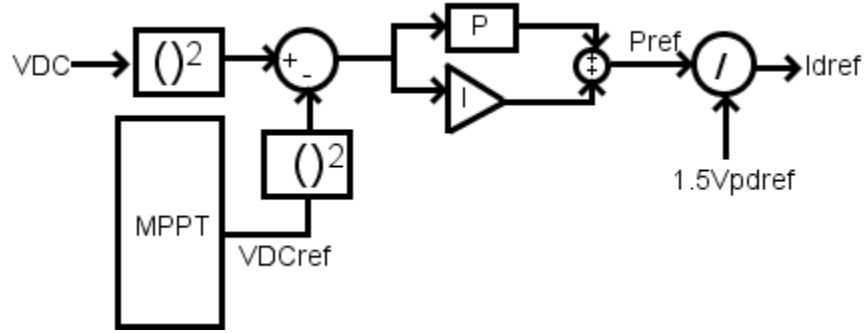


Figure 3-24 PV DC link voltage regulation and MPPT control

A PI control is used to obtain the desired power reference according to the DC side dynamics described by [55]:

$$V_{DC}I_{PV} - V_{DC}I_{DC} = \frac{C_{DC}dV_{DC}^2}{dt} \quad (3.44)$$

The proportional  $k_{p\_vdc}$  and integral gains  $k_{i\_vdc}$  are selected so that the closed loop response  $\tau_{vdc}$  of the DC bus regulation is slower than the closed loop response  $\tau_{cc}$  of the  $dq$  current control [55].

Table 3-6 shows the proportional and integral gain values for the PV system controllers.

**Table 3-5 Proportional and Integral gains for PV controllers**

Decoupled dq current control	$k_{p_{cc}} = 0.025, k_{i_{cc}} = 0.5, \tau_{cc} = 4ms$
AC bus voltage control	$k_{p_{vac}} = 0.0125, k_{i_{vac}} = 0.4, \delta_{vac} = 82^0$
DC bus voltage control	$k_{p_{vdc}} = 1, k_{i_{vdc}} = 5$

The DC side capacitance should be sufficiently large to reduce ripples on the DC bus voltage. A method to select a suitable DC side capacitance to minimize ripples on the DC bus voltage is discussed in [59] and described by:

$$C_{DC} \geq \frac{P_{DC_{rated}}}{240 * V_{ripple} * |v_{pd}|_{LL_{rms}} * f_{grid}} \quad (3.45)$$

$$V_{ripple} \leq (1\% - 5\%)V_{DC_{rated}} \quad (3.46)$$

The DC bus voltage is selected to be greater than two times the nominal peak value of the line to neutral voltage at the point of connection of the PV-grid system [55].

$$V_{DC} > \frac{2\sqrt{2}|v_{pd}|_{LL_{rms}}}{\sqrt{3}} \quad (3.47)$$

The DC bus voltage reference  $V_{DC_{ref}}$  is obtained from a MPPT method which, is designed to track the maximum power point of the PV array under varying insolation and temperature conditions. Figure 3-25 shows several methods used for tracking the maximum power point of PV arrays which can be classified as direct and indirect tracking techniques [60, 61].

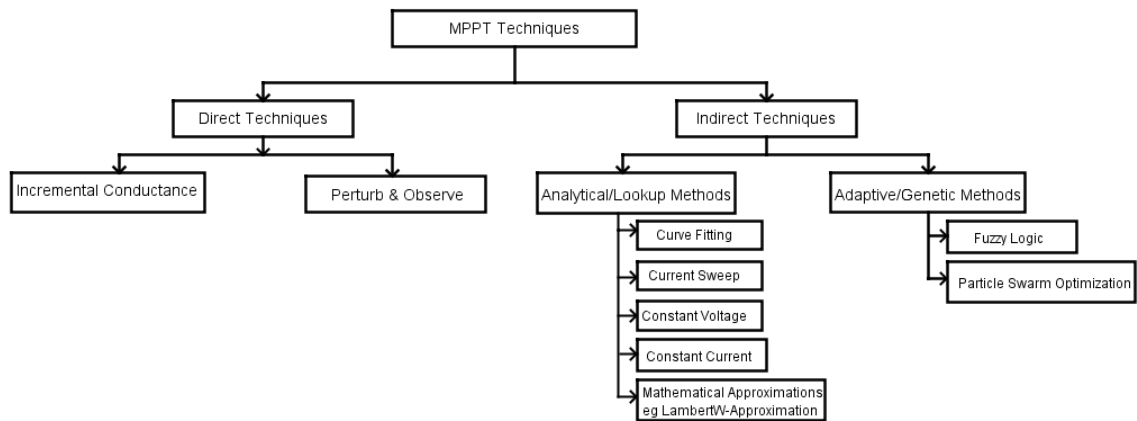


**Figure 3-25 Maximum power point tracking techniques**

Direct methods such as the perturbation & observation (P&O) and incremental conductance (INC) methods are commonly used due to their reduced implementation complexity and computation requirements [61]. The disadvantage of direct methods is they have inherent oscillations at the maximum power point which increase power losses in the PV system. In addition direct methods can become confused when tracking the maximum power point under rapidly changing environment conditions [61]. Indirect maximum power point tracking techniques offer rapid tracking under varying environmental conditions with minimal oscillations at the maximum power point but are more complex to implement in practise as they require more knowledge of the operating conditions of the PV array leading to an increase in computation requirements compared to direct methods [61]. In this thesis, the incremental conductance algorithm is used to obtain the DC bus voltage reference. The INC algorithm uses the idea that the slope of the P-V curve is zero at the MPP, negative at points greater than the MPP and positive at points less than the MPP as described by [62]. For a given isolation and temperature condition, the DC bus voltage reference is either increased or decreased by the MPPT control using a specified step size

$dV$  and MPPT sampling time to track the new maximum power point. The flow chart of the incremental conductance method is shown in Figure 3-26.

$$\frac{dP_{PV}}{dV_{PV}} = \frac{d(V_{PV}I_{PV})}{dV_{PV}} = V_{PV} \frac{dI_{PV}}{dV_{PV}} + I_{PV} \tag{3.44}$$

$$\frac{dI_{PV}}{dV_{PV}} = -\frac{I_{PV}}{V_{PV}} \text{ for } \frac{dP_{PV}}{dV_{PV}} = 0 \text{ (MPP)} \tag{3.45}$$

$$\frac{dI_{PV}}{dV_{PV}} < -\frac{I_{PV}}{V_{PV}} \text{ for } \frac{dP_{DC}}{dV_{PV}} < 0 (> \text{MPP}) \tag{3.46}$$

$$\frac{dI_{PV}}{dV_{PV}} > -\frac{I_{PV}}{V_{PV}} \text{ for } \frac{dP_{PV}}{dV_{PV}} < 0 (> \text{MPP}) \tag{3.47}$$

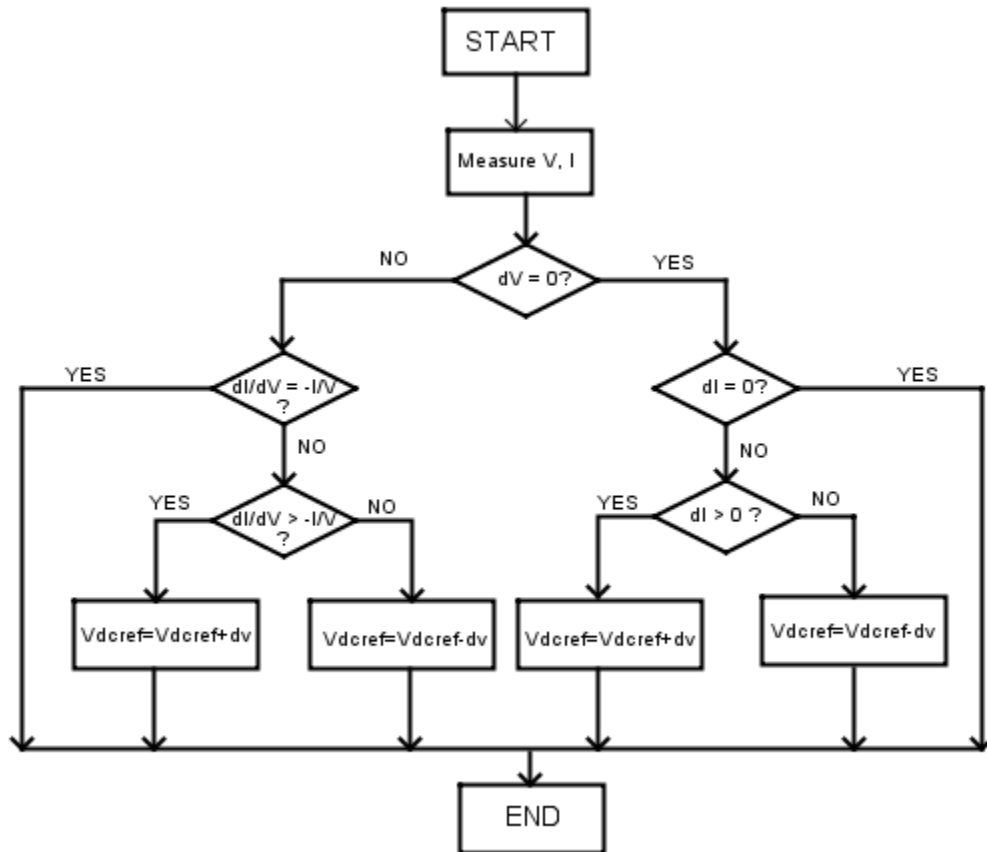


Figure 3-26 Flowchart of incremental conductance algorithm

### 3.3.4 Simulation of the PV System

Figure 3-27 shows the RSCAD Runtime model for simulating and controlling the PV system. The VSC's AC side is interfaced to a  $3\Omega\angle 86^\circ$ , 60Hz grid using a 2.5MVA, 0.48/13.2kV, delta-wye transformer. The PV system is rated to deliver 1.74 MW at a DC bus voltage rating of 2kV at the reference (STC) insolation and temperature condition of  $1000\text{W}/\text{m}^2$  and  $25^\circ\text{C}$ . The capacitance of the AC-side filter is set to  $2500\mu\text{F}$ . A 1MW dynamic load is connected at the point of connection to study the power flow dynamics between the PV system and the grid.

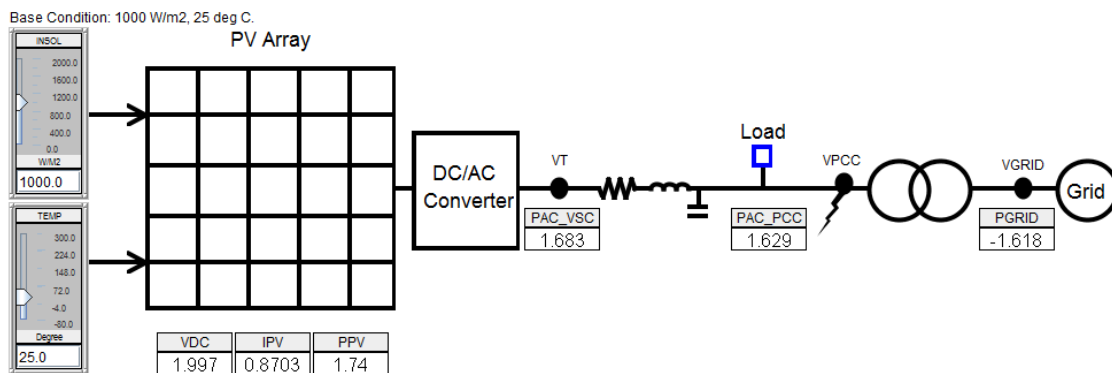


Figure 3-27 RSCAD Runtime for PV Simulation

Figure 3-28 and Figure 3-29 show the I-V and P-V curves of the PV array parameters listed in Table 3-5 for solar insolation values from  $200\text{W}/\text{m}^2$  to  $1000\text{W}/\text{m}^2$ . The curves indicate a maximum power point for each insolation condition.

Table 3-6 PV Array Parameters

Ncs	36
Ncp	1
Voc_stc	21.7 V
Isc_stc	3.35 A
Vm_stc	17.4 V
Im_stc	3.05 A
Ki	0.065 %/degC
Eg	1.11eV
Prated	1.74 MW
Ns	115

Np	285
----	-----

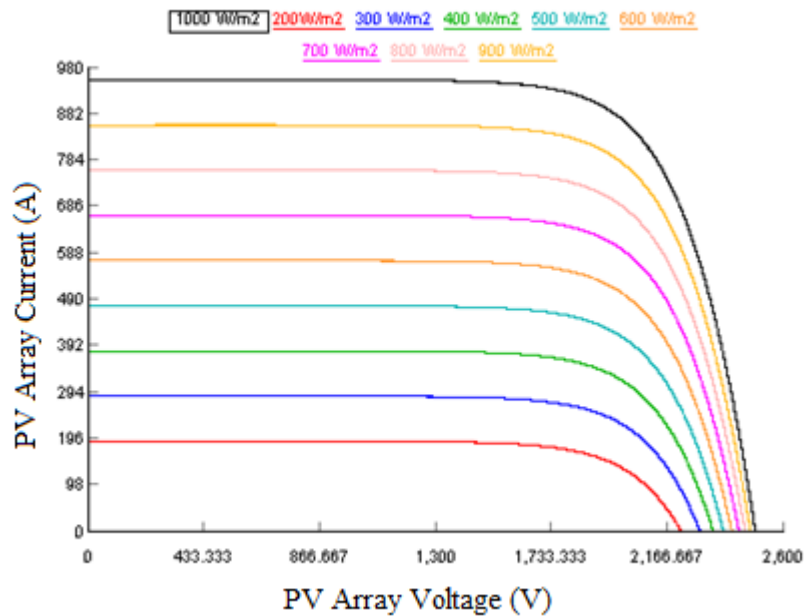


Figure 3-28 I-V curves for different insolation at T=25<sup>0</sup> C

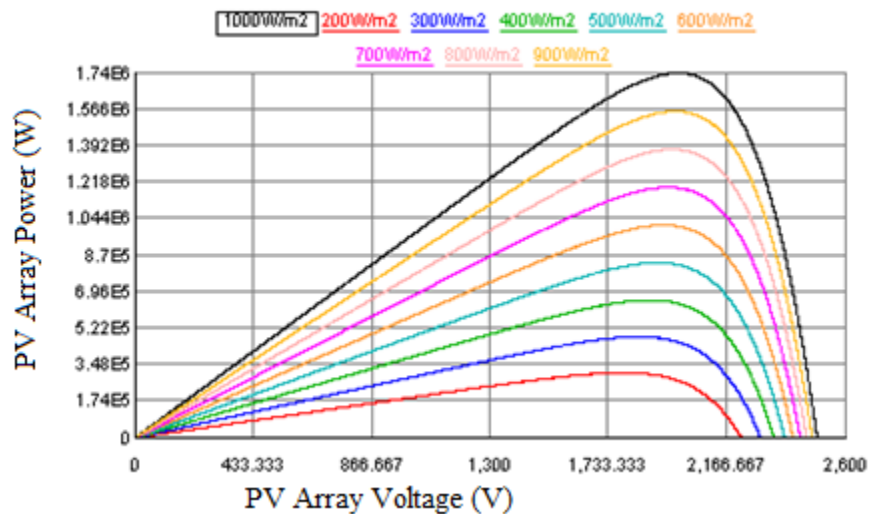
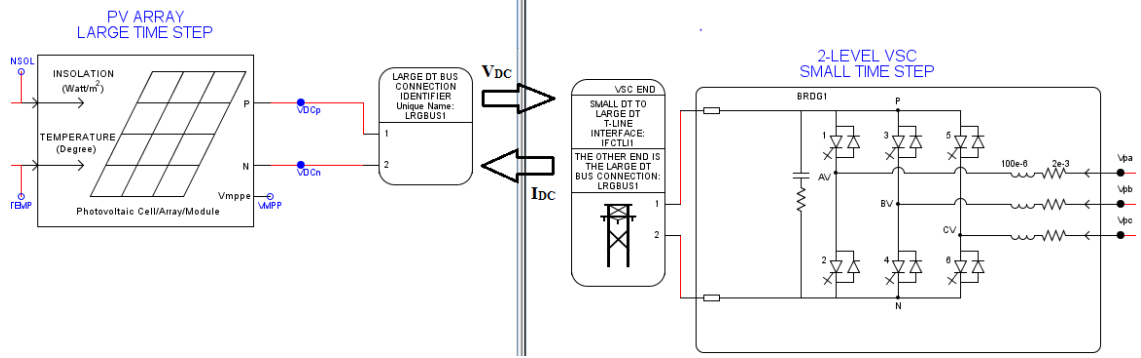


Figure 3-29 P-V curves for different insolation at T=25<sup>0</sup>C

The PV array is connected to the AC grid using the two-level, VSC modeled in the RSCAD small time step bridge box. The switching frequency of the VSC is set to be 21 times the grid frequency i.e 1620Hz. The interface between the PV array which is simulated with a large time step of 50μsecs and the 2-level, VSC which is simulated with a small time step

of  $2.5 \mu\text{secs}$  is done using a small time step to large time step transmission line interface model in RSCAD as shown in Figure 3-30.



**Figure 3-30 Interfacing the PV array with the 2-level VSC in RSCAD**

The interface transmission line adds an artificial inductance  $L_{line}$  and shunt capacitance  $C_{line}$  according to the travel time relationship described by [31]:

$$\tau_{line} = 1.39\Delta T_{large} = \sqrt{L_{line}C_{line}} \quad (3.48)$$

The impact of the artificial transmission line can be alleviated by taking the shunt capacitance value  $C_{line}$  to be a portion of the DC bus capacitor  $C_{DC}$ , which has a natural charging and discharging transient time delay.

Figure 3-31 shows the DC bus response to a ramp change in insolation from  $400 \text{ W/m}^2$  to  $1000 \text{ W/m}^2$ . The step size  $dV$  and sampling period  $T_{samp}$  for the INC MPPT were set to value  $5 \text{ V}$  and  $200 \text{ ms}$  ( $5 \text{ Hz}$ ), respectively. The initialization time of the INC method was set to  $5$  seconds and during this time the initial value of the DC bus voltage reference was set to  $80\%$  of the measured open circuit voltage of the PV array [56]. The open circuit voltage is given as an output from PV model. The selected step size and sampling period for the INC is shown to offer rapid tracking with minimum oscillations at the maximum power point.

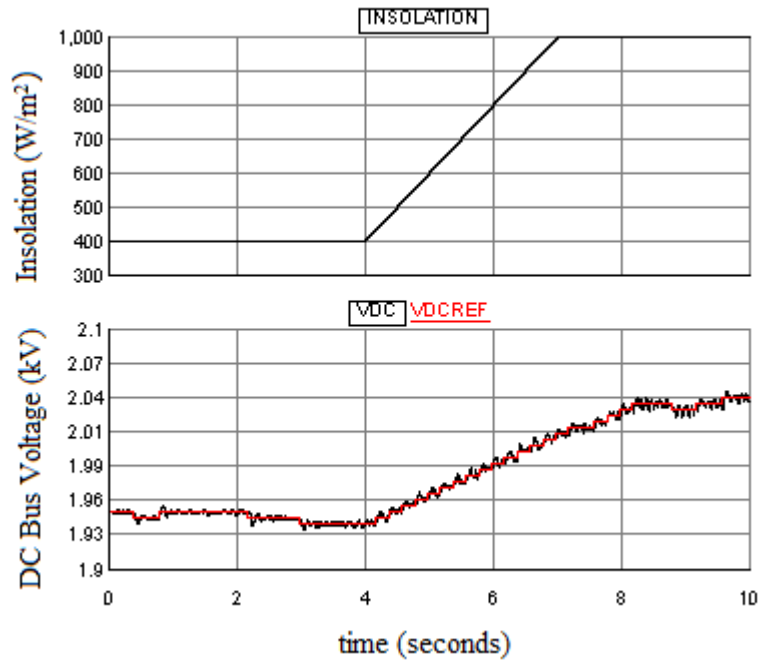


Figure 3-31 DC Bus voltage response to changing insolation

The variation of the PV array power to the ramp change in insolation is shown in Figure 3-32. The efficiency of the DC/AC power conversion stage remains above 95%.

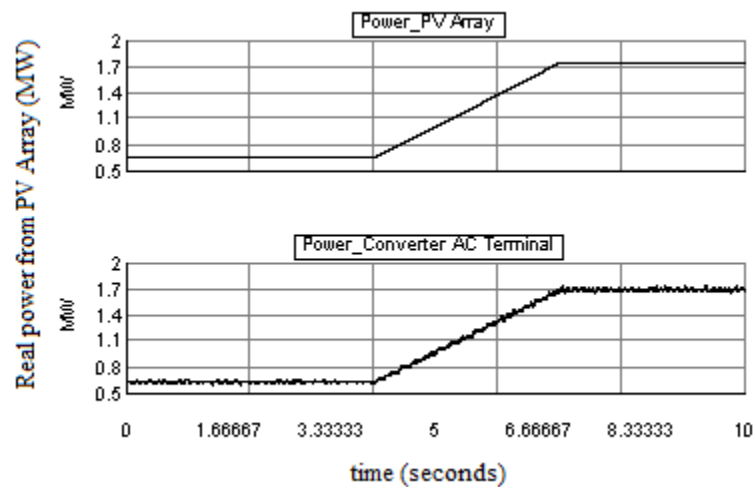


Figure 3-32 Increasing PV array power (DC and AC side) to increasing insolation

The variation of the power delivered to the grid by the PV array to the ramp change in insolation is shown in Figure 3-33. The power produced by the PV array increases as the

insolation increases and consequently the power supplied by the grid to the load reduces showing the intermittent nature of the power supplied by renewable PV DERs.

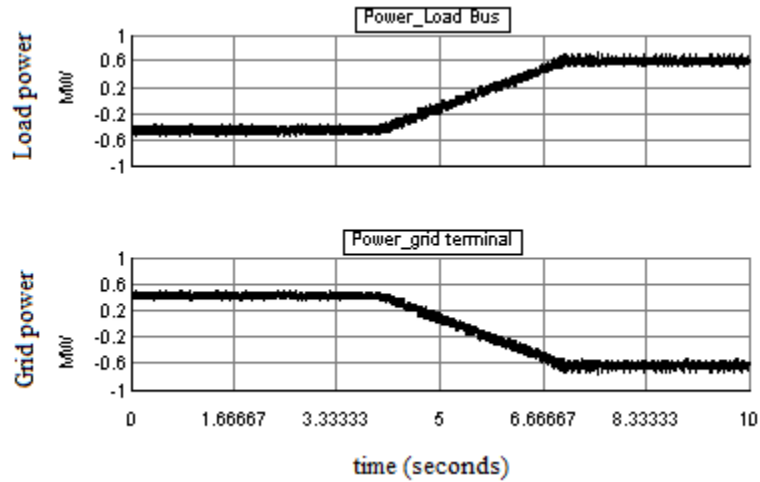


Figure 3-33 Grid response to varying solar insolation

To demonstrate the reactive power capability of the PV inverter for voltage regulation, the load on the transformer’s delta winding was decreased from 1MW to 0.1MW as shown in Figure 3-34. The delta winding’s bus voltage response with and without the voltage regulation control is shown in Figure 3-35.

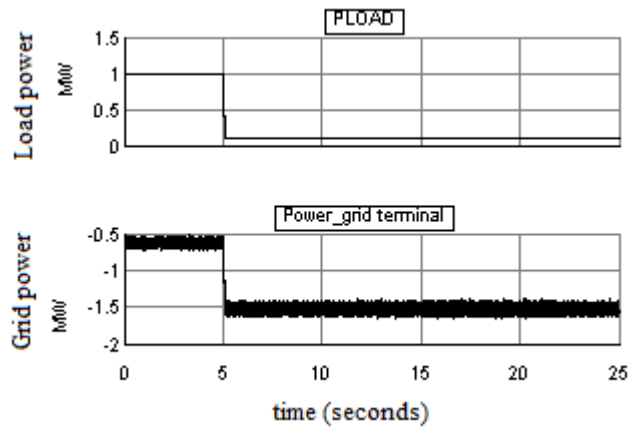


Figure 3-34 Step Change in Load for PV voltage regulation

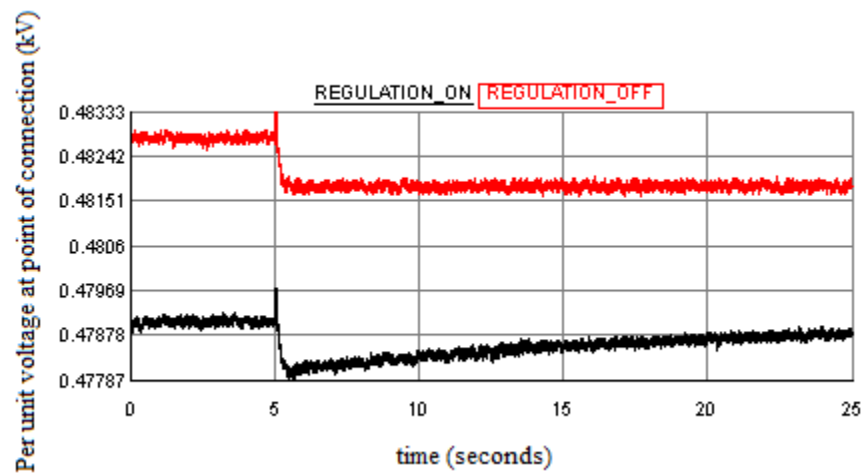


Figure 3-35 PV-grid PCC bus response to step change in load with and without voltage regulation.

Figure 3-35 shows that the voltage regulation lowers the value of the PCC bus voltage compared to when the voltage regulation is disabled (unity power factor operation). This demonstrates the capability of using the reactive power capability of power converters for voltage regulation to keep bus voltages within the specified voltage limits and provide grid voltage support to distribution networks with converter interfaced renewable energy systems.

### 3.4 Wind Energy System Model

Wind energy systems convert the kinetic energy in the wind into electrical power, which can be delivered to the grid or used in off-grid applications to supply local loads.

Wind turbines are grouped into two categories based on the axis of rotation namely: *horizontal axis wind turbines* (HAWT) and *vertical axis wind turbines* (VAWT). Wind turbines are further classified based on the speed of operation into *fixed speed* and *variable speed* wind turbines. Fixed speed wind turbines have optimum operation at a constant wind

speed while variable wind speeds can operate over a wider wind speed range. The output of modern wind turbines range from 10kW for small wind turbines to 5MW for large wind turbines [57]. The most common configuration used in modern wind turbines is the variable speed, 3 bladed upwind HAWT due to its advantage of higher wind energy conversion efficiency, better controllability, and improved aerodynamic performance over a wide wind speed range [57]. In this research, the doubly fed induction generator (DFIG) wind turbine system shown in Figure 3-36 is discussed and implemented.

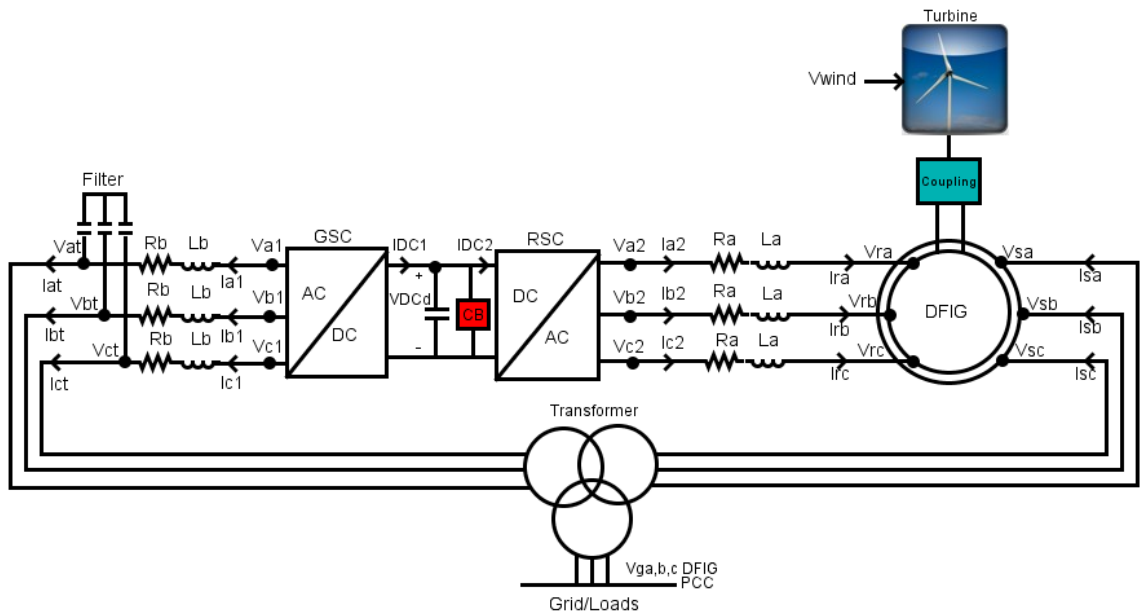


Figure 3-36 DFIG wind energy system

### 3.4.1 Doubly Fed Induction Generator (DFIG)

The doubly fed induction generator is used to convert the wind turbine's mechanical power to electrical power. Transformers are used to step up or down the wind turbine's voltage typically in the range of 0.69 – 2kV before connection to the grid/load. In addition, transformers are used to isolate the grid from the wind turbine system.

A gearbox may be used to convert the low speed of the wind turbine rotor ( $\leq 20\text{rpm}$ ) to the high speed of the generator (1000rpm – 1800rpm). The gearbox ratio is given by [57]:

$$r_{gb} = \frac{n_{turbine} (rpm)}{n_{generator} (rpm)} = \frac{(1 - s)60 f_s}{n_{generator} P} \quad (3.49)$$

where  $P$  is the number of generator pole's pairs,  $s$  is the rated slip and  $f_s$  is the rated grid frequency in Hz [57]. Direct drive wind turbine systems with low speed, high pole generators do not require a gearbox and are connected directly to the wind turbine rotor shaft reducing the required maintenance and overall cost of the wind turbine system [57]. The energy from the wind is captured through the rotor and blades. The mechanical power output of a wind turbine is related to its rotor size by equation (3.25) where  $V_w$  is the wind velocity,  $A$  is the area swept by the rotor and  $\rho$  is the density of air [63].

$$P_m = 0.5C_p\rho AV_w^3 \quad (3.50)$$

The blade power coefficient  $C_p$  determines the amount of kinetic energy in the wind converted to mechanical energy by the wind turbine. The blade power coefficient  $C_p$  for modern wind turbines ranges from 0.2-0.5 with a maximum limit of 0.59 called the Betz limit. The blade power coefficient is a function of the tip speed ratio  $\lambda$  and the blade pitch angle  $\beta$  which is the angle between the wind speed direction and the surface of the wind turbine blades [63].

The tip speed ratio  $\lambda$  is the ratio of the rotor tip speed  $\omega_m$  to the wind velocity,  $V_w$  and for a rotor with radius  $R$ , it is given by [63].

$$\lambda = \frac{R\omega_m}{V_w} \quad (3.51)$$

The variation of the wind turbine blade power coefficient  $C_p$  with tip speed ratio  $\lambda$  is shown in Figure 3-37. The curves indicate an optimal tip speed ratio  $\lambda$  for a given pitch angle  $\beta$

which determines the maximum power that can be extracted by the wind turbine at a given wind speed  $V_w$ .

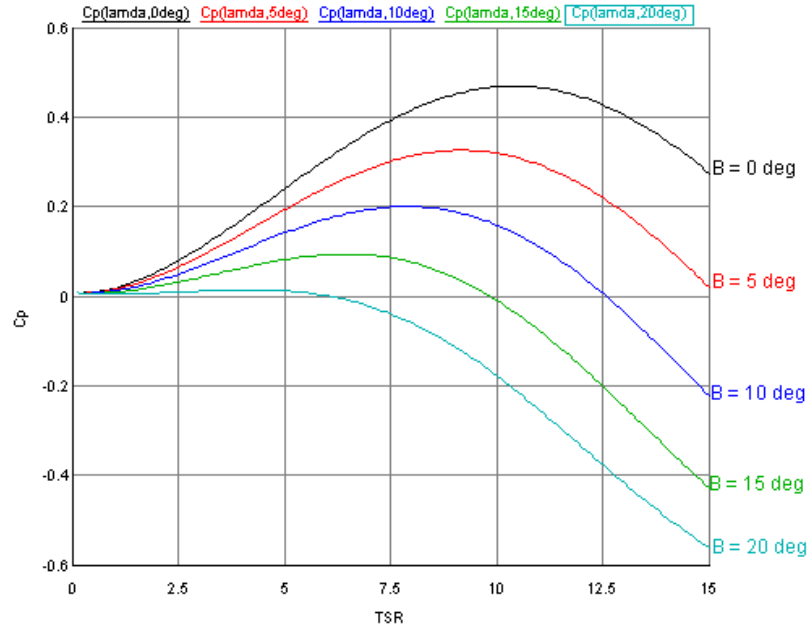


Figure 3-37 Power coefficient curves ( $C_p$ ) vs tip speed ratio (TSR) ( $\lambda, \beta$ ) [31]

The drivetrain is represented using a two mass model shown in Figure 3-38, which ignores the inertia of the gearbox and includes the rotating mass of the wind turbine and the generator [64].

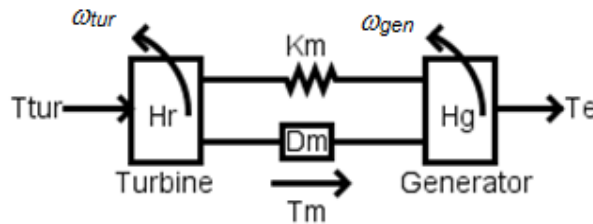


Figure 3-38 Two mass model of the wind turbine drive train

The dynamics of the two-mass model is described by [64]:

$$T_{tur} - T_m = 2H_r \frac{d\omega_r}{dt} \tag{3.52}$$

$$T_m - T_e = 2H_g \frac{d\omega_g}{dt} \tag{3.53}$$

$$T_m = D_m(\omega_r - \omega_g) + K_m \int (\omega_r - \omega_g) dt \quad (3.54)$$

Where  $T_{tur}$  is the wind turbine's mechanical torque,  $T_m$  and  $T_e$  are the generator's mechanical and electrical torque,  $H_r$  and  $H_g$  are the turbine and generator inertia constants,  $K_m$  and  $D_m$  are the stiffness and damping of the mechanical connection between the turbine and generator [64]. Figure 3-39 shows the RSCAD models used for simulating the wind turbine and drive train system [31].

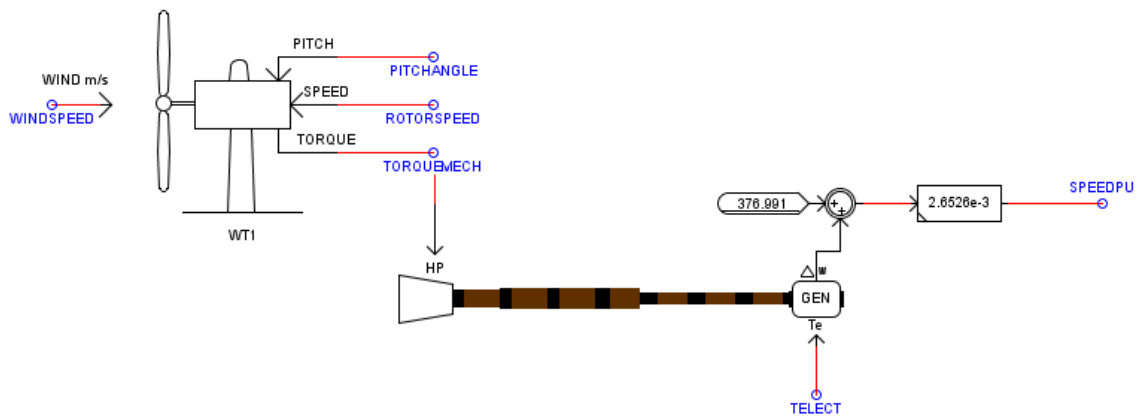
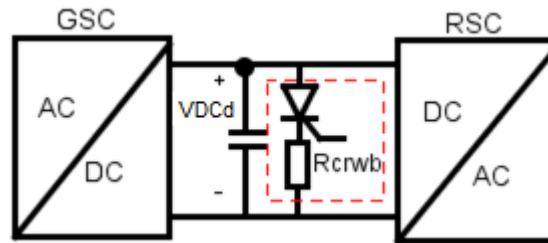


Figure 3-39 RSCAD Model of Wind Turbine and Drive Train [31]

As shown in Figure 3-36, the stator of the DFIG is connected directly to the grid and the rotor is connected to the grid using two back to back power converters with a common capacitive DC link and an AC filter. The back to back, VSCs known as the grid side converter (GSC) and rotor side converter (RSC) control the power exchanged between the wind turbine and the grid. The back to back converters have a rated power of about 25-30% of the total DFIG wind power system resulting in reduced converter power losses and increased efficiency [57]. The interface reactors  $L_a$  and  $L_b$  control the real and reactive power flow between the converters and grid as well as provide some filtering of the converter harmonics injected to the grid [55]. Typically IGBT based, PWM VSCs are used in

DFIG applications allowing the simultaneous control of the active and reactive power exchanged between the grid and the generator [57]. The RSC may be subjected to DC link over-voltages and rotor circuit over-currents during grid faults. Crowbar circuits (CB) protect the RSC by short circuiting the rotor windings enabling the DFIG to remain connected to the grid during fault events [31]. The crowbar is modeled as a shunt conductance in series with a switch and is connected between the GSC and RSC of the DFIG as shown in Figure 3-40 [31].



**Figure 3-40 DFIG Crowbar Circuit.**

The crowbar switch is turned on when the dc link voltage exceeds a specified maximum value and is turned off when the dc link voltage drops below a minimum value. The value of the crowbar resistance affects the operation of the DFIG. High resistance values provide adequate damping to the fault transients when the crowbar is enabled but can create undesirable transients when the crowbar is turned off [65]. High resistance values provide adequate damping to the fault transients when the crowbar is enabled but can create undesirable transients when the crowbar is turned off [65].

The DFIG allows variable speed operation over a slip speed range (typically 0.7 – 1.2 pu) and has better controllability than other wind turbine generators without the need for additional mechanical parts and capacitors for reactive power compensation [66]. The power delivered by the rotor and stator side of the DFIG is given by [64]:

$$P_{stator} = \frac{P_m}{1 - slip} \quad (3.55)$$

$$P_{rotor} = -slip * P_{stator} \quad (3.56)$$

$$slip = \frac{\omega_{stator} - \omega_m}{\omega_{stator}} = \frac{\omega_{rotor}}{\omega_{stator}} \quad (3.57)$$

$$P_{grid} = P_{stator} + P_{rotor} \quad (3.58)$$

### 3.4.2 Modeling the DFIG control system

Control systems are required for the reliable and safe operation of the DFIG system over a wide wind speed range. The control of the DFIG wind energy system is based on [31, 67] and is described as follows:

- **Pitch angle control**

The electrical power output of a wind turbine at various wind speeds is indicated by its power-wind speed curve as shown in Figure 3-41.

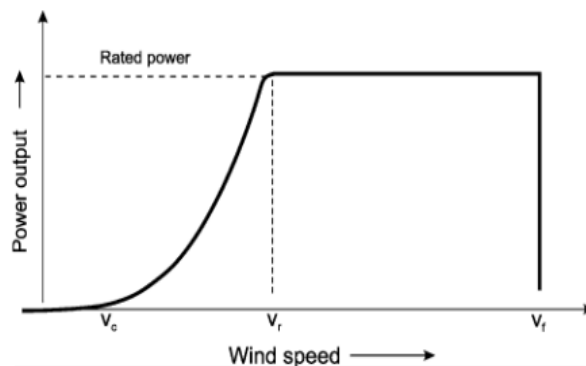


Figure 3-41 Wind system power-speed curves [68]

The power-speed curves indicate the cut in wind speed  $V_c$  (3-5m/s) where the wind turbine starts to operate, the rated wind speed  $V_r$  (12-15m/s) where rated power operation is achieved and the cut out wind speed  $V_f$  ( $\geq 25$ m/s) at which the wind turbine is designed to stop operation to avoid mechanical damage due to excessive wind speeds [68]. The function of the pitch angle control shown in Figure 3-42 is to change the pitch angle of the wind turbine blades for wind speeds greater than  $V_r$  to reduce rotor blade rotations and frequency oscillations caused by high wind speeds [68]. Due to the large inertia of the rotor blades, the pitch angle has a slow rate of change and is limited to protect the wind turbine during grid fault events and high wind speeds [64].

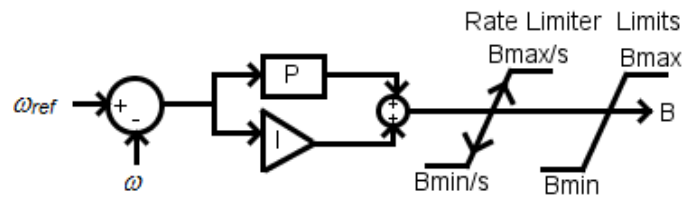


Figure 3-42 Pitch angle control

- **Maximum power point tracking control**

For wind speeds between the cut-in and rated speed range [ $V_c - V_r$ ], the pitch angle is set to zero and a MPPT control strategy is used to track the maximum power of the wind turbine at the given wind speed. Commonly used MPPT methods are *optimal tip speed ratio* where the optimum rotor speed for a given wind speed is calculated based on the known optimum tip speed ratio which is constant for a given blade [69]; *turbine power feedback control* which measures the rotor speed at a given wind speed and calculates the maximum power from the known power curve of the wind turbine [69] and *optimal torque control* which uses the idea that for a given gearbox ratio, the turbine's mechanical torque and speed can be converted to the generator torque and speed from which the optimum

torque can be calculated using the generator rated parameters [69]. The optimum torque control (OTC) shown in Figure 3-43 is used in this work. Limits are placed to avoid damage to the wind turbine when the rotor speed exceeds a specified level [55].

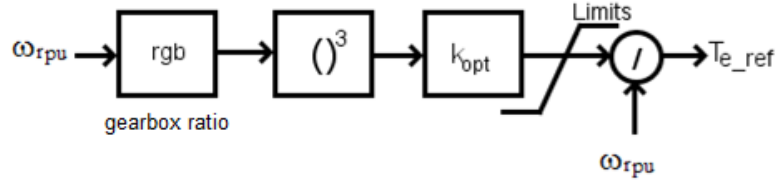


Figure 3-43 Optimal torque control for DFIG MPPT method

The input to the OTC control is the turbine speed and the output is the electrical torque reference that indicates the maximum power in the wind. The optimum torque coefficient  $k_{opt}$  can be obtained from the maximum power coefficient  $C_{p_{max}}$  as described by [69]:

$$C_p(\lambda_{opt}, \beta=0) = C_{p_{max}} \quad (3.59)$$

$$P_{m,optimum} = k_{opt} \omega_{m,opt}^3 \quad (3.60)$$

$$T_{m,opt} = k_{opt} \omega_{m,optimum}^2 \quad (3.61)$$

$$\omega_{m,opt} = \frac{\lambda_{opt} V_w}{R} \quad (3.62)$$

$$k_{opt} = \frac{0.5\pi\rho C_{p_{max}} R^5}{\lambda_{opt}^3} \quad (3.63)$$

- **Grid Side Converter (GSC) control**

The function of the GSC is to control the DC link voltage to a constant reference value and provide reactive power support to the grid voltage at the point of connection (PCC) during fault events [57].

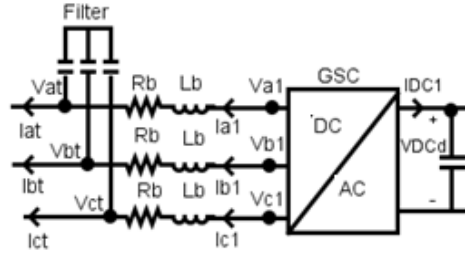


Figure 3-44 GSC voltages and currents

The voltage equations across the GSC R-L reactor as shown in Figure 3-44 is given by [55]:

$$v_{at,bt,ct} = R_b i_{a,b,c1} + L_b \frac{d}{dt} i_{a,b,c1} + v_{a1,b1,c1} \quad (3.64)$$

In dq reference frame:

$$V_{dt\_gsc} = V_{dref1} = R_b I_{d1} + L_b \frac{d}{dt} I_{d1} - \omega_e L_b I_{q1} + V_{d1} \quad (3.65)$$

$$V_{qt\_gsc} = V_{qref1} = R_b I_{q1} + L_b \frac{d}{dt} I_{q1} + \omega_e L_b I_{d1} + V_{q1} \quad (3.66)$$

The decoupled  $dq$  current mode control described in section 3.3.2 is used for the GSC to allow the independent control of the DC link voltage and reactive power injected to the grid during fault events. The  $d$  axis control regulates the DC bus voltage to the DC bus voltage reference  $V_{DCrefd}$  which should be greater than 2 times the peak-peak, line to neutral grid voltage at the point of common connection (PCC) and should be set to a value that accounts for the maximum grid voltage during system transients [67].

The reactive power and consequently the power factor of the DFIG system is controlled by the  $q$  axis current controller. The reactive power reference  $Q_{set\_gsc}$  is set to *zero* for unity power factor, *greater than 0* for lagging power factor and *less than 0* for leading power factor within the reactive power limits of the GSC. Figure 3-45 – 3-47 show the decoupled current control for the GSC.

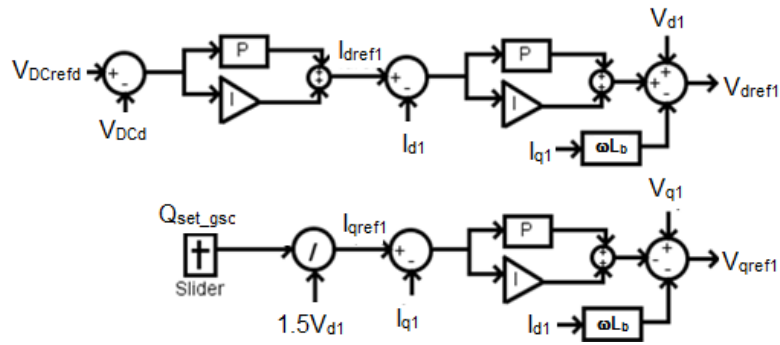


Figure 3-45 Grid side converter *dq* current control

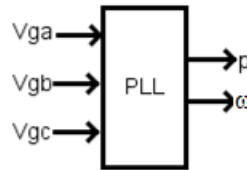


Figure 3-46 Phase locked loop of grid three phase voltages

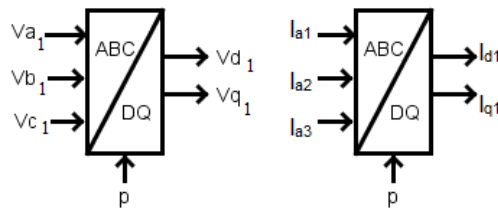


Figure 3-47 dq transform of GSC AC voltages and currents

The output of the current controllers are the voltage reference *dq* modulation indices, which are transformed to sinusoidal, three phase signals and used as the modulation waveforms in the SPWM control described in section 3.3 to generate the firing pulses of the GSC as shown in Figure 3-48.

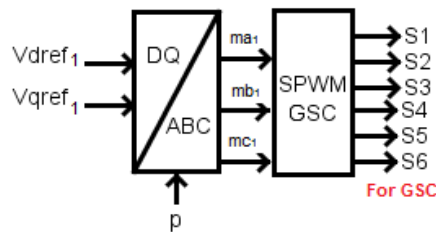


Figure 3-48 Firing pulse generation for GSC using SPWM

- **Rotor Side Converter (RSC) control**

The function of the RSC shown in Figure 3-49 is to control the electrical torque and power factor of the DFIG which respectively controls the real and reactive power exchanged between the rotor circuit and the grid. The RSC control is done using the stator flux vector orientation scheme where the  $dq$  axis are aligned with the stator flux allowing the simultaneous control of the electrical torque/real power and rotor excitation current/reactive power of the DFIG [67].

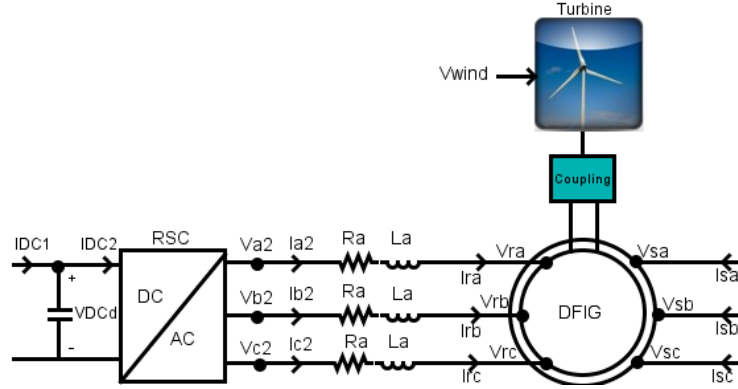


Figure 3-49 Rotor side converter voltages and currents

The equations that describe the relationship between the electrical torque  $T_e$ ; the total reactive power  $Q_g$ ; the stator and rotor flux linkages; the rotor and stator voltages and currents in the  $dq$  reference axis are given by [67].

$$v_{dr} = v_{dr}' - \omega_{slip} \sigma L_r i_{qr} = v_{dr}' - (\omega_s - \omega_r) \sigma L_r i_{qr} \quad (3.67)$$

$$v_{qr} = v_{qr}' + \omega_{slip} (L_m i_{ms} + \sigma L_r i_{dr}) \quad (3.68)$$

$$v_{dr}' = R_r i_{dr} + \sigma L_r \frac{di_{dr}}{dt} \quad (3.69)$$

$$v_{qr}' = R_r i_{qr} + \sigma L_r \frac{di_{qr}}{dt} \quad (3.70)$$

$$\lambda_s = \lambda_{ds} = L_o i_{ms} = L_s i_{ds} + L_o i_{dr} \quad (3.71)$$

$$\lambda_{dr} = \frac{L_o^2}{L_s} i_{ms} + \sigma L_r i_{dr} \quad (3.72)$$

$$\lambda_{qr} = \sigma L_r i_{dr} \quad (3.73)$$

$$i_{qs} = \frac{-L_o}{L_s} i_{qr} \quad (3.74)$$

$$\sigma = 1 - \frac{L_o^2}{L_s L_r}; \quad (3.75)$$

$$L_o^2 = L_m L_s; L_s = L_m + L_{ls}; L_r = L_m + L_{lr} \quad (3.76)$$

$$T_e = -\frac{3}{2} P L_m i_{ms} i_{qr} \quad (3.77)$$

$$Q_q = \frac{L_m v_{qs}}{L_s} \left( \frac{v_{qs}}{\omega_s L_m} + i_{dr} \right) - \frac{v_{qs}^2}{\omega_s L_s} \quad (3.78)$$

where  $\lambda_{dr}, \lambda_{ds}$  and  $\lambda_{qr}, \lambda_{qs}$  are the  $dq$  stator and rotor flux linkages;  $L_s, L_r$  are the stator and rotor inductances;  $L_{ls}, L_{lr}$  are the stator and rotor leakage inductances;  $L_m$  is the magnetizing inductance;  $i_{ms}$  is the stator magnetizing current;  $i_{dr}, i_{ds}$  and  $i_{qr}, i_{qs}$  are the  $dq$  stator and rotor currents;  $v_{dr}, v_{ds}$  and  $v_{qr}, v_{qs}$  are the  $dq$  stator and rotor voltages;  $R_r$  and  $R_s$  are the rotor and stator resistances;  $\omega_{slip}$  is the slip frequency;  $\omega_s, \omega_r$  are the stator and rotor angular frequencies;  $P$  is the number of poles.

As shown in Figure 3-50, the rotor phase currents are transformed to the  $dq$  axis using the slip angle  $\theta_{slip}$  which is the angle between the stator flux vector  $\theta_s$  and the rotor angle  $\theta_r$  [67].

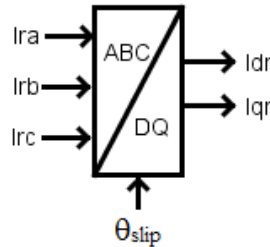


Figure 3-50 ABC-dq RSC

$$\theta_{slip} = \theta_s - \theta_r \quad (3.79)$$

The rotor angle  $\theta_r$  is output from the DFIG model [31] while the stator flux angle is given by [67].

$$\theta_s = \tan^{-1} \frac{\lambda_{\beta s}}{\lambda_{\alpha s}} = \tan^{-1} \frac{\int (v_{\alpha s} - R_s i_{\alpha s}) dt}{\int (v_{\beta s} - R_s i_{\beta s}) dt} \quad (3.80)$$

$$\omega_s = \frac{d\theta_s}{dt} \quad (3.81)$$

$$\lambda_s = \sqrt{\lambda_{\alpha s}^2 + \lambda_{\beta s}^2} \quad (3.82)$$

Where  $\lambda_{\beta s}, \lambda_{\alpha s}; v_{\alpha s}, v_{\beta s}; i_{\alpha s}, i_{\beta s}$  are the alpha-beta transform of the stator flux, stator voltages and stator currents [67]. Figure 3-51 shows the  $dq$  current control of the RSC where the d axis regulates the rotor current and subsequently the reactive power output and the q axis controls the electrical torque and subsequently the real power delivered to the grid by the DFIG as indicated by equations (3.67) - (3.78).

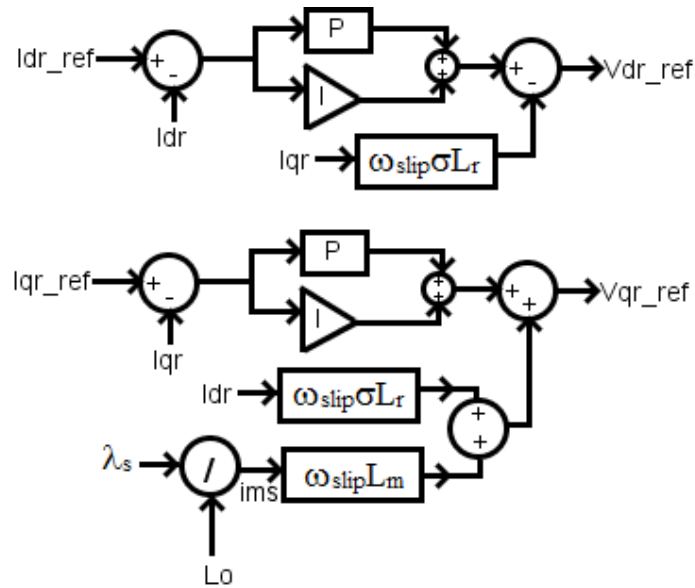
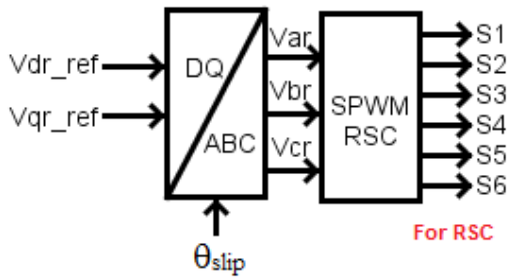


Figure 3-51 RSC dq current control

$I_{dr\_ref}$  is set to zero to minimize the VSC AC side currents and power losses in the VSC and rotor circuit [55].  $I_{qr\_ref}$  is determined from the torque equation given by:

$$T_{e\_ref} = -\frac{3}{2}P L_m i_{ms} i_{qr\_ref} \quad (3.83)$$

$T_{e\_ref}$  is obtained using the optimum torque MPPT control. The output of the RSC current control are the  $dq$  rotor voltage references used to create the rotor modulation waveforms for the SPWM control used to generate the switching sequence for the RSC as shown in Figure 3-52.



**Figure 3-52 RSC Firing pulse generation using SPWM**

The proportional and integral gain parameters for the DFIG GSC and RSC controls are given in [31] and listed in Table 3-7.

**Table 3-7 DFIG RSC and GSC Control Parameters**

GSC dq current control	$k_{p\_gsc} = 0.35, k_{i\_gsc} = 10$
RSC dq current control	$k_{p\_rsc} = 1.387, k_{i\_rsc} = 0.02808$
GSC DC bus voltage control	$k_{p\_vdc\_gsc} = 1, k_{i\_vdc\_gsc} = 10$

### 3.4.3 Simulation of the DFIG Wind System.

Figure 3-53 shows the RSCAD model used to analyze the dynamic response of the DFIG system. The back to back DFIG converter and stator side is connected to the grid by a three winding 2.5MVA, 13.2kV/22.2kV/0.69kV wye-wye-wye transformer simulated using the small time step subnetwork bridge box with a time step of 2.943μsecs. The DFIG system

is connected to the grid through a 25MVA, 138kV/13.2kV, delta-wye transformer through a 7.2km line represented by a PI section model The DC capacitance that connects the RSC and GSC is given as 110mF. The parameters of the DFIG system are obtained from [31] and given in Table 3-8.

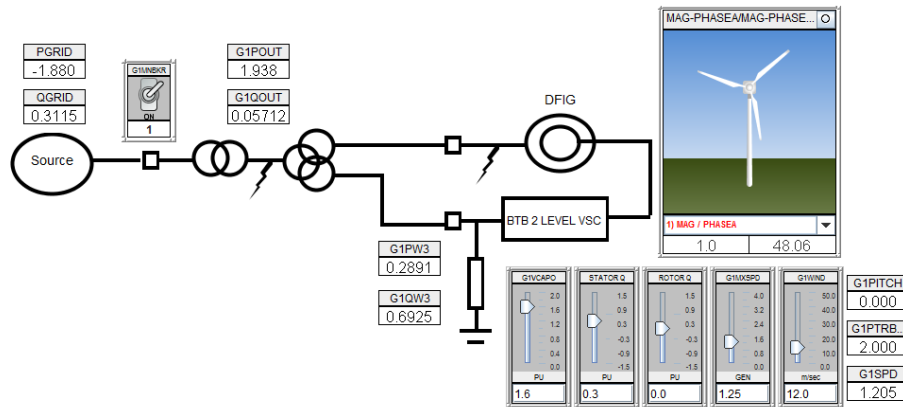


Figure 3-53 DFIG System in RSCAD [31]

Table 3-8 DFIG System Parameters [31]

Rated MVA <b>S<sub>dfig</sub></b>	2.2
Power MW <b>P<sub>dfig</sub></b>	2
Vrated_stator_prim vs_sec	0.69kV LL rms
Interface resistance <b>R<sub>a</sub>=R<sub>b</sub></b>	0.0015 ohms
Interface reactor <b>L<sub>a</sub>=L<sub>b</sub></b>	100μH
Power rating converter	0.3MW
Switching frequency DFIG	2000Hz
Turns ratio_rotor-stator	2.6377
Frequency <b>F<sub>grid</sub></b>	60 Hz
Stator leakage reactance <b>X<sub>s</sub></b>	0.102 pu
Stator resistance <b>R<sub>s</sub></b>	0.00462 pu
Rotor leakage reactance <b>X<sub>r</sub></b>	0.08596pu
Rotor resistance <b>R<sub>r</sub></b>	0.0060 pu
Inertia constant <b>H<sub>dfig</sub></b>	1.5 MWs/MVA

The interface between the small time step subnetwork and the grid simulated in the large time step is done using an interface transformer model in RSCAD. The interface transformer is modeled as a travelling line with a travel time given by [31]:

$$\tau_{trf\_inter} = 1.39\Delta T_{large} = \sqrt{L_{trf\_inter}C_{trf\_inter}} \quad (3.58)$$

To alleviate the effect of including an artificial line, the inductance of the line  $L_{trf\_inter}$  should be chosen to minimize the size of the shunt capacitance  $C_{trf\_inter}$  [31].  $L_{trf\_inter}$  can be taken as a fraction of the leakage inductance of the transformers in the DFIG system. A 0.22MVar high pass capacitive filter with cut off frequency of 2000Hz is connected to the grid side converters AC terminals to reduce harmonic current injections to the grid [31]. Figure 3-54 shows the response of the DFIG wind system pitch control to a ramp increase in wind speed from 5m/s to 15m/s. For wind speed <12m/s, the pitch angle is set to zero. For wind speeds > 12m/s, the pitch control is activated at a rate limit of 5deg/s and the DFIG output power is regulated to its rated power output as shown in Figure 3-55.

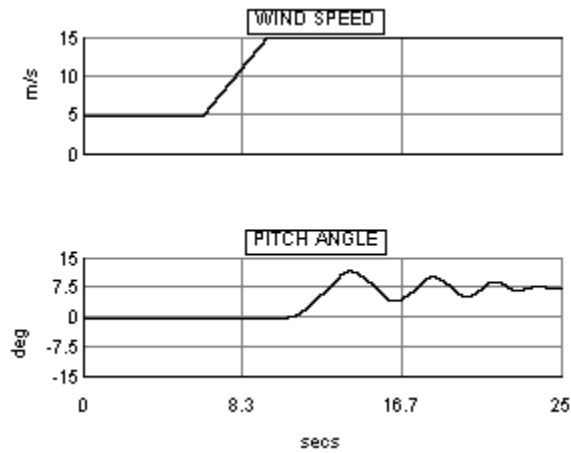


**Figure 3-54 Pitch angle response to wind speed ramp**

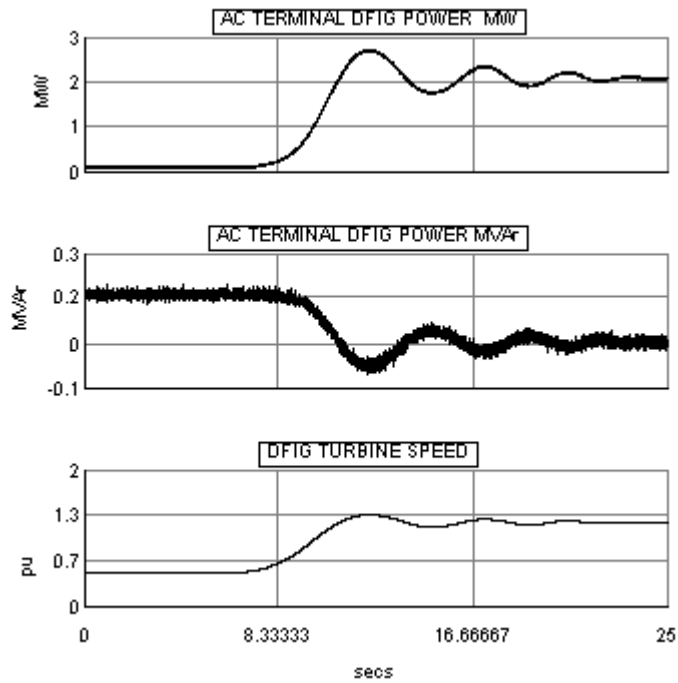


Figure 3-55 Power and speed response of DFIG wind system to ramp change in wind speed.

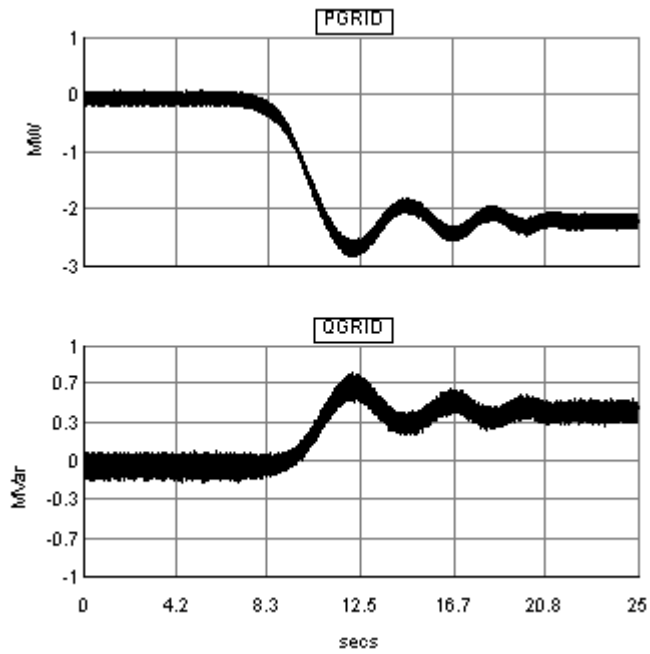


Figure 3-56 Grid power response to ramp change in wind speed

## 3.5 Conclusions

This chapter discussed the modeling of a diesel generating system; a photovoltaic system and a DFIG wind energy system as well as their associated control systems. The objective of this chapter was to gain an introductory knowledge of the theory of each DERs and their control systems. The modeling of voltage source converters using the small time step sub-network which is required to represent the high switching frequency dynamics of VSCs was discussed. These small time step subnetworks require dedicated processors to keep the simulation time steps less than  $3\mu\text{secs}$  which increasing the computational burden and required hardware resources on the RTDS. The use of average-value models (AVM) to reduce the required hardware resources is discussed in Chapter 4. A comparison of the steady state and transient operation of the AVM and full VSC model is discussed in Chapter 4 to understand the limitations of AVMs for transient simulations. The individual simulation cases of the diesel system, photovoltaic system and DFIG wind energy system helps to study their steady state and transient behaviour before they are connected to a larger network with other DERs. The DERs discussed in this chapter are used in the microgrid system discussed in Chapter 5.

# Chapter 4

## Average Value Modeling of Voltage

## Source Converters

### 4.1 Introduction

This chapter describes the average-value modeling of the voltage source converters used in the solar and wind energy systems described in Chapter 3. The goal of this chapter is to compare the response of the fully switched VSCs models with the AVMs to show the limitations of using AVMs for converter modeling. A comparison of the hardware reduction using the AVMs is discussed in Chapter 5.

### 4.2 Average Value Models

Detailed modeling of the voltage source converters for the solar and wind energy systems described in Chapter 3 requires small simulation time steps in the range of 1.4 – 2.5 $\mu$ secs

to represent their high switching frequency dynamics. Typically in transient simulation programs, the ON and OFF state of a switch is represented by a small resistance (large conductance) and a large resistance (small conductance), respectively, as shown in Figure 4-1.

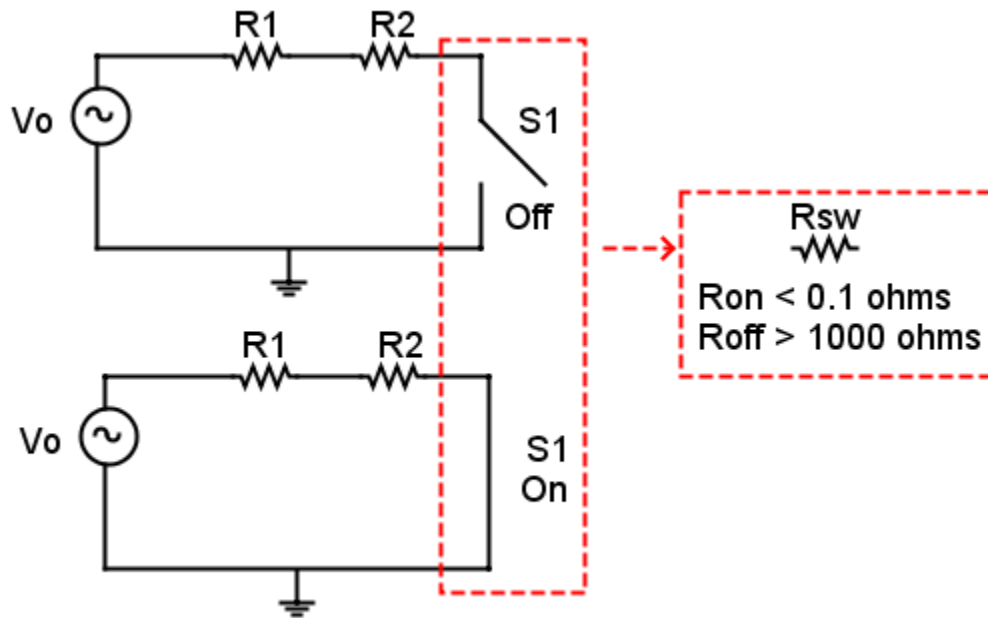


**Figure 4-1 Switching state representation**

To maintain real-time simulation using the EMTP algorithm described in Chapter 2, the system conductance matrix has to be reinverted each time the switching state of the network changes. For small simulation time steps in the range of 1-3  $\mu\text{s}$ , the reinversion of this matrix will require significant processing power. In order to achieve real-time simulation with small simulation time steps, an alternative approach is used in RTDS to model the high frequency switching in voltage source converters [31]. The RTDS simulator uses calculation short cuts, dedicated processors, and components to represent the fully switched models of the VSCs. Nevertheless, it requires a significantly high processing resources to simulate power system networks with voltage source converters [31].

To reduce the required hardware resources and computation burden, the fully switched VSCs can be represented using average-value models (AVMs). The two available AVM methods for representing voltage source converters using controlled voltage and current sources are (i) average modelling in the dq reference frame and (ii) the average models based on the use of switching functions [70]. The AVM approach in the dq reference frame is discussed and implemented in this research.

### 4.3 AVM in the *dq* reference Frame

The averaging operator over one switching cycle  $T_s$  is defined by equation 4.1 where  $\bar{x}(t)$  represents the averaged voltage (or current) waveform of the VSC as described by [55]:

$$\bar{x}(t) = \frac{1}{T_s} \int_0^{T_s} x(\tau) d\tau \quad (4.1)$$

Applying equation 4.1 to the AC side voltages of a VSC gives [55]:

$$\bar{v}_{a,b,c}(t) = \bar{m}_{a,b,c}(t) \frac{V_{DC}}{2} \quad (4.2)$$

where  $\bar{m}_{a,b,c}(t)$  are the averaged values of modulation indices of the three phase sinusoidal waveforms used for generating the PWM signals in the converter control scheme. In the dq reference frame, equation 4.2 becomes [55]:

$$\bar{v}_d(t) = \bar{m}_d(t) \frac{V_{DC}}{2} \quad (4.3)$$

$$\bar{v}_q(t) = \bar{m}_q(t) \frac{V_{DC}}{2} \quad (4.4)$$

The DC side current is obtained using the power balance (assuming negligible converter losses) between the DC and AC side of the VSC, which is given by [55]:

$$P_{DC}(t) = P_{AC}(t) \tag{4.5}$$

$$V_{DC}(t)I_{DC}(t) = v_a(t)i_a(t) + v_b(t)i_b(t) + v_c(t)i_c(t) \tag{4.6}$$

$$I_{DC}(t) = \frac{v_a(t)i_a(t) + v_b(t)i_b(t) + v_c(t)i_c(t)}{V_{DC}(t)} \tag{4.7}$$

In the dq reference frame [55]:

$$I_{DC}(t) = \frac{\frac{3}{2}(v_d(t)i_d(t) + v_q(t)i_q(t))}{V_{DC}(t)} \tag{4.8}$$

Figures 4-2 and 4-3 shows the dq reference frame AVM representation of the VSCs for the PV (solar) and DFIG wind converter systems.

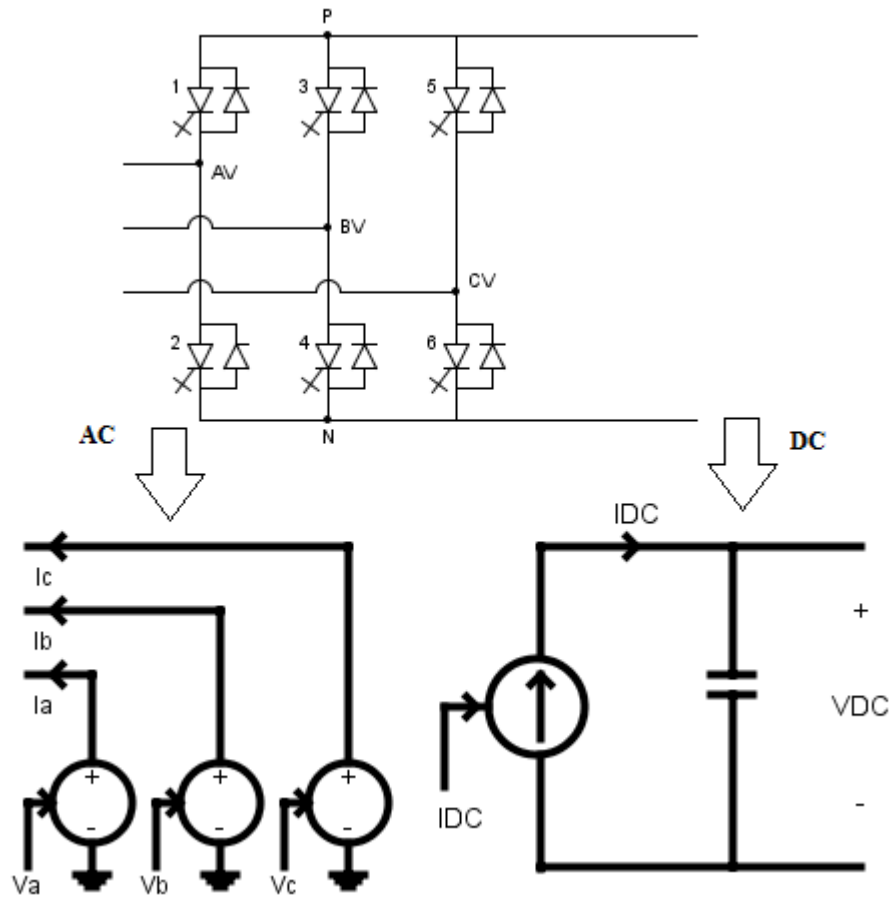


Figure 4-2 AVM for PV VSC

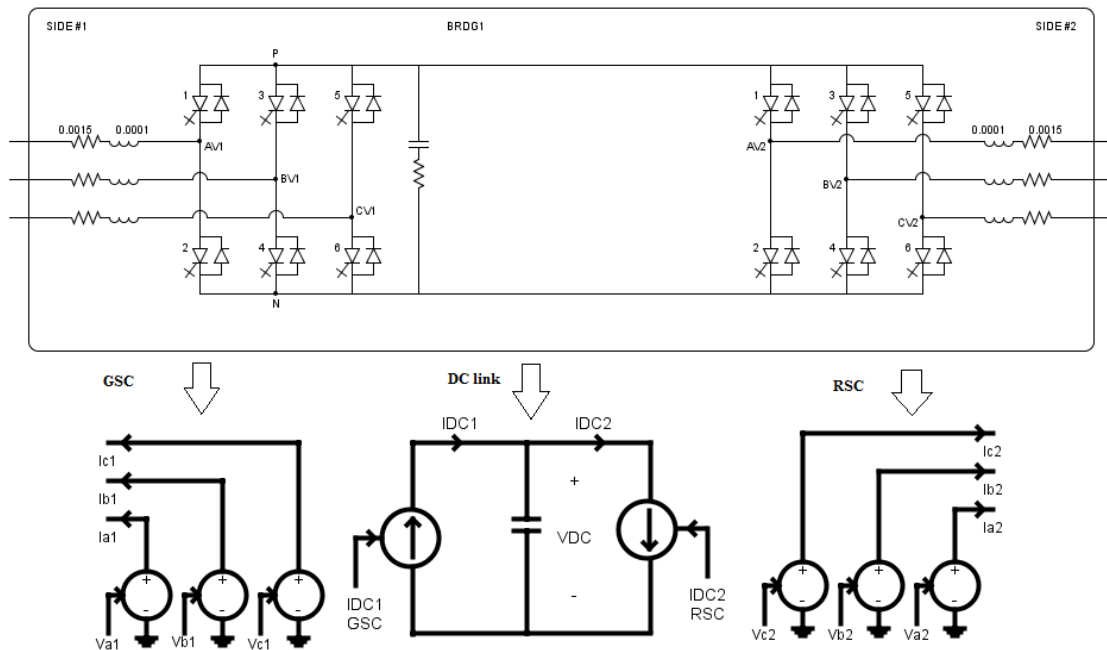


Figure 4-3 AVM for DFIG VSC

The voltage sources are controlled using the output of the dq-ABC transformation which are the reference modulation waveforms for the SPWM control discussed in chapter 3. The AVM based on the dq reference frame AVM does not represent the switching harmonics and cannot be used for VSC harmonic analysis [70]. The converter power losses can be included in the AVM by using a lumped resistance in the controlled voltage sources. For the DFIG AVM, the resistance can be added to the stator or rotor winding resistance [55].

## 4.4 Comparing AVM and Detailed VSC

This section shows the comparison between the AVM and detailed VSCs in terms of the dynamic response of the Solar and DFIG system. The comparison in terms of hardware resources will be discussed in Chapter 5.

4.4.1 Comparing the AVM and Full VSC for the DFIG system

Figure 4-4 shows the RSCAD Draft case used to compare the response of the AVM and detailed VSC model for the DFIG. The DFIG is rated at 2MW, 0.69kV LL rms at the stator terminals and is connected to the 25MVA, 138kV/13.2kV transformer through a 7.2 km line represented by a PI section model. The impedance of the grid is  $3/86^0\Omega$ .

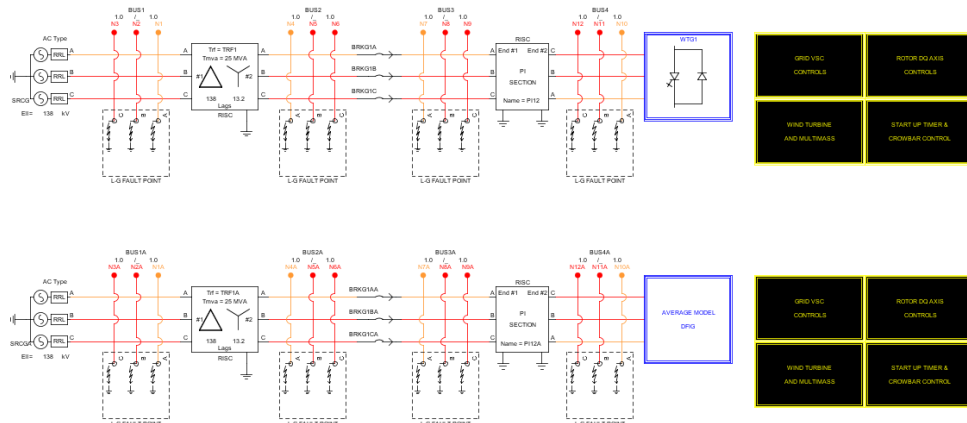


Figure 4-4 Comparing the AVM and Fully Switched DFIG VSC

The control scheme and parameters are kept the same for both the AVM and detailed VSC. The controlled voltage source AVM representation of the GSC and RSC is shown in Figure 4-5 where the injected voltages are the reference voltage waveforms obtained from the GSC and RSC current control schemes described in Section 3.4.2.

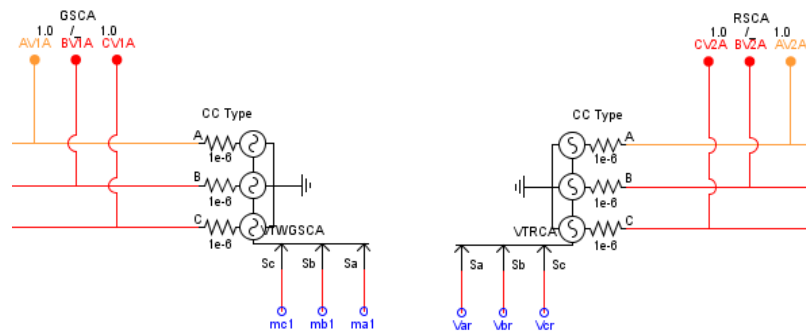


Figure 4-5 GSC and RSC AVM voltage source representation in RSCAD/Draft

The DC bus link for the DFIG AVM is shown in Figure 4-6 [71]. The value of the DC bus capacitance is 110 mF. The current sources represent the DC currents obtained from the AC and DC power balance of the GSC and RSC circuits. A charge controller represented by the voltage source and breaker BRKCH is used to set the DC bus voltage to its initial value to charge the DC side capacitance at simulation start up and is switched off (i.e BRKCH is opened) when the DC side voltage is regulated to the reference point by the controls [71].

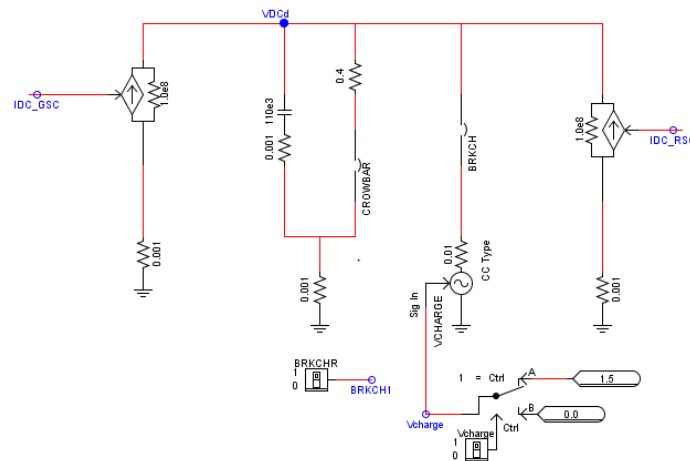


Figure 4-6 DC Bus link for the AVM

Figures 4-7 – 4.12 compares the transient response of the DFIG real and reactive power, speed, DC bus voltage, dq voltage and current response of the AVM and Full VSC DFIG system to a 0.1 ohm, 5 cycle, three phase line to ground fault at the DFIG-Grid bus connection terminal. Figures 4-7 – 4-12 show a close response between the Full and AVM of the VSC before and after the fault event. The deviations in the transient response of the AVM from the Full VSC model is due to the simplifications used in the AVM which does not represent the high switching frequency dynamics of the VSC as shown in Figure 4-13.

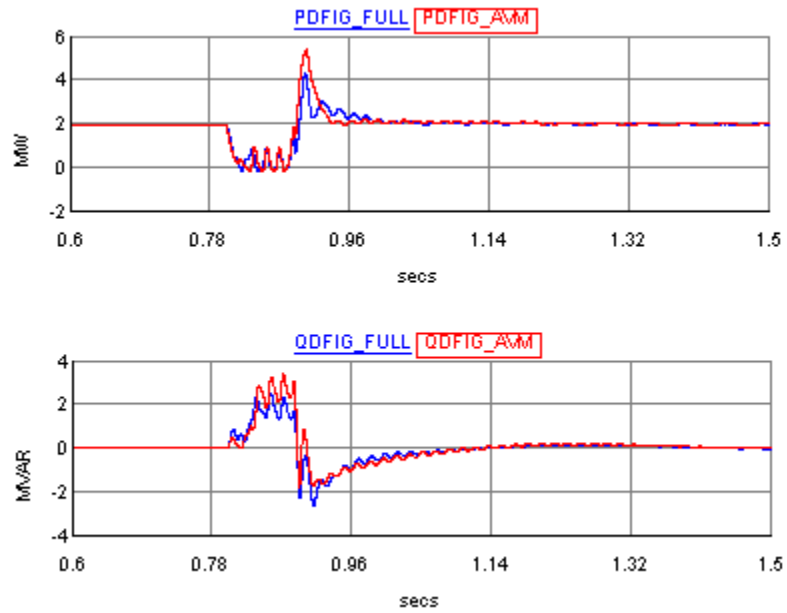


Figure 4-7 DFIG Real and Reactive Power

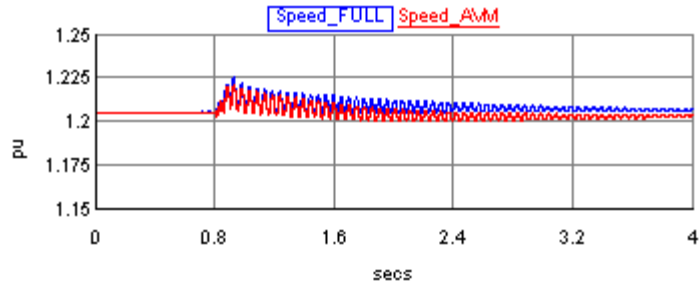


Figure 4-8 DFIG Speed

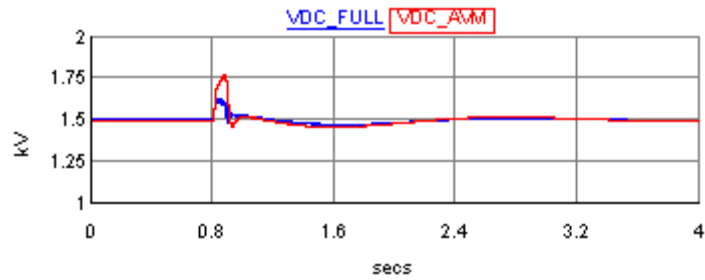


Figure 4-9 DC Bus Voltage

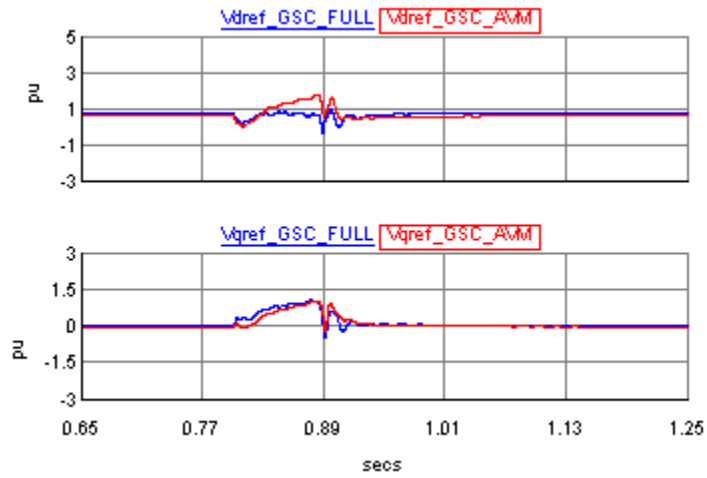


Figure 4-10 Grid side converter dq voltage references

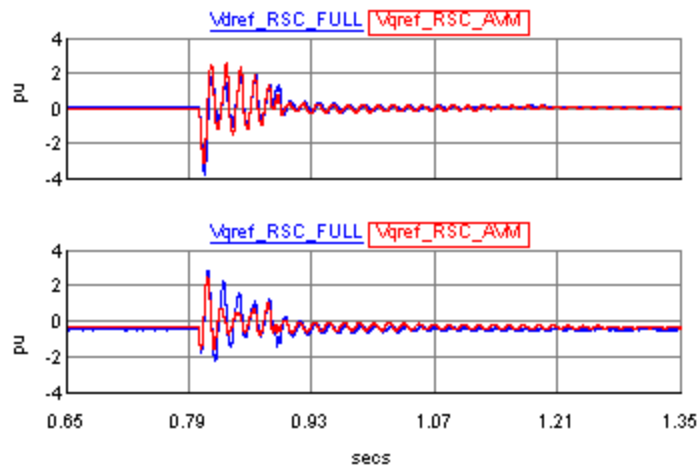


Figure 4-11 Rotor side converter dq voltage references

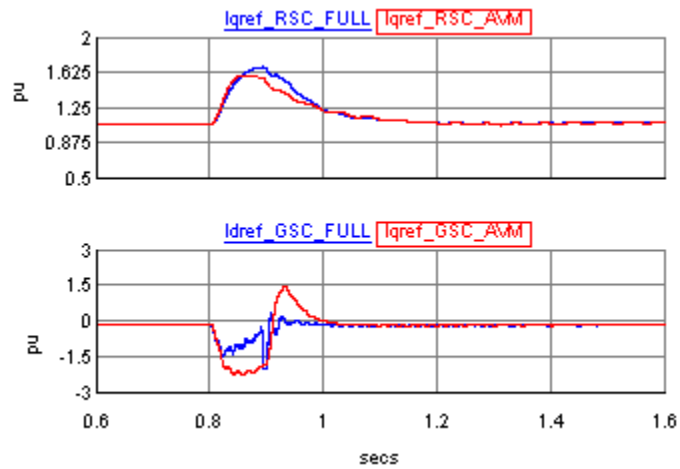


Figure 4-12 q current reference for RSC and d current reference for GSC

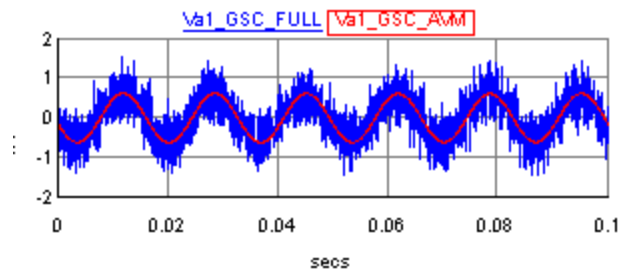


Figure 4-13 Switching frequency dynamics in DFIG Full VSC.

#### 4.4.2 Comparing the AVM and Full VSC for the PV system

Figure 4-14 shows the RSCAD Draft case used to compare the response of the AVM and detailed VSC model for the PV system. The ratings of the solar system are given in Section 3.3.4. The control scheme and parameters are kept the same for both the AVM and detailed VSC PV system. The response of the real and reactive power of the PV system and grid, the VSC dc bus voltage, modulation waveforms response of the AVM and Full VSC to a 0.1ohm, 5 cycle, and three phase line to ground is shown in Figures 4-15 to 4-17. The difference in the Solar AVM transient response compared to the fully switched PV VSC model transient response shown in Figures 4-15 to 4-17 is associated with the approximations made in the modeling of the converter side dynamics for the AVM which does not include the switching harmonics in the Full VSC model.

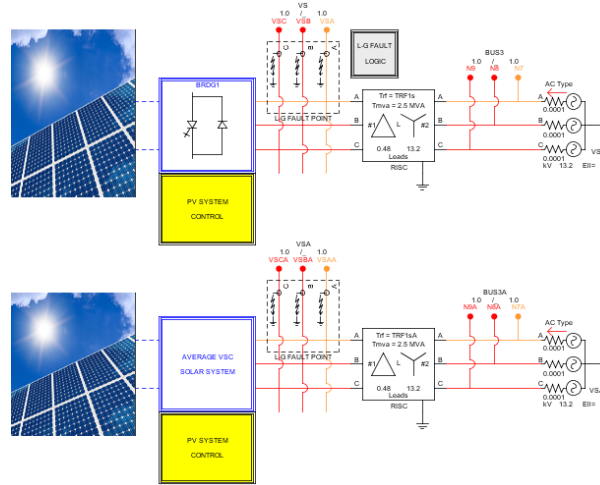


Figure 4-14 Simulation case for comparing the FULL and AVM VSC for the PV system

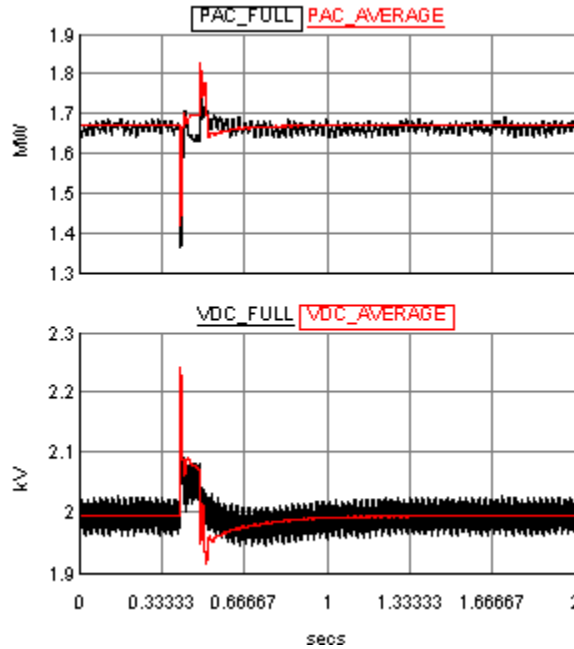


Figure 4-15 Real power output and DC bus voltage of FULL and AVM model to three phase line to ground fault

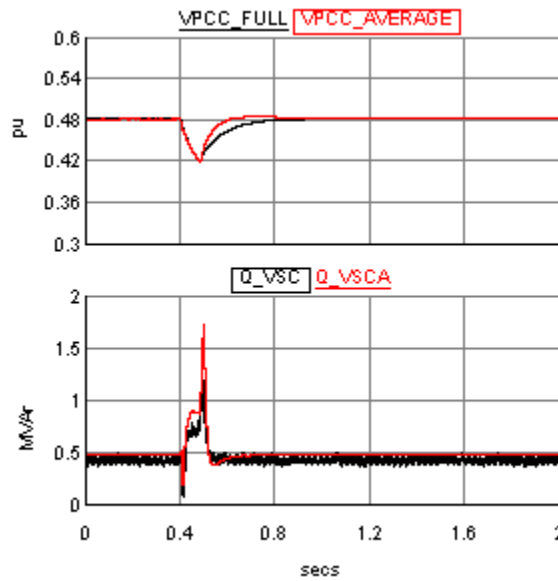


Figure 4-16 Per unit voltage at PV-grid point of connection and reactive power of FULL (black) and AVM(red) model to three phase line to ground fault.

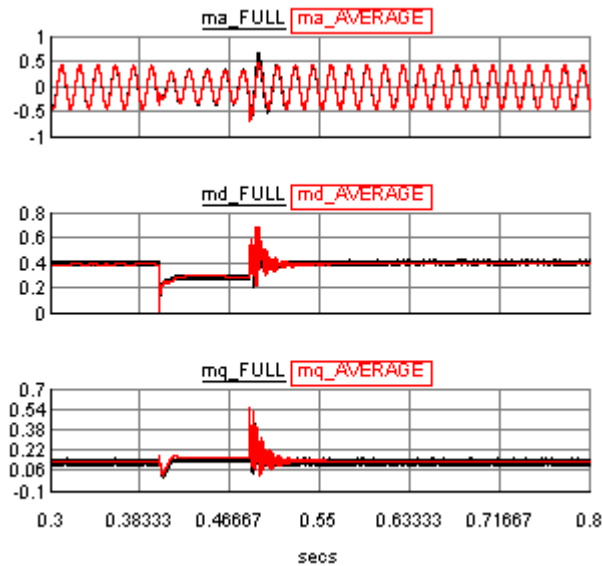
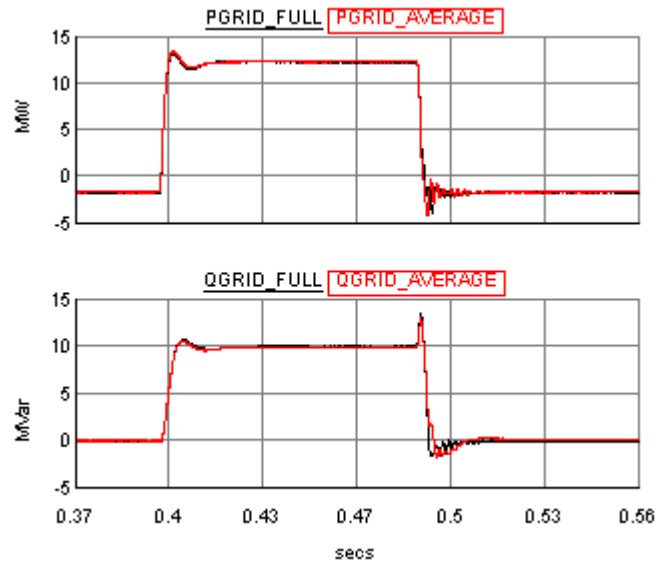


Figure 4-17 dq modulation indices response to three phase line to ground fault with FULL (black) and AVM (red) VSC models



**Figure 4-18 Real and Reactive power at grid side response to three phase line to ground fault with FULL (black) and AVM (red) VSC models**

## 4.5 Conclusions

The AVM of the solar and DFIG was developed and their response compared. The results show differences in the transient operation between the FULL and AVM model and this can be attributed to the difference in modeling the switched VSC models in the small time step and comparing the simulation with no VSCs in the large time. From the grid perspective, the active and reactive power delivered by the AVM for both wind and solar match closely with the FULL VSC models as shown in Figure 4-7 and Figure 4-18. The response of the AVM and FULL VSC is sufficient when AC side dynamics are considered and this will be compared in the microgrid system in Chapter 5. The reduction in hardware requirements when the AVM VSC models are used in the microgrid is discussed in Chapter 5.

# Chapter 5

## Microgrid System Analysis

### 5.1 Introduction

This chapter describes the microgrid structure. An analysis of the operation of the microgrid and DERs in grid-connected and islanded mode is also presented. A hardware-in-the-loop simulation with the microgrid system with a protective relay is implemented and discussed.

### 5.2 Microgrid Structure

The microgrid structure is shown in Figure 5-1. The 13.2 kV microgrid is connected to the 138 kV utility grid through a 138 kV/13.2 kV transformer. The point of common connection (PCC) is on the LV side of the transformer, and the microgrid is interconnected using a static switch (S1). The microgrid is a radial network if the disconnect switches S2 and S3 are open, and can be transformed to a mesh network if S2 and S3 are closed [1]. In this

research, the microgrid is analyzed with S2 and S3 open. The interconnection transformer is a  $\Delta$ -Y grounded connection rated at 25MVA with 8% impedance. The 5.5 MVA diesel generator described in Section 3.2 is interconnected to the microgrid at bus-B7, and it performs the frequency control of the microgrid during the islanded operation. The 1.74MW PV system described in Section 3.3 is connected to the microgrid at bus-B3, and the 2MW DFIG wind turbine generator described in Section 3.4 is connected to bus-B5. To facilitate microgrid voltage synchronization three switched capacitors banks rated at 0.5MVA each are connected at BUS1.

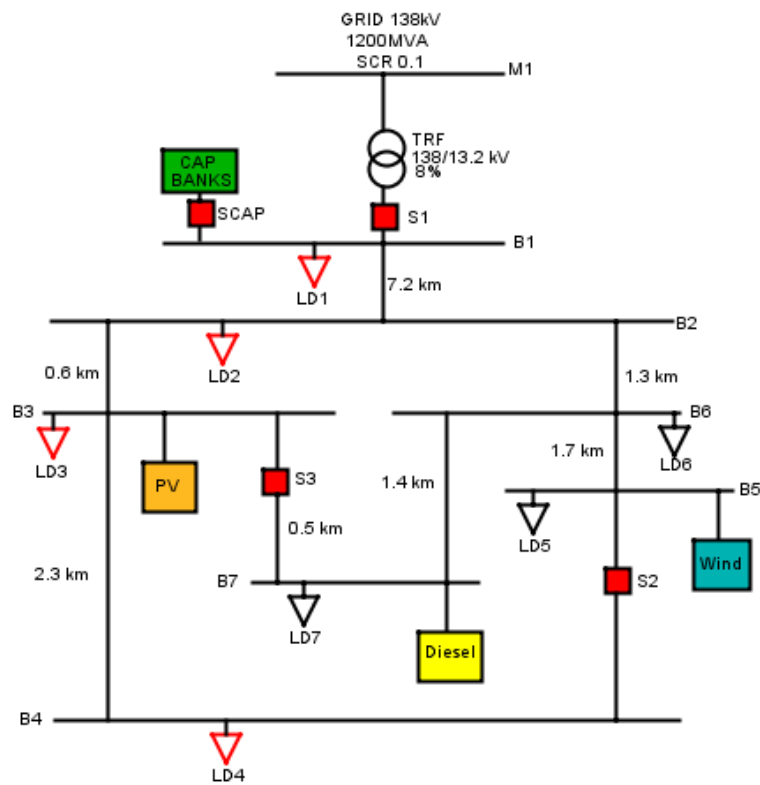


**Figure 5-1 Microgrid structure**

The distribution lines in the microgrid are less than 8 km and are represented using pi-section models in the simulation model. Due to node limitations (72 single phase nodes) imposed by the hardware limits on the RTDS, the CIGRE benchmark network was reduced from an 11 bus system to a 7 bus system while maintaining the original structure. This was

done as the short transmission line lengths in the microgrid network are not long enough for the network to be divided into subsystems for multi-rack simulations. Multi-rack simulations require transmission line lengths which have a travel time greater than the simulation time step. For a 50µsecs simulation time step, the minimum length of line required for multi-rack simulations is 15km. Table 5-1 gives the transmission line data is given in terms of the positive and zero sequence resistance, reactance and susceptance with the length of the corresponding line section indicated in Figure 5-1.

**Table 5-1 Transmission line data**

$R_p$	$X_p$	$B_p$	$R_0$	$X_0$	$B_0$
[Ω/km]	[Ω/km]	[1/μΩ·km]	[Ω/km]	[Ω/km]	[1/μΩ·km]
0.173	0.4317	3.8305	0.3506	1.7987	1.57

The self-resistance, reactance and susceptance of the line are obtained from Table 5-2 using the following expressions:

$$R_s(\Omega/\text{km}) = \frac{R_0 + 2R_p}{3} \quad (5.1)$$

$$X_s(\Omega/\text{km}) = \frac{X_0 + 2X_p}{3} \quad (5.2)$$

$$B_s(1/\mu\Omega \cdot \text{km}) = \frac{B_0 + 2B_p}{3} \quad (5.3)$$

### 5.2.1 Load shedding scheme

An automatic under-frequency load shedding scheme described in [6] was implemented to maintain the stability of the microgrid during power imbalances and frequency fluctuations caused by islanding or fault events. The loads are shed in stages to restore the frequency and consequently the stability of the microgrid network. The load shedding control is activated when the frequency and rate of change of frequency fall within the specified limits

and time duration [6]. The load shedding stages, amount of load to be shed, the frequency and rate of change of frequency limits and time duration settings are shown in Table 5-3.

**Table 5-2 Load shedding criteria**

Stage	Criteria	Time	Load shed	
1	$f \leq 59.5\text{Hz}$ or $\frac{df}{dt} > 1.5 \frac{\text{Hz}}{\text{s}}$	0.1 secs	LD1	1.37MW 0.66MVAr
2	$f \leq 58.7\text{Hz}$ or $\frac{df}{dt} > 1.5 \frac{\text{Hz}}{\text{s}}$	0.08 secs	LD2	1.045MW 0.343MVAr
3	$f \leq 58.3\text{Hz}$	0.08 secs	LD3	0.930MW 0.45MVAr
4	$f \leq 58.0\text{Hz}$	0.08 secs	LD4	0.96MW 0.47MVAr

Table 5-2 gives the load data for bus 1-7 of the microgrid. Loads on bus 1-4 are modeled as switched RL passive loads which are allowed to shed if needed while loads on bus 5-7 are modeled as non-switchable dynamic loads representing the critical loads in the network.

**Table 5-3 Load Data**

Bus	Phase A [KVA]	Phase B [KVA]	Phase C [KVA]	pf
1	506	506	506	0.9
2	367	367	367	0.95
3	344	344	344	0.9
4	356	356	356	0.9
5	325	625	100	0.95
6	125	725	300	0.95
7	275	625	150	0.95

### 5.2.2 Implementation of microgrid in RTDS

The microgrid model shown in Figure 5-1 was implemented in a RTDS real-time simulator.

Figure 5-2 shows the microgrid with the DERs modeled in RSCAD. The microgrid is simulated with a time step of  $75\mu\text{s}$  on a one rack simulator with four processor cards.

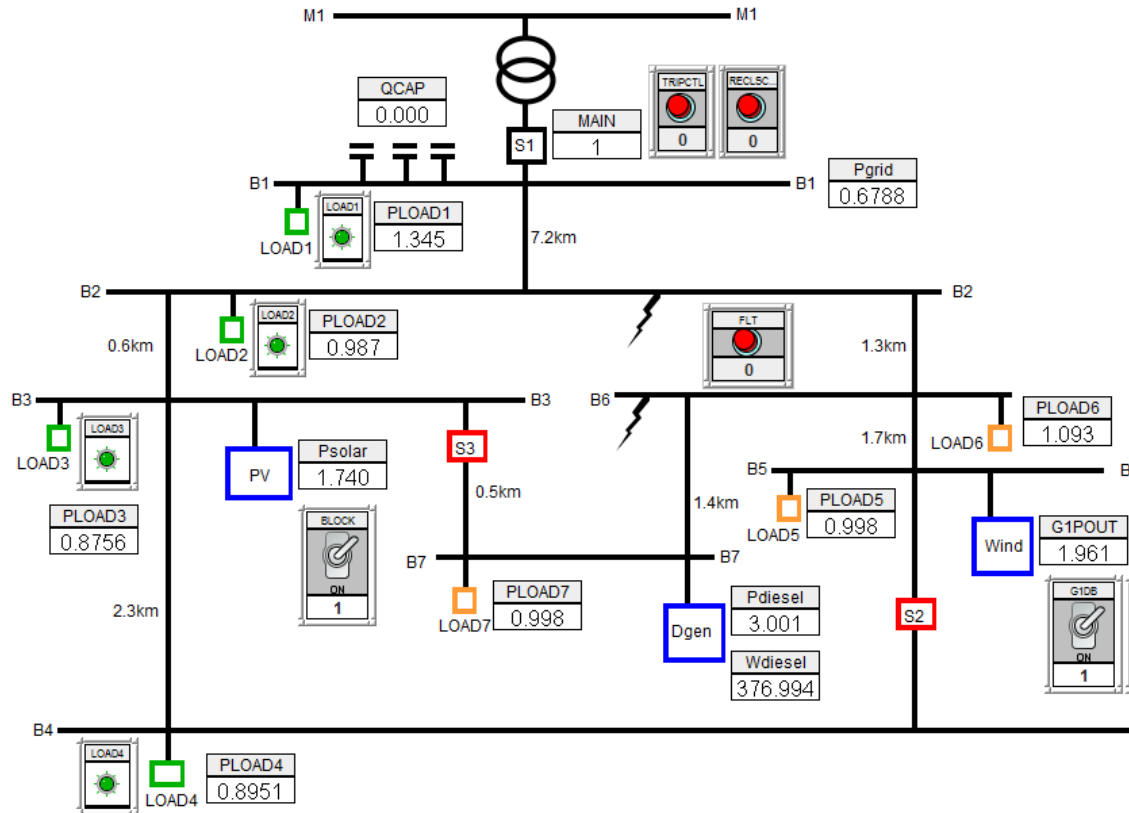


Figure 5-2 RSCAD Runtime model of microgrid with the DERs

Figure 5-3 shows the allocation of hardware resources for the microgrid using the fully switched VSC models. All four processor cards on the RTDS rack are required to obtain the solution of the microgrid network.

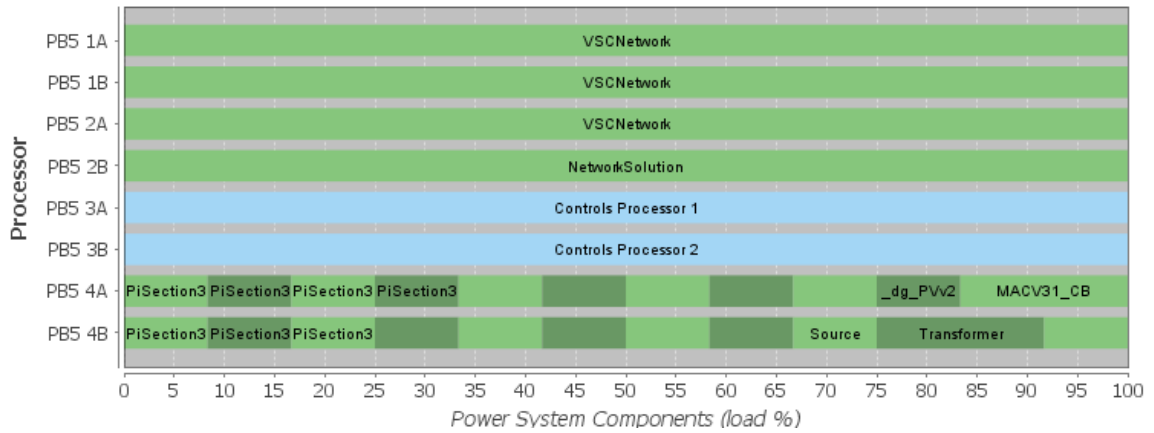


Figure 5-3 Processor assignment using fully switched VSC models

The allocation of hardware resources when the AVM models are used for the solar and DFIG energy system is shown in Figure 5-4. The number of required processor cards has been reduced to three when using the AVM. The AVM is useful when the available hardware resources on the RTDS rack is insufficient to model the given network with the fully switched VSC models.

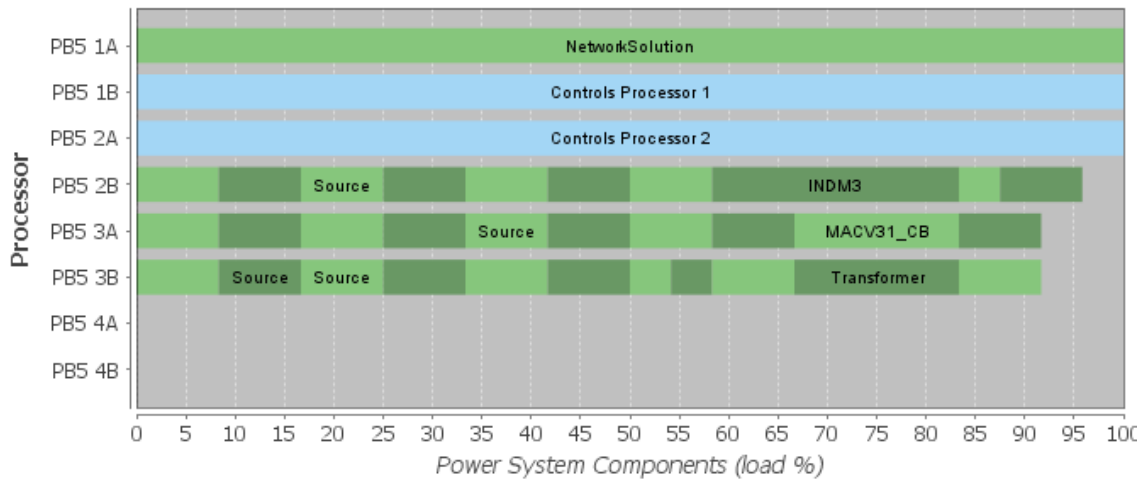


Figure 5-4 Processor assignment using the average-value VSC models

## 5.3 Grid connected operation of microgrid

In grid-connected mode, the main switch S1 is closed and the microgrid frequency is determined by the grid frequency. The DFIG wind and PV systems control their real and reactive power output using the control schemes described in Chapter 3 while the diesel generator operates in droop control to exchange real and reactive power with the grid. The diesel generator was set to produce 3MW and 1.736MVar at steady state and was initialized by taking the solar and wind generator system as constant PQ sources at unity power factor at rated power of 1.74MW and 2MW respectively. The generator controls described in chapter 3.2 were reinitialized to the new initial mechanical torque and excitation field voltage given as 0.55pu and 1.85pu. Table 5-4 show the steady state, per unit line to neutral phase voltages on each bus with NO DERs and with DERs using the Full and AVM VSC models discussed in chapter 4. Table 5-5 gives the average, per unit RMS bus voltages and percentage voltage unbalance defined by equation (2.3).

**Table 5-4 Per RMS Line phase voltages on bus 1-7 of the microgrid**

BUS	PER UNIT RMS PHASE VOLTAGES								
	NO DERS			DERS (FULL VSC)			DERS (AVM VSC)		
	PHASE A	PHASE B	PHASE C	PHASE A	PHASE B	PHASE C	PHASE A	PHASE B	PHASE C
M1	0.995	0.975	0.989	0.995	0.991	0.992	0.995	0.991	0.992
1	0.991	0.969	0.986	0.995	0.990	0.992	0.995	0.990	0.992
2	0.913	0.733	1.013	0.979	0.951	0.975	0.980	0.949	0.967
3	0.912	0.731	1.009	0.978	0.951	0.973	0.979	0.949	0.966
4	0.910	0.727	1.002	0.974	0.946	0.967	0.975	0.944	0.961
5	0.895	0.694	1.037	0.974	0.944	0.980	0.976	0.942	0.965
6	0.902	0.704	1.030	0.976	0.947	0.981	0.980	0.946	0.968
7	0.898	0.695	1.036	0.980	0.956	0.983	0.988	0.954	0.974

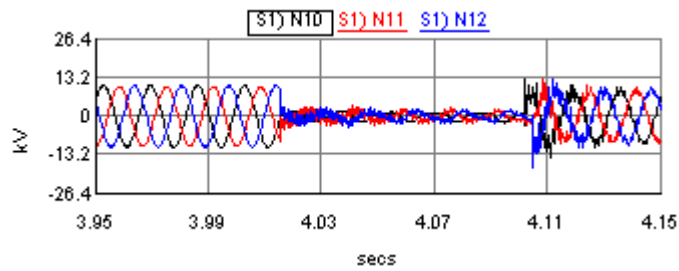
**Table 5-5 Average LL rms voltages and %Voltage unbalance**

BUS	AVERAGE pu LL RMS VOLTAGES AND % VOLTAGE UNBALANCE					
	NO DERS		DERS FULL		DERS AVM	
M1	0.9862	0.769%	0.9925	0.266%	0.9927	0.294%
1	0.9821	0.781%	0.9922	0.275%	0.9922	0.299%
2	0.8864	5.788%	0.9683	1.993%	0.9654	2.037%
3	0.8840	5.787%	0.9671	1.927%	0.9646	2.036%
4	0.8796	5.785%	0.9624	1.841%	0.9600	2.034%
5	0.8754	7.265%	0.9658	2.336%	0.9609	2.560%
6	0.8786	6.803%	0.9677	2.044%	0.9646	2.365%
7	0.8761	7.165%	0.9730	2.212%	0.9721	2.352%

From Table 5-5 it can be shown that with no DERs, the voltage unbalance exceeds 4% on bus 2-7. The connection of the DERs reduces the voltage unbalance to less than 3% thus improving the voltage profile of the grid-connected microgrid network. The error difference between voltage unbalance and per unit bus voltages between the AVM and FULL VSC models shown in Tables 5-4 and 5-5 are less than 0.6% and 0.002 pu respectively, thus the steady state bus voltages and voltage unbalance values using the AVM and full VSC models give very close results.

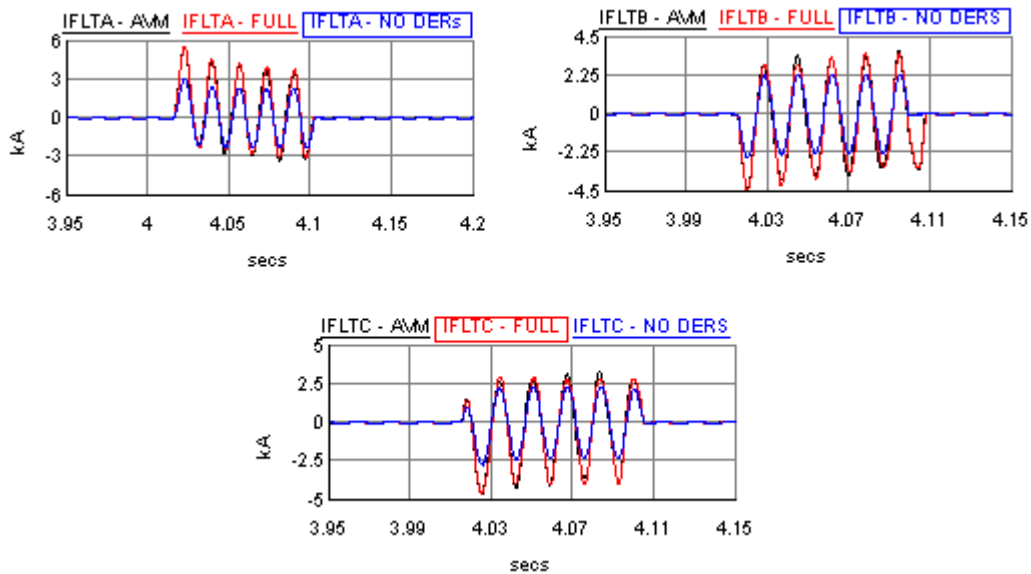
### 5.3.1 Microgrid transient response in grid-connected mode

An analysis of the impact of DER integration on fault current levels in the network is discussed in this section. DER integration may result in fault currents in excess of the capability of circuit breakers and associated protection and control equipment. Changing fault levels can also affect the correct operation of traditional fault detection schemes. Figure 5-5 shows a 5 cycle, 0.1 $\Omega$ , three phase line to ground fault applied at Bus 6.



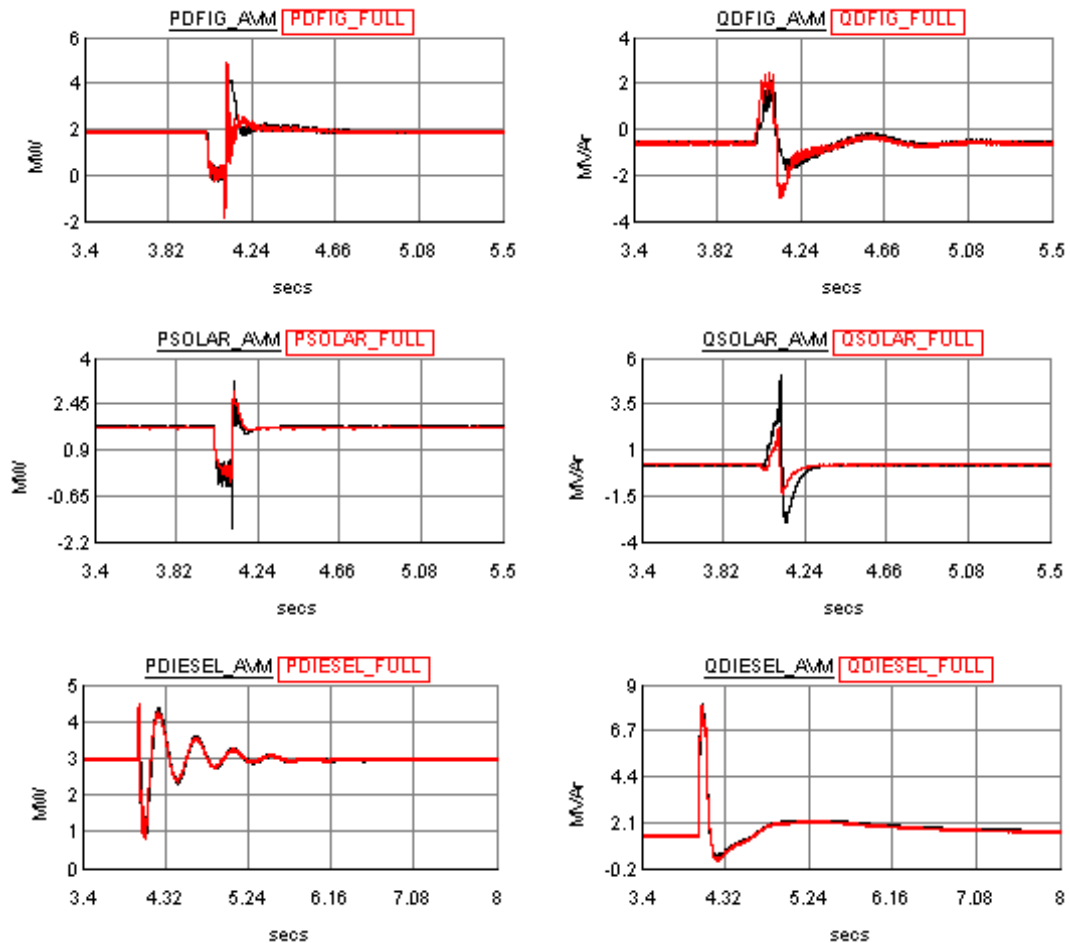
**Figure 5-5 Line to Line Voltages response to 3 Phase line to ground fault at BUS6**

Figure 5-6 compares the phase fault currents at Bus 6 with a 5 cycle, 0.1Ω line to ground fault with no DERs (Blue), DERs with full VSC model (Black) and DERs with AVM models (Red) in the microgrid. The fault current response of the microgrid with the Full and AVM VSC of the Solar and DFIG system give similar results. It is shown that with the DERs integrated in the network the fault currents in each phase of Bus 6 is increased by ~25%.



**Figure 5-6 Fault currents at Bus 6 with a 5 cycle, 0.1 ohm line to ground fault with no DERs (Blue), DERs with full VSC model (Black) and DERs with AVM models (Red) in the microgrid**

The real and reactive power supplied by the DFIG Wind, Solar and Diesel DERs is shown in Figure 5-7. The results obtained with the AVM and FULL VSC converter models are very similar.



**Figure 5-7 Real and reactive power supplied by the individual DERs and consumed for the AVM (black) and FULL (red) VSC converter models during**

Figure 5-8 compares the microgrid frequency in grid-connected mode before and after the fault using the AVM and FULL VSC converter models. The Full and AVM model show similar response. The AVM model has a slightly different variation during the transient period immediately after the fault. For both models the frequency is regulated to 60Hz by the main grid source.

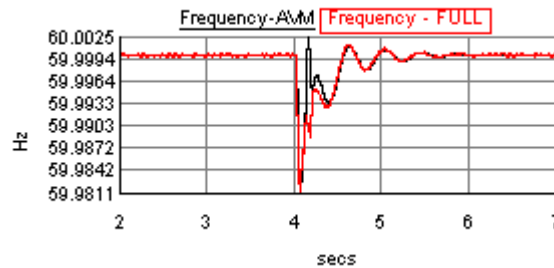


**Figure 5-8** Microgrid frequency response to 3PH, line to ground fault at BUS 6 for the AVM(black) and FULL VSC (red) converter DERs.

## 5.4 Microgrid Operation in islanded mode

The operation of the microgrid is analyzed for the following scenarios namely: (i) change of grid-connected to islanded mode of operation and (ii) microgrid response in islanded operation during a temporary fault condition. Simulation results with the AVM and FULL VSC converter models are compared for all simulation cases.

### 5.4.1 Case A: Change from Grid-connected to Islanded operation

The microgrid is islanded by opening the point of connection circuit breaker switch S1 using a manual trip command. A breaker status signal is sent to the diesel generator to change the operating mode from droop power control mode to isochronous frequency control mode. Figure 5-9 shows the microgrid frequency before and after the islanded operation using the AVM and full VSC models for the DFIG and solar DERs. The frequency of the microgrid is regulated to 60Hz by the diesel generator operating in isochronous mode and the load shedding scheme is not activated, since the total microgrid load could be supplied by the DERs.

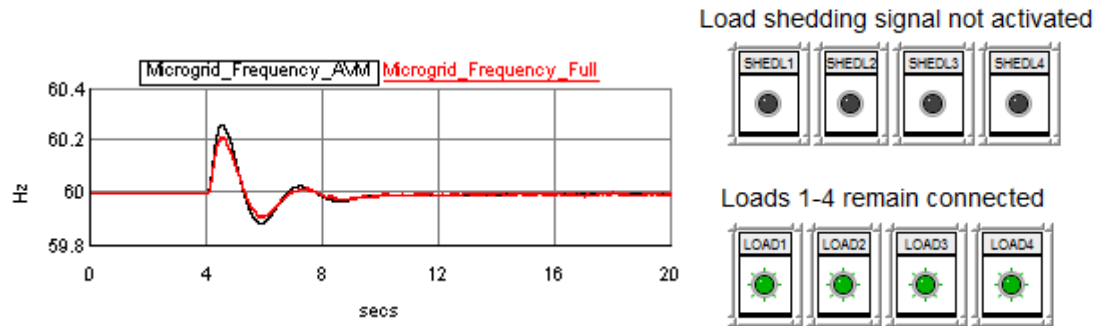


Figure 5-9 Microgrid Frequency before and after islanding with the AVM VSC (black) and FULL VSC Models(Red). Load shedding is not activated.

The total real and reactive power supplied by the GRID, DERs and consumed by the load before and after the islanding is shown in Figure 5-10. The steady state operation before islanding shows the GRID supplies 0.74MVA<sub>r</sub> at 2.64MVA<sub>r</sub>, the DERs supply 6.55MVA<sub>r</sub> at 1.33MVA<sub>r</sub> and the LOADS consume 7.2MVA<sub>r</sub> at 2.833MVA<sub>r</sub>. The results obtained with the AVM and FULL VSC converter models are very similar.

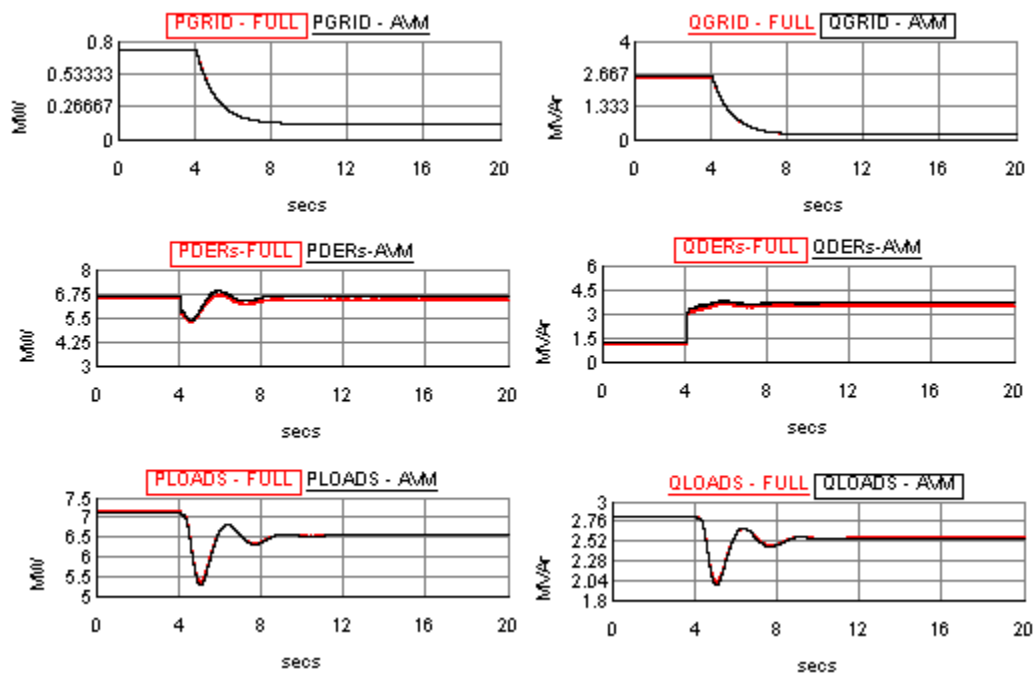
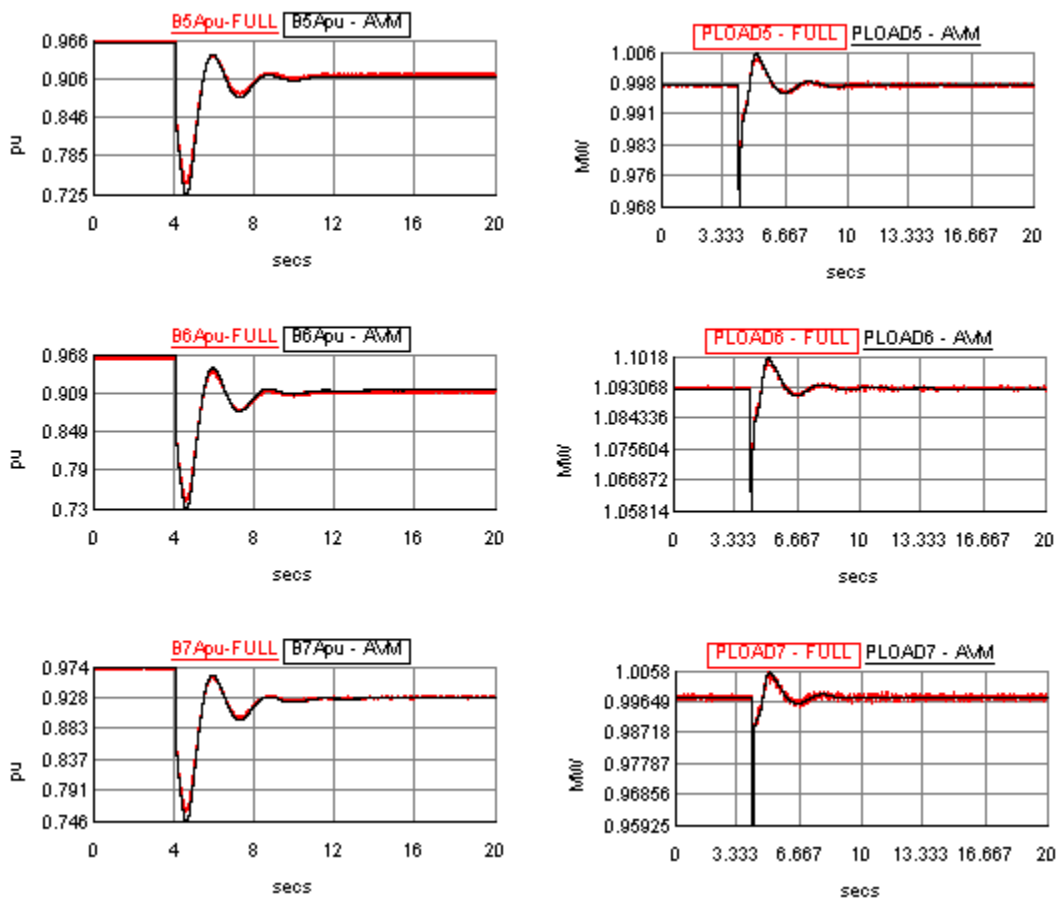


Figure 5-10 Total real and reactive power supplied by the GRID and DERs and consumed by the LOADS for both the AVM(black) and FULL (red) VSC converter models.

From Figure 5-10, the total power consumed by the load drops after islanding. This is due to the loss of reactive power from the grid which as shown in Figure 5-11 and 5-12 causes a 7% drop in the bus 1-7 voltages for the simulations with both AVM and FULL VSC models. The voltage drop changes the active power of the constant impedance loads on bus 1-4. The loads on bus 5-7 are represented as dynamic loads which despite the drop in the bus voltages keep their active power at the power set points given in Table 5-2. The Solar and DFIG DERs are operated in constant PQ mode and are not regulating the bus voltages (unity power factor operation). The reactive power lost from the grid disconnection is thus picked up by the diesel generator.



**Figure 5-11 Per Unit average RMS Bus Voltage and Load Response on Bus 5-7 for AVM (Black) and Full VSC Model (Red)**

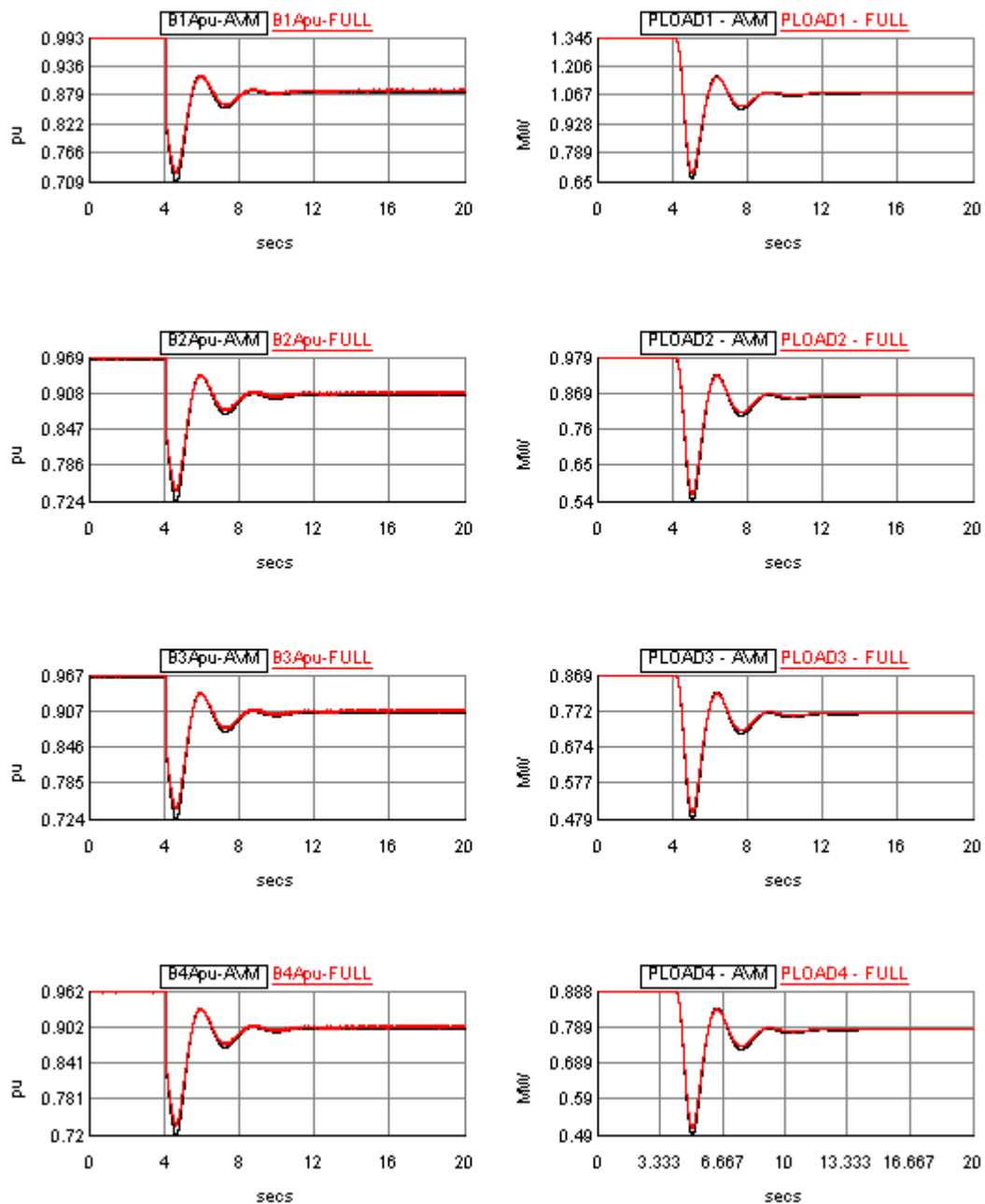


Figure 5-12 Per Unit average RMS Bus Voltage and Load Response on Bus 1-4 or AVM (Black) and Full VSC Model (Red)

Figure 5-13 shows an increase in the voltage unbalance on Bus 1-7 when the microgrid transitions from grid-connected to islanded operation. The microgrid with the AVM model of the DFIG and PV VSC shows a higher voltage unbalance compared to the FULL VSC

after islanding. The difference between the voltage unbalance after islanding obtained using the Full and AVM model on Bus 1-7 is less than 15%. This difference can be accounted for due to the use of transmission line interfaces to connect the VSC in the small time bridge box with the rest of the network simulated in the large time step. The interface transmission adds artificial capacitances to the network which are not present in the AVM.

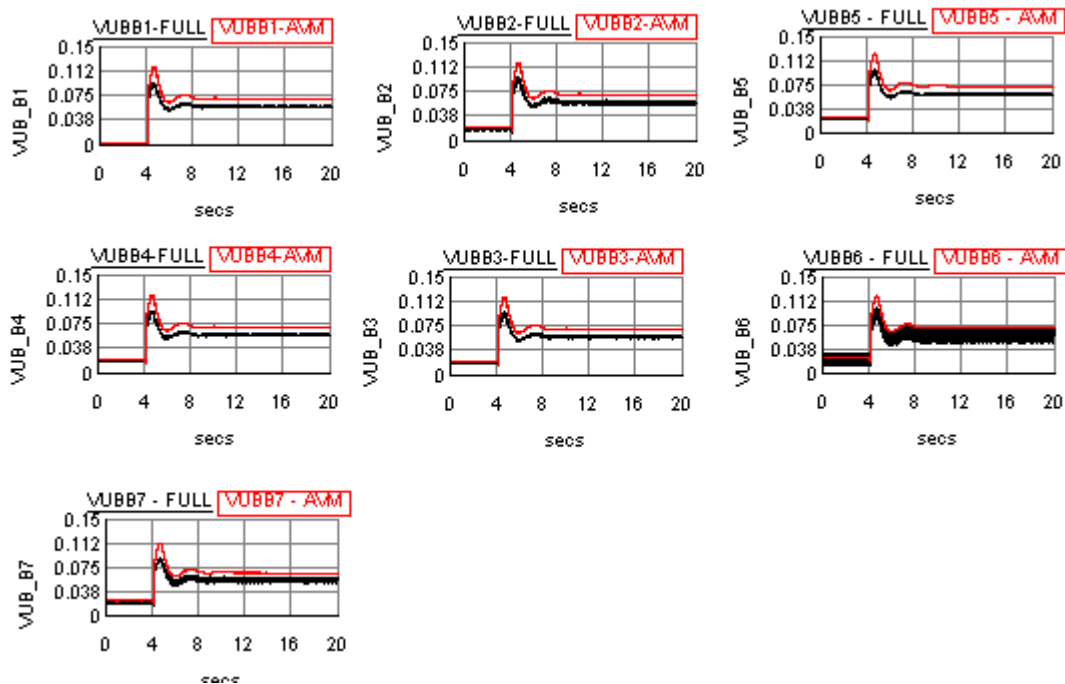


Figure 5-13 Voltage unbalance of the islanded microgrid using the FULL(black) and AVM(red) VSC Converter models for the Solar and DFIG DERs.

### 5.4.2 Case B: Temporary fault in islanded mode

A  $0.1\Omega$ ,  $0.1s$  single phase line to ground fault is applied to phase A of BUS6 of the islanded microgrid. The fault current obtained using the AVM and FULL VSC converter models give a close match as shown in shown in Figure 5-14.

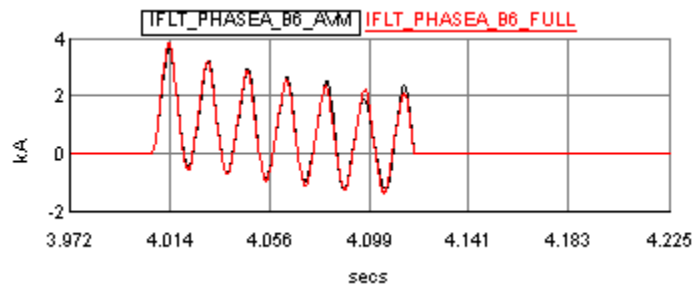


Figure 5-14 Fault current level for islanded microgrid with line to ground fault at BUS 6 using the AVM (black) and FULL(red) VSC model of the DFIG and SOLAR DERs.

Figure 5-15 shows the load shedding scheme is activated as the rate of change of frequency exceeds 1.5Hz/secs for both the simulations with the AVM and FULL VSC models. As a result, LOAD1 and LOAD2 and the diesel generator is able to restore the frequency of the islanded microgrid. Figure 5-16 shows the total power of the loads and DERs before and after the fault condition in the islanded microgrid using both the Full and AVM VSC models in the microgrid.

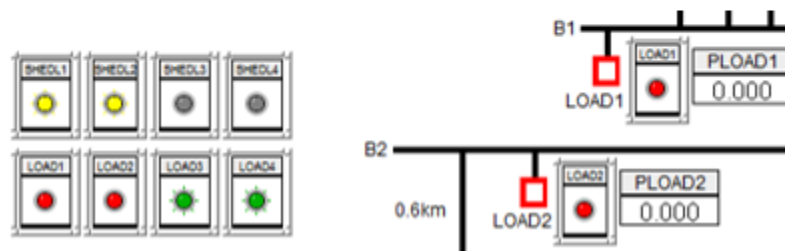
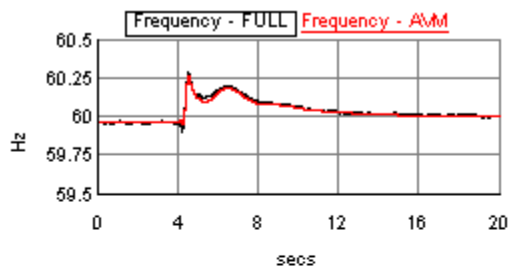
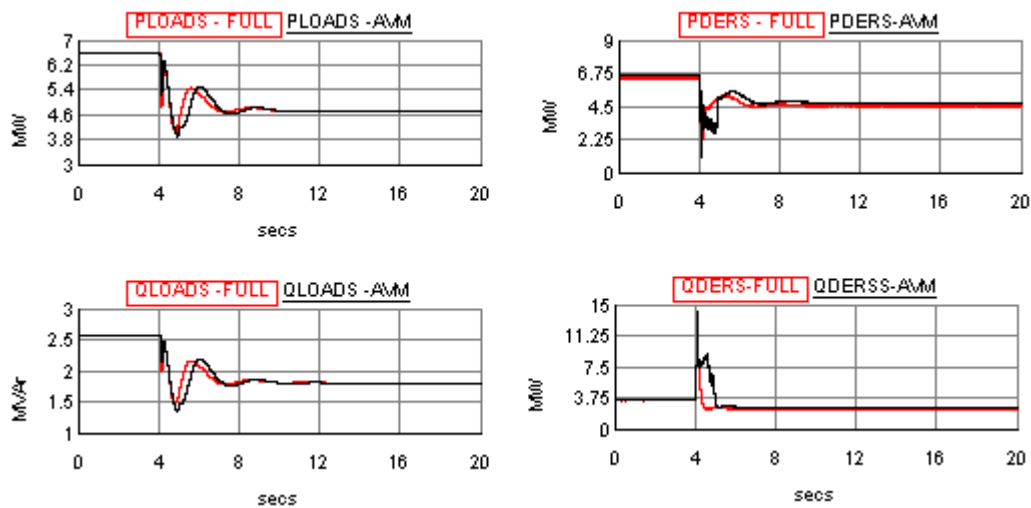


Figure 5-15 Microgrid Frequency during islanded fault condition activates load shedding



**Figure 5-16 Response of total real and reactive power supplied by the DERs and consumed by the LOADS for both the AVM(black) and FULL (red) VSC converter models during temporary fault in islanded microgrid.**

## 5.5 Microgrid Synchronization

As shown in Section 5.4, the microgrid supplies the local load when it is switched to islanded operation due to some network event such as a fault on the utility grid but the voltage unbalance exceeds 3% when the microgrid is islanded. In section 2.7, recommended limits for voltage unbalance are less than 3% to avoid heating in induction machine based DERs, in this case the DFIG system, and uncharacteristic harmonics in converter interfaced DERs. The microgrid has to be resynchronized (reconnected) to the utility grid to restore normal operation. For resynchronization, the voltage, phase angle and frequency of an islanded microgrid at the point of connection (BUS1) must be brought within the acceptable limits given in Table 2-1 before reconnection with the main grid. A passive synchronization method described in [6] is implemented using a synchro-check element available from the

RTDS protection library shown in Figure 5-17. The islanding and resynchronization signals are manually controlled by the TRIPCTL and RECLSCTL pushbuttons to demonstrate the synchronization of the microgrid back to the utility grid.

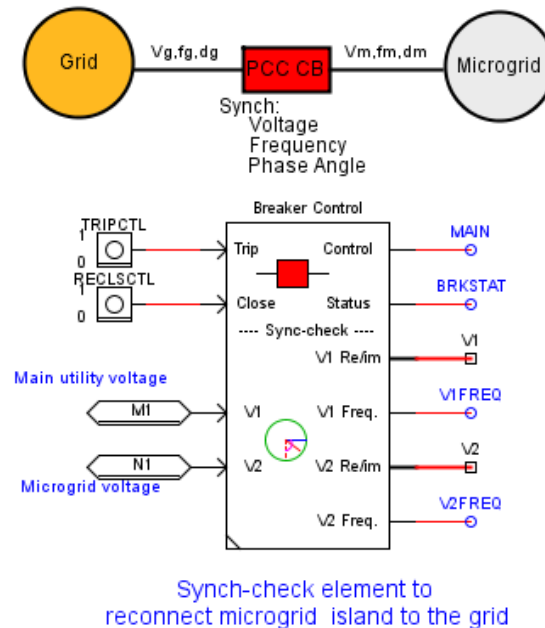


**Figure 5-17 RTDS Synchro-check element for microgrid synchronization**

The breaker control synchronization command is issued by the breaker control unit within the synchro-check element after the microgrid system is restored to steady state following the clearing of the fault. The synchro-check verifies that the phase voltages of the microgrid at the PCC breaker are within the set limits of magnitude, angle and frequency difference given in Table 2-1 before issuing a close command to the PCC circuit breaker to reconnect the microgrid to the grid [26]. The simulated scenario in this section includes disconnection from the grid (by manually tripping breaker S1) and then reconnecting the microgrid with the utility grid by the synchro-check element when the synchronized conditions are met. Figure 5-18 shows the voltage difference and angle difference of the microgrid using the AVM and FULL VSC models for the solar and DFIG system. The angle difference for

both models is less than 10 degrees and within the synchronization limits. A 6% angle difference is observed between the AVM and FULL VSC models. The voltage difference for both models give a close match and are greater than the limits of 3% for synchronization.

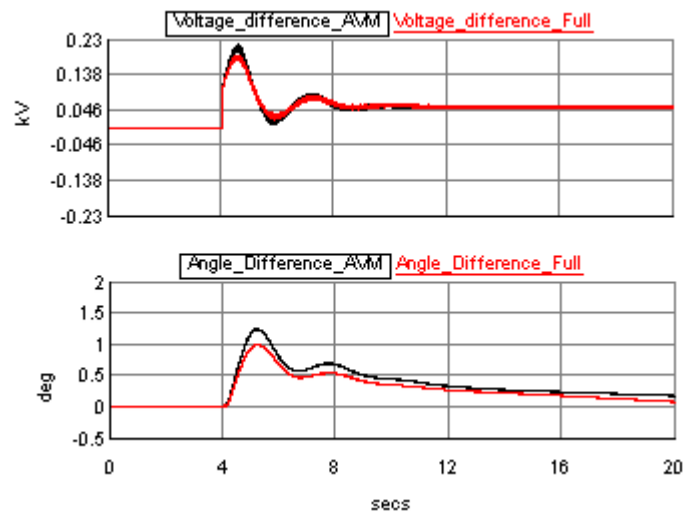


Figure 5-18 Voltage and phase difference between microgrid and grid at PCC after islanding using the FULL (red) and AVM(black) converter based DERs,

To meet the voltage synchronization criteria, the switched shunt capacitors connected to the PCC are manually turned on until the voltage difference meets the required criteria of 3%. It was observed that all three switched capacitors banks were required to meet the voltage criteria for synchronization. As shown in Figure 5-19, the switched capacitors reduce the phase voltage difference to less than 0.00657kV at the PCC.

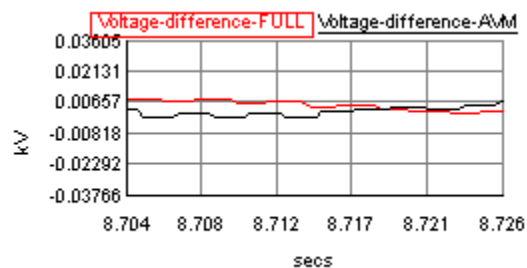


Figure 5-19 Voltage difference at Microgrid PCC after turning on the switched shunt capacitors

To facilitate synchronization, the speed reference of the diesel generator is increased to 1.00045 pu which makes the voltage phasor of the microgrid rotate with a frequency difference of about 0.2Hz as shown in Figure 5-20.

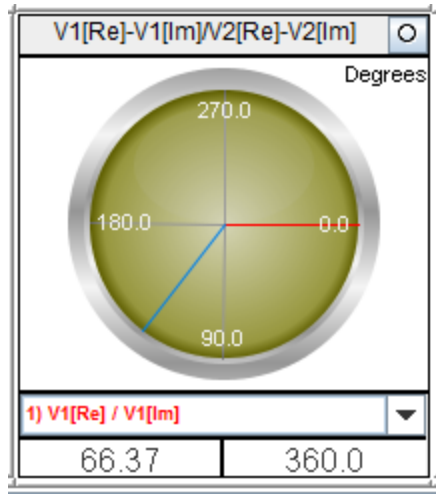


Figure 5-20 Phasor diagram representation of microgrid (blue) and grid (red) bus voltages

The microgrid is reconnected to the grid when the voltage phasor of the microgrid crosses the grid voltage phasor at 0.0 deg. The delay in seconds between when the reclose is initiated to when the microgrid is reconnected is shown in Figure 5-21. The synchronous generator control mode is changed to power control mode after the synchronization.

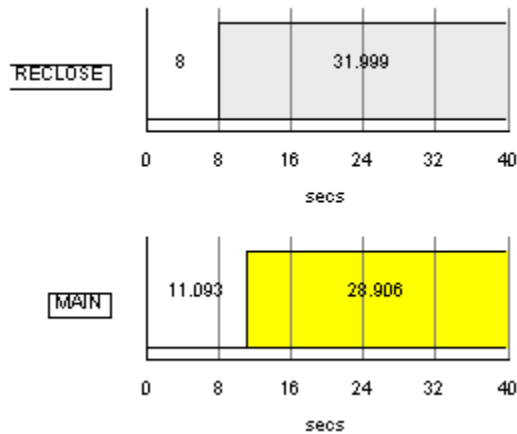
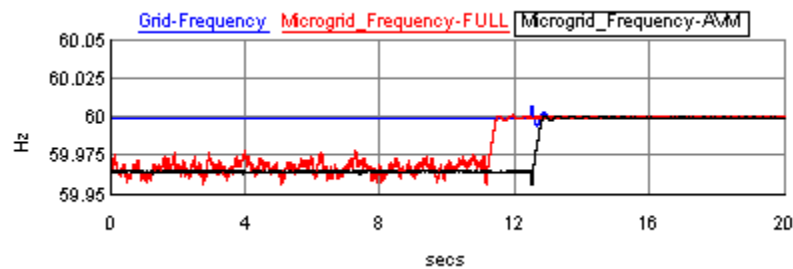


Figure 5-21 Reconnecting the microgrid with the grid

The microgrid frequency after reconnection to the grid is shown in Figure 5-22. The RE-CLOSE command is not synchronized between the microgrid simulation case using the Full and AVM VSC models so a time delay is seen between the two models. The frequency response is however similar for both models showing that the synchronization criteria has been met by the voltage balancing capacitors as well as the diesel generator governor action for isochronous frequency control. When the microgrid is reconnected, the breaker closed status is sent to the diesel generator to switch the governor back to droop control.



**Figure 5-22 Microgrid frequency synchronized to grid frequency power with the AVM(black) and FULL(red) VSC converter based models**

The total power from the grid, loads and DERs after reconnection to the microgrid is shown in Figure 5-23 for the AVM and Full VSC converter models. The total load increases due to increased voltage level, as the additional real and reactive power demand is mostly supplied by the utility grid. The response of both the AVM and FULL microgrid systems give close results after the microgrid is reconnected, the time difference is again due to the manual reclose command being issued earlier in the microgrid simulation with the Full VSC modeled compared to the AVM model.

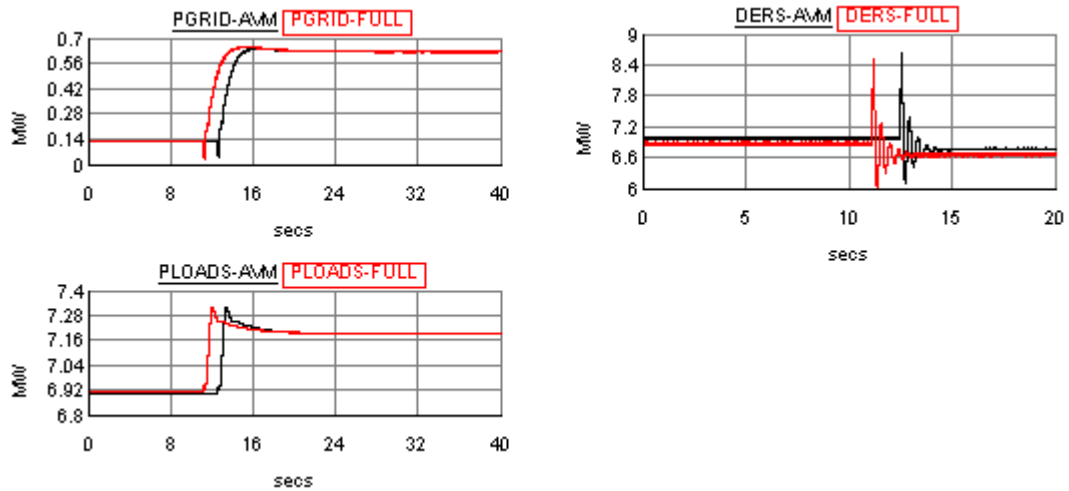


Figure 5-23 Grid, Load and DER power before and after resynchronization with the AVM(black) and FULL(red) VSC converter based models

## 5.6 Interfacing a Physical Relay with the Microgrid System

The reliable operation of microgrids requires protection systems with appropriate settings to detect fault conditions to avoid damage to equipment and abnormal operating conditions. The key benefit of real-time simulations is the ability to interface actual protection equipment with the simulated microgrid system in order to test their operation under realistic operating conditions. This section discusses interfacing a protection relay with the microgrid to perform hardware in the loop simulations. The simulation model with the detailed VSC representation was used in these simulations.

### 5.6.1 Interface between the microgrid model and the relay

Figure 5-24 shows the interface between the microgrid model and a physical micro-processor relay placed at bus 1 (B1). The bus voltages and line currents are scaled down and measured by using a voltage (potential) transformer (PT) with turns ratio of 2000 and a current transformer (CT) with a turns ratio of 100 respectively. The burden voltages and burden currents of the voltage and current transformer are then sent to the relay using a digital to analog converter (analogue output) card included as part of the RTDS hardware. The fault detection signal from the relay indicated by the relay contact operation is sent back to the simulated microgrid model using a digital input card where a logic 0 input indicates a relay trip operation and a logic 1 input indicates no relay operation. The fault detection signal can be used to operate the point of connection breaker or used to initiate some control action in the microgrid system.

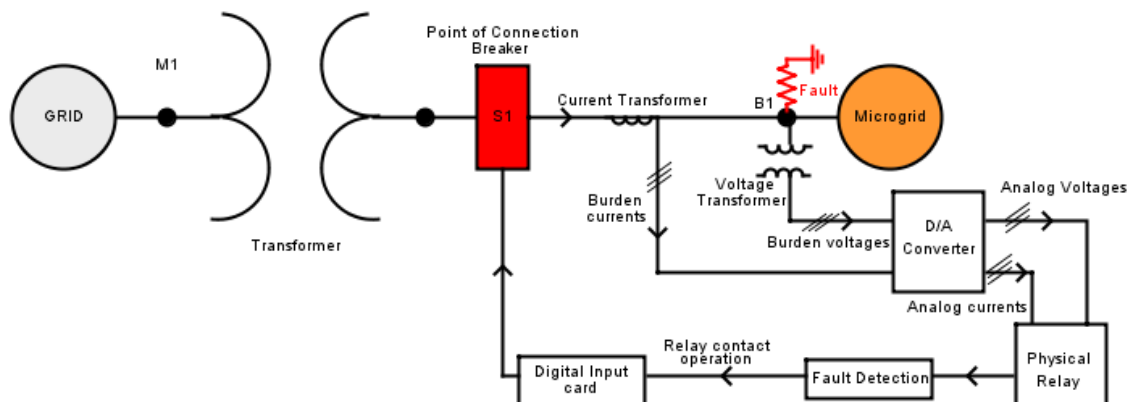


**Figure 5-24 Interface between Microgrid System and a Physical Relay**

Figures 5-25 and 5-26 compares the rms voltages and current magnitudes estimated by the relay and inside RTDS simulation. The small differences are due to errors in D/A and A/D conversion and the differences in the phasor estimation methods. If necessary, these can be calibrated inside the relay.

Main Voltage A:	7.568	kV	0	*	Main Voltage B:	7.525	kV	-120	*
Main Voltage C:	7.554	kV	120	*	Main Line Current A:	70.967	A	-75	*
Main Line Current B:	131.017	A	176	*	Main Line Current C:	112.179	A	25	*

**Figure 5-25 Measured primary RMS voltage and RMS current signals in the relay**

Voltage_A	Voltage_B	Voltage_C
7.584	7.546	7.557
Current_A	Current_B	Current_C
74.17	135.4	116.4

**Figure 5-26 Measured primary RMS voltage (kV) and RMS current (A) in the RTDS simulation**

Typically, micro-processor relays have multiple protection functions used to detect fault conditions and provide the fault detection (trip) signal using pre-defined settings. Commonly available protection functions include overcurrent, over/under voltage, over/under frequency, rate of change of frequency, distance and impedance elements. A major challenge in the protection of microgrids is the setting and co-ordination of these different protection functions when the microgrid operates in grid-connected or islanded operation. In this work, the ground overcurrent element of the relay was enabled to demonstrate the relay interface with the microgrid system. Figure 5-27 shows the required settings of the neutral overcurrent elements in the relay. The relay used in the experiment was actually a transmission line protection relay and comes with directional capability. However, directional function was not enabled as typical distribution protection relays are not directional.

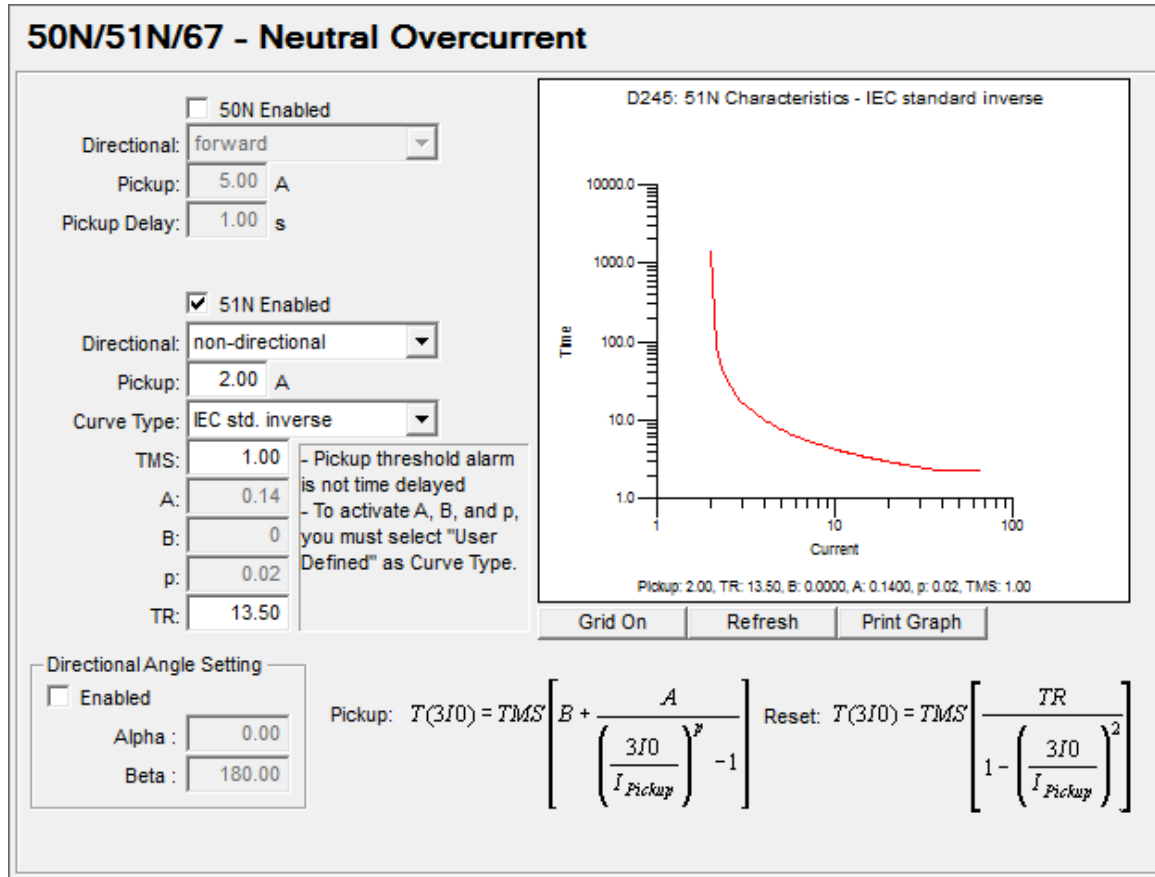


Figure 5-27 Overcurrent Element of Protection Relay

The ground/neutral overcurrent element detects the line to ground faults by measuring the zero sequence current and comparing it against a predetermined pickup current setting as given by [72]:

$$I_{pick\_up} = \frac{I_{nominal} * Unbalanced\ Factor}{Current\ Transformer\ Ratio} \quad (5.4)$$

Typical value for the unbalanced factor for distribution feeders is given as 0.3[72]. The time multiplier setting adjusts the relay operating time when the fault current is equal to or greater than the pick-up current to provide a discrimination margin to coordinate between other relay elements when enabled [72].

Figure 5-28 shows the fault current obtained when a  $0.1\Omega$ , single phase line to ground fault is applied at bus 1 with the microgrid in grid-connected mode.

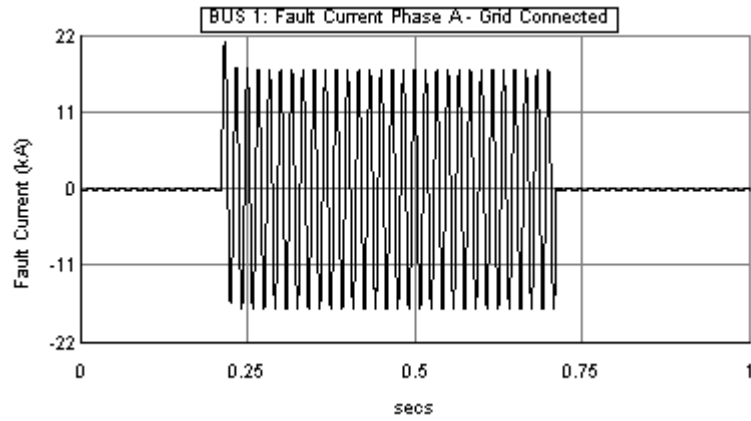


Figure 5-28 Grid Connected Mode: Phase A Line to Ground Fault Current

The overcurrent setting detects the fault and issues the trip signal after a time delay of  $\sim 0.11$  seconds as shown in Figure 5-29. The trip signal is received back in the RTDS via the digital input card in the hardware in the loop interface as shown in Figure 5-30. The CT currents observed in the relay and the RTDS simulation during the fault are shown in Figure 5-31 and Figure 5-32 respectively.

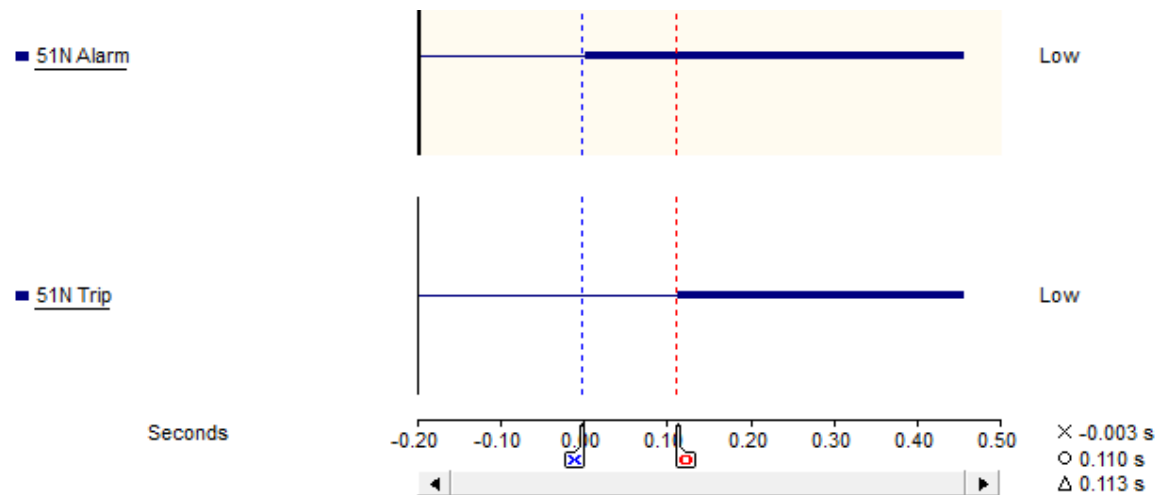


Figure 5-29 Fault Detection in Relay

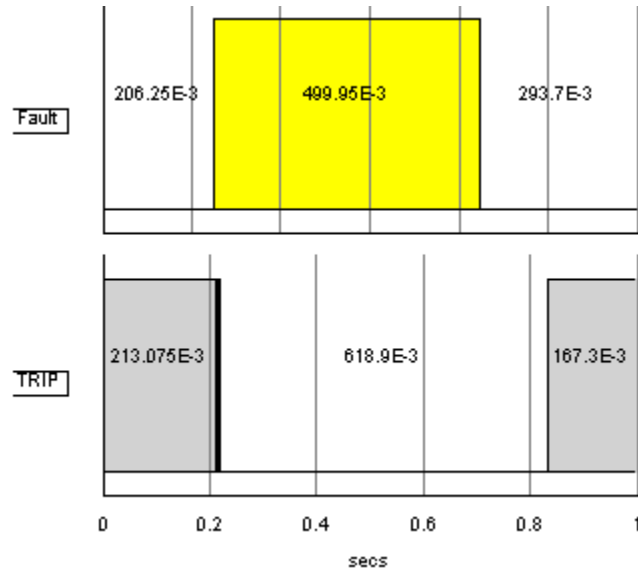


Figure 5-30 Fault and relay trip signal in simulated system grid connected operation

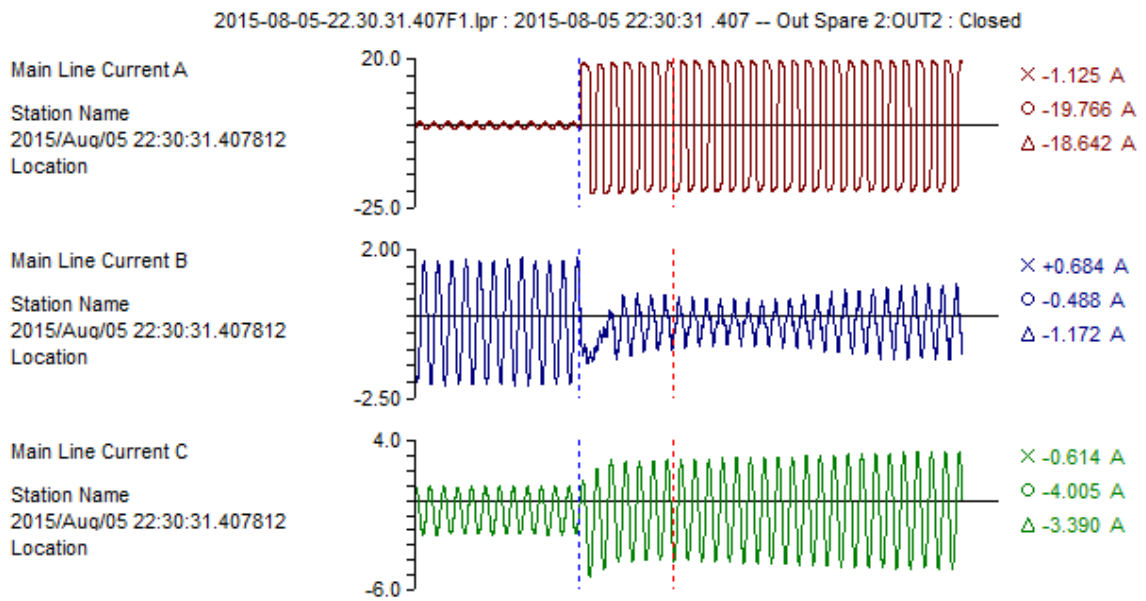
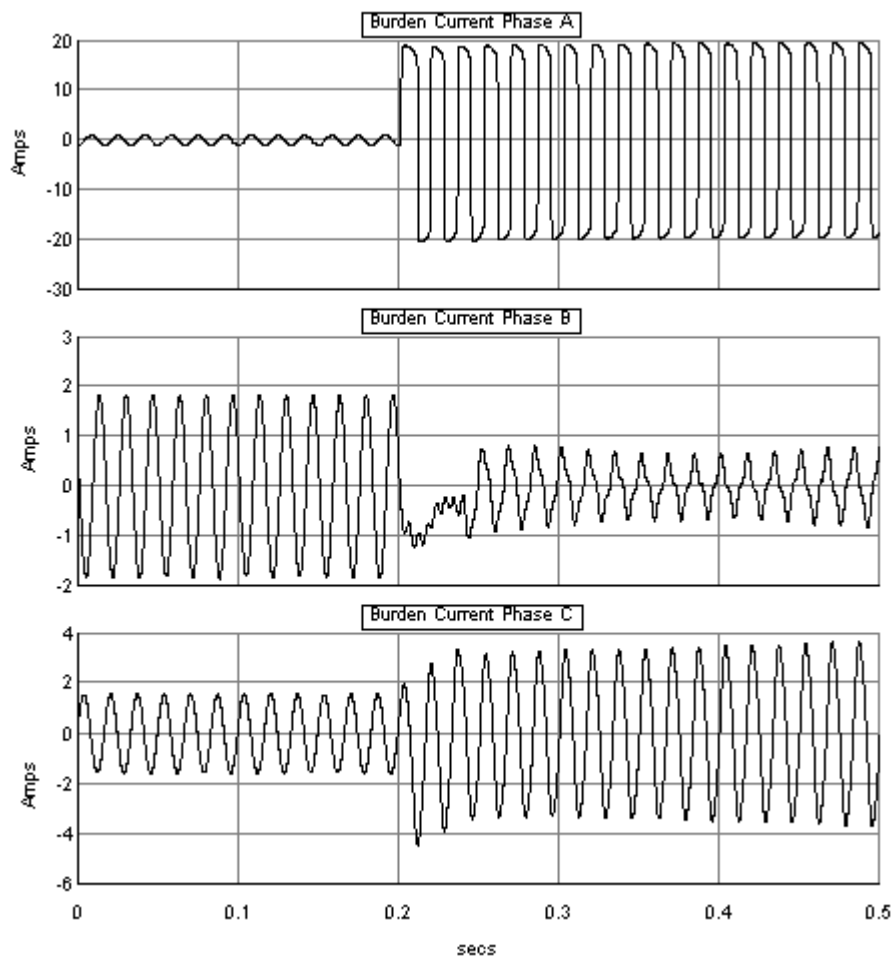


Figure 5-31 CT currents in the Relay



**Figure 5-32 CT currents in the RTDS**

Figure 5-33 shows a reduced fault current level when the microgrid is in islanded operation and a  $0.1\Omega$ , single phase line to ground fault is applied at bus 1. The overcurrent element does not detect the fault in the islanded microgrid as shown in Figure 5-34. A more sophisticated fault detection method or an adaptive overcurrent settings is required to ensure fault detection when the microgrid is in islanded mode. Future work will look into implementing a co-ordinated protection strategy to detect fault conditions when in the microgrid operates in both grid-connected and islanded mode.

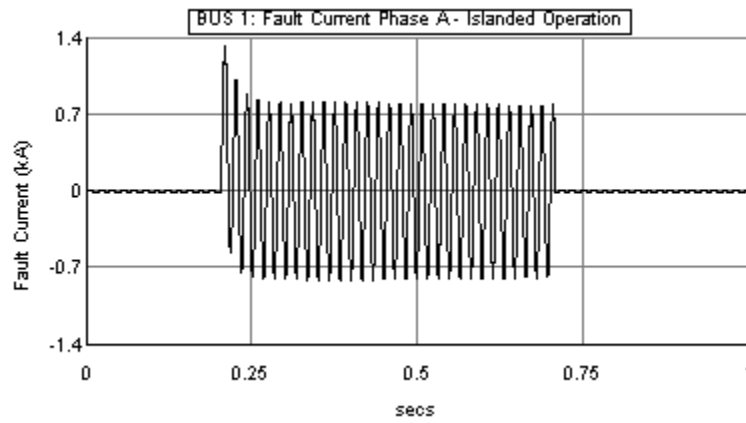


Figure 5-33 Fault Current - Islanded Mode

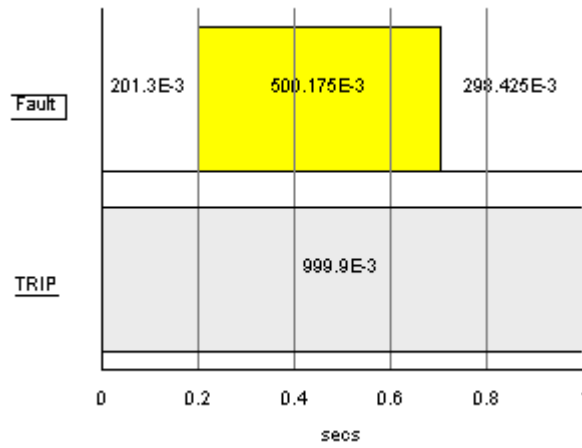


Figure 5-34 Fault and relay trip signal in islanded operation

## 5.7 Conclusions

A microgrid model based on the CIGRE North American medium voltage network was developed and simulated using the DERs discussed in Chapter 3. The operation of the load shedding control as well as the synchronization of the microgrid using voltage balancing capacitors was demonstrated. The response of the microgrid was compared for several transient scenarios using the AVM and FULL VSC models of the Solar and DFIG system and similar results were obtained with slight differences in the transient voltage and fault currents due to the approximations used in the AVMs and the modeling representation of the VSC models in the small time step. This chapter showed that the AVM model reduced the hardware resources required to simulate the Full VSC models. The AVM model is sufficient for real-time simulation of large distribution networks with limited hardware resources. In this chapter, the advantage of real time digital simulation to interface actual microgrid protection and control hardware to test their operation under different fault conditions was demonstrated by a hardware in the loop simulation with a protection relay.

# Chapter 6

## Conclusions and Future Work

### 6.1 Conclusions

The following conclusions are drawn from the work carried out in this thesis

- An understanding of microgrid concepts, the technical issues related to microgrid implementation, and simulation tools used for microgrid studies was achieved by a comprehensive literature review. The advantage of using real-time simulation tools for microgrid studies to allow for hardware in the loop testing of microgrid protection and control devices was established.
- A real-time simulation model of a microgrid based on the CIGRE bench mark MV North American distribution network was developed on the RTDS simulator. Short three-phase overhead distribution line segments in the network were represented using coupled pi networks. Implementation of large distribution networks with many nodes in a real-time simulator is challenging as it is nearly impossible to di-

vide the network into subsystems due to short distribution line lengths. The structure of the microgrid was reduced from an 11 bus network to a 7 bus network by combining transmission lines to meet the node requirements.

- The microgrid included three types of DERs namely a solar PV generator, a DFIG driven by a wind turbine, and a synchronous generator driven by a diesel engine. Real time simulation models of the individual DERs were developed, accuracy was validated and the hardware requirements were determined. The implementation of the converter based DERs namely the PV and wind generators using detailed model with small time step simulations requires a considerable amount of hardware resources to represent the high switching frequency dynamics of their voltage source converters.
- The simulation models of the VSCs of the wind and PV system were implemented using the average-value modelling (AVM) technique in the dq reference frame to reduce the required hardware resources. The simulation results obtained with the average models were compared with those obtained with fully switched converter models under variety of situations. The results indicate the results obtained with average models are adequate for most purposes. However, some differences were observed in the transient response of the two models due to the approximations made in using the AVM and the small time step simulation approach used in the RTDS. The AVM is shown to be sufficient when AC side dynamics of DERs are considered.

- The operation of the microgrid in grid-connected and islanded mode was analyzed by simulating several transient events such as islanding and resynchronization of the microgrid. A load shedding scheme to achieve power balance during islanded operation and a switched capacitor bank to balance and control the voltages to enable resynchronization of the microgrid after an islanding event were implemented in the microgrid simulation model. Correct operation of the microgrid with the implemented control was successfully demonstrated by simulating a number of islanding, synchronization and fault events. The simulation model using the AVM and Full converter models gave similar results and behaved as expected.
- The developed real-time microgrid simulation model was interfaced to a protection relay in a hardware in the loop simulation. It was demonstrated that the protection relay operates differently due to differences in fault currents when the microgrid is in grid-connected and islanded operation. Advanced protection techniques are required for microgrid operation in grid-connected and islanded mode.

## 6.2 Future Work

- The logical next step is to use the developed real-time microgrid simulation model to investigate various issues related to advanced protection and control of microgrids. Main advantage of real-time simulations is the ability of testing actual protection and control devices using hardware in the loop simulations.

- In this research the role of the diesel generators in the microgrid is to control the frequency during islanding due to the high mechanical inertia of the synchronous machine. However, practical diesel generators require regular transportation of diesel fuels which might be difficult to access in remote/rural based microgrids. In addition, the combustion of the diesel fuel causes surrounding pollution compared to the renewable PV and wind DERs as shown in Figure 6-1. The simulation model can be enhanced to include new elements such as energy storage to study the operation and control of microgrids with only converter based DERs using battery energy storage systems for voltage and frequency control during islanding operation.



**Figure 6-1 Diesel Generator with associated pollution (blackened walls)**

## References

- [1] CIGRE C6.04.02 Task Force, "Benchmark Modeling and Simulation for Analysis, Design and Validation of Distributed Energy Resources," September 2006.
- [2] Wikipedia, "Distributed generation," 26 March 2014. [Online]. Available: [http://en.wikipedia.org/w/index.php?title=Distributed\\_generation&oldid=601399313](http://en.wikipedia.org/w/index.php?title=Distributed_generation&oldid=601399313). [Accessed 29 May 2014].
- [3] K. Stefferud, "Post #7: Microgrid Benefits and Challenges," EnerNex: Electric power research, engineering and consulting, 28 August 2013. [Online]. Available: <http://www.enernex.com/blog/post-7-microgrid-benefits-and-challenges/>. [Accessed 6 September 2014].
- [4] C. Abbey, D. Cornforth, N. Hatziargyriou, K. Hirose, A. Kwasinski, E. Kyriakides, G. Platt, L. Reyes and S. Suryanarayanan, "Powering Through the Storm: Microgrids Operation for More Efficient Disaster Recovery," *Power and Energy Magazine, IEEE*, vol. 12, no. 3, pp. pp.67,76, May-June 2014.
- [5] K. Strunz, "Developing benchmark models for studying the integration of distributed energy resources," in *Power Engineering Society General Meeting, 2006. IEEE*, Montreal, Que., 2006.
- [6] L. Arachchige and A. Rajapakse, "Voltage balancing and synchronization of microgrids with highly unbalanced loads," *Renewable and Sustainable Energy Reviews*, vol. 31, pp. 907-920, March 2014.
- [7] R. A. Walling and N. W. Miller, "Distributed generation islanding-implications on power system dynamic performance," in *Power Engineering Society Summer Meeting, 2002 IEEE (Volume:1)*, Chicago, IL, USA, 25-25 July 2002.
- [8] R. H. Lasseter, "Microgrids [distributed power generation]," in *Power Engineering Society Winter Meeting, 2001. IEEE (Volume:1)*, Columbus, OH, 28 Jan 2001-01 Feb 2001.

- [9] N.W.A Lidula and A. Rajapakse, "Microgrids research: A review of experimental microgrids and test systems," *Renewable and Sustainable Energy Reviews*, vol. 15, no. 1, pp. 186-202, 2010..
- [10] R. Majumder, "Modeling, stability analysis and control of microgrid," 2010.
- [11] S. Chowdhury , S. Chowdhury and P. Crossley, *Microgrids and Active Distribution Networks*, London: The Institution of Energy and Technology, 2009.
- [12] H.-J. Liu, Y. Sun, Z.-Y. Zou and L. Niu, "Control Methods and Simulations of Microgrid," in *Electronics and Signal Processing*, Springer, 2011, pp. 1023-1030.
- [13] C. Trujillo, D. Velasco, E. Figueres and G. Garcera, "Local and Remote Techniques for Islanding," [Online]. Available: <http://cdn.intechopen.com/pdfs-wm/10136.pdf>.
- [14] S. M. Sharkh, M. A. Abusara, G. I. Orfanoudakis and B. Hussain, *Power Electronic Converters for Microgrids*, Singapore: Wiley, 2014.
- [15] "IEEE Standard for Interconnecting Distributed Resources with Electric Power Systems," *IEEE Std 1547-2003*, pp. 1,28, July 28 2003.
- [16] F. Katiraei, "Computer simulation modeling and analysis of the dynamic behaviour of a reciprocating engine based distributed generation unit during islanding transition," Natural Resources Canada, Devon-Ottawa-Varenes, August 2007.
- [17] P. Mahat, Z. Chen and B. Bak-Jensen, "Review of islanding detection methods for distributed generation," in *Electric Utility Deregulation and Restructuring and Power Technologies, 2008. DRPT 2008. Third International Conference on*, Nanjing, 2008.
- [18] S. S. Madani, A. Abbaspour, M. Beiraghi, P. Z. Dehkordhi and A. M. Ranjbar, "Islanding detection for PV and DFIG using decision tree and AdaBoost algorithm," in *Innovative Smart Grid Technologies (ISGT Europe), 2012 3rd IEEE PES International Conference and Exhibition on*, Berlin, Oct. 2012.

- [19] C. Trujillo, D. Velasco, E. Figueres and G. Garcera, "Local and Remote Techniques for Islanding," [Online]. Available: <http://cdn.intechopen.com/pdfs-wm/10136.pdf>.
- [20] E. Muljadi, T. Batan, D. Yildirim and C. Butterfield, "Understanding the unbalanced voltage problem in wind turbine generation," in *Industry Applications Conference, 1999. Thirty-Fourth IAS Annual Meeting. Conference Record of the 1999 IEEE (Volume:2)*, Phoenix Arizona, 1999.
- [21] P. Pillay and M. Manyage, "Definitions of Voltage Unbalance," *Power Engineering Review, IEEE (Volume:21, Issue: 5)*, vol. 21, no. 5, pp. 49-51, May 2001.
- [22] "1547.2-2008 - IEEE Application Guide for IEEE Std 1547(TM), IEEE Standard for Interconnecting Distributed Resources with Electric Power Systems," pp. 1-217, 2009.
- [23] A. Ellis, R. Nelson, E. V. Engeln, R. Walling, J. McDowell, L. Casey, E. Seymour, W. Peter, C. Barker and B. Kirby, "Reactive Power Interconnection Requirements for PV and Wind Plants-Recommendations to NERC," Sandia National Laboratories, February 2012.
- [24] K. Turitsyn, P. Sulc, S. Backhaus and M. Chertkov, "Options for Control of Reactive Power by Distributed Photovoltaic Generators," *Proceedings of the IEEE*, vol. 99, no. 6, pp. 1063 - 1073, June 2011.
- [25] L. Huijuan, Y. Xu, S. Adhikari, R. D. Tom, F. Li and P. Irminger, "Real and Reactive Power Control of a Three-Phase Single Stage PV System and PV Voltage Stability," in *Power and Energy Society General Meeting, 2012 IEEE*, San Diego, CA, 22-26 July 2012.
- [26] M. Illinadala and G. Venkataramana, "Control of Distributed Generation Systems to Mitigate Load and Line Imbalances," in *Power Electronics Specialists Conference, 2002. pesc 02. 2002 IEEE 33rd Annual*, Cairns, Qld., 2002.

- [27] B. Bhandari, S. Poudel, K.-T. Lee and S.-H. Ahn, "Mathematical modeling of hybrid renewable energy system: A review on small hydro-solar-wind power generation," *International Journal of Precision Engineering and Manufacturing-Green Technology*, vol. 1, no. 2, pp. 157-173, 2014.
- [28] L. Zhang, N. Gari and L. V. Hmurcik, "Energy management in a microgrid with distributed energy resources," *Energy Conversion and Management*, vol. 7, pp. 297-305, 2014.
- [29] A. Rajapakse and D. Muthumuni, "Simulation tools for photovoltaic system grid integration studies," in *Electrical Power & Energy Conference, 2009 IEEE*, Montreal, 2009.
- [30] H. B. Sun, X. R. Song and C. L. Li, "Dynamic modeling of a hybrid wind/solar/hydro microgrid in EMTP/ATP," *Renewable Energy*, vol. 39, no. 1, pp. 96-106, March 2012.
- [31] R. Technologies, *RTDS Manuals and Documentation*, Winnipeg, 2009.
- [32] J. Arrillaga and N. Watson, *Power Systems Electromagnetic Transients Simulation*, London, United Kingdom: Institution of Engineering and Technology, 2007.
- [33] M. Mauri, "Hardware in the loop simulation of renewable distributed generation systems," 2009 December 2009. [Online]. Available: <http://www.intechopen.com/books/renewable-energy/hardware-in-the-loop-simulation-of-renewable-distributed-generation-systems>.
- [34] I. K. Park, P. Forsyth, R. Kuffel and E. Tara, "Hardware in the Loop (HILS) testing of a power electronics controller with RTDS," in *IECON 2013 - 39th Annual Conference of the IEEE Industrial Electronics Society*, Vienna, Nov 2013
- [35] J. Jin-Hong, K. Jong-Yul, K. Seul-Ki and A. Ong-Bo, "Development of HILS(Hardware in-Loop Simulation) system for MMS (Microgrid Management System) by using RTDS," in *Power Electronics and Motion Control Conference, 2008. EPE-PEMC 2008. 13th*, Poznan, 1-3 Sept. 2008

- [36] E. d. Jong , R. d. Graaf, P. Vaessen, P. Crolla, A. Roscoe, F. Lehfab, G. Lauss, P. Kotsampopoulos and F. Gafaro, "European White Book on Real-Time Powerhardware-in-the-Loop testing," European Distributed Energy Resources Laboratories, Arnhem Netherlands, 2011-12.
- [37] G. Joos, B.-T. Ooi, D. T. McGillis, F. D. Galiana and R. J. Marceau, "The potential of distributed generation to provide ancillary services," in *Power Engineering Society Summer Meeting, 2000. IEEE*, Seattle, WA, 2000.
- [38] S. Krishnamurthy, T. Jahns and R. Lasseter, "The operation of diesel gensets in a CERTS microgrid," in *Power and Energy Society General Meeting - Conversion and Delivery of Electrical Energy in the 21st Century, 2008 IEEE*, Pittsburgh, PA, 20-24 July 2008.
- [39] P. Kundur, *Power System Stability and Control*, New York: McGraw-Hill, 1994.
- [40] Wikipedia, the free encyclopedia, "Diesel Engine," Wikipedia, 9 April 2015. [Online]. Available: [http://en.wikipedia.org/wiki/Diesel\\_engine#Major\\_advantages](http://en.wikipedia.org/wiki/Diesel_engine#Major_advantages). [Accessed 13 April 2015].
- [41] L. Lansky, "Diesel engine modelling and control," MSc thesis. Department of Control Engineering. Czech Technical University in Prague, 2008.
- [42] S. Roy, O. Malik and G. Hope, "A low order computer model for adaptive speed control of diesel driven power plants," in *Industry Applications Society Annual Meeting, 1991., Conference Record of the 1991 IEEE* , Dearborn, MI, USA , Sept. 28 1991-Oct. 4 1991 .
- [43] D. Augustine and K. Kumar, "A method for self-tuning a PID controller for control of small to medium sized diesel engines," in *Systems Engineering, 1991., IEEE International Conference on* , Dayton, OH, USA , 1-3 Aug. 1993
- [44] H. Saadat, *Power System Analysis*, Milwaukee: McGraw-Hill, 2002.
- [45] "IEEE Recommended Practise for Excitation System Models for Power System Stability Studies," *IEEE Std 421.5-2005 (Revision of IEEE Std 421.5-1992)*, vol. 0, pp. 0\_1-85, 2006

- [46] J. Rogers and L. Wisland, "Solar Power on the Rise: The Technologies and Policies behind a Booming Energy Sector," 07 08 2014. [Online]. Available: [http://www.ucsusa.org/assets/documents/clean\\_energy/Solar-Power-on-the-Rise.pdf](http://www.ucsusa.org/assets/documents/clean_energy/Solar-Power-on-the-Rise.pdf). [Accessed 13 09 2014].
- [47] Wikipedia , "List of semiconductor materials," 7 April 2015. [Online]. Available: [http://en.wikipedia.org/wiki/List\\_of\\_semiconductor\\_materials](http://en.wikipedia.org/wiki/List_of_semiconductor_materials). [Accessed 20 April 2015].
- [48] ENERGY INFORMATIVE THE HOMEOWNER'S GUIDE TO SOLAR PANELS, "Solar Cell Comparison Chart - Mono-Polycrystalline and Thin Film," ENERGY INFORMATIVE, 2015. [Online]. Available: <http://energyinformative.org/solar-cell-comparison-chart-mono-polycrystalline-thin-film/>. [Accessed 20 April 2015].
- [49] Wikipedia The Free Encyclopedia, "Solar Car," Wikipedia, 4 April 2015. [Online]. Available: [http://en.wikipedia.org/wiki/Solar\\_car](http://en.wikipedia.org/wiki/Solar_car). [Accessed 20 April 2015].
- [50] M. G. Villalva, J. R. Gazoli and E. R. Filho, "Comprehensive Approach to Modeling and Simulation of Photovoltaic Arrays," *IEEE Transactions on Power Electronics*, vol. 24, no. 5, pp. 1198-1208, May 2009.
- [51] C. Honsberg and S. Bowden, "<http://pveducation.org/>," 3 28 2013. [Online]. [Accessed 01 Jan 2014].
- [52] D. S. Chan and J. C. Phang, "Analytical Methods for the Extraction of Solar-Cell Single-and Double-Diode Model Parameters from I-V Characteristics," *IEEE Transactions on Electronic Devices*, vol. 34, no. 2, pp. 286-293, February 1987.
- [53] R. Khezzar, M. Zereg and A. Khezzar, "Comparative Study of Mathematical Methods for Parameters Calculation of Current-Voltage Characteristics of Photovoltaic Module," in *International Conference on Electrical and Electronics Engineering 2009. ELECO 2009*, Bursa, 2009.
- [54] Z. Yongli, Y. JianGuo and W. Di, "Comparative study of two stages and single stage topologies for grid-tie photovoltaic generation by PSCAD/EMTDC," in *International Conference on Advanced Power System Automation and Protection (APAP) 2011.*, Beijeng, 16-20 Oct 2011.

- [55] A. Yazdani and R. Iravani, *Voltage-Sourced Converters in Power Systems: Modeling, Control, and Applications*, New Jersey: Wiley-IEEE Press, 2010.
- [56] A. Yazdani, A. R. D. Fazio, H. Ghoddami, M. Russo, M. Kazerani, J. Jatskevich, K. Strunz, S. Leva and J. A. Martinez, "Modeling Guidelines and a Benchmark for Power System Simulation Studies of Three-Phase Single-Stage Photovoltaic Systems," *IEEE Transactions on Power Delivery*, vol. 26, no. 2, pp. 1247-1264, 24 March 2011.
- [57] B. Wu, Y. Lang, N. Zargari and S. Kouro, *Power Conversion and Control of Wind Energy Systems*, Wiley-IEEE Press, 2011.
- [58] A. Yazdani and P. P. Dash, "A Control Methodology and Characterization of Dynamics for a Photovoltaic (PV) System Interfaced With a Distribution Network," *IEEE Transactions on Power Delivery*, vol. 24, no. 3, pp. 1538-1551, 2009.
- [59] A. Hava, U. Ayhan and V. Aban, "A DC bus capacitor design method for various inverter applications," in *Energy Conversion Congress and Exposition (ECCE), 2012 IEEE*, Raleigh, NC, 15-20 Sept 2012.
- [60] T. Esram and P. L. Chapman, "Comparison of Photovoltaic Array Maximum Power Point Tracking Techniques," *IEEE Transactions on Energy Conversion*, vol. 22, no. 2, pp. 439-449, June 2007.
- [61] G. Farivar, B. Asaei and S. Mehranmi, "An Analytical Solution for Tracking Photovoltaic Module MPP," *IEEE Journal of Photovoltaics*, vol. 3, no. 3, pp. 1053-1061, July 2013.
- [62] B. Ankaiah and J. Nageswararao, "MPPT Algorithm for Solar Photovoltaic Cell by Incremental Conductance Algorithm," *International Journal of Innovations in Engineering and Technology (IJJET)*, vol. 2, no. 1, pp. 17-23, February 2013.
- [63] H. Siegfried, *Grid Integration of Wind Energy Conversion Systems*, John Wiley & Sons, 1998.
- [64] P. Parlados, P. Rebennack, S. Pereira, N. Illiadis and N. Pappu, *Handbook of Wind Power Systems*, Springer, 2013.

- [65] O. Anaya-Lara, Z. Liu, G. Quinonez-Varela and J. R. McDonald, "Optimal DFIG crowbar resistor design under different controllers during grid faults," in *Third International Conference on Electric Utility Deregulation and Restructuring and Power Technologies.*, Nanjing, 6-9 April 2008.
- [66] W. Qiao, "Chapter 28: Power Electronics for Renewable Energy," in *The Electric Power Engineering Handbook: Power Systems 3rd Edition*, CRC Press, 2012.
- [67] R. Pena, J. Clare and G. Asher, "Doubly fed induction generator using back-to-back PWM converters and its application of variable-speed wind-energy generation," *Electric Power Applications, IEEE Proceedings*, vol. 143, no. 3, pp. 231-241, 1996.
- [68] H. J. Wagner and J. Mathur, *Introduction of Wind Energy Systems: Basics, Technology and Operation*, G. E. a. Technology, Ed., Springer, 2013.
- [69] J. S. Thongnam and M. Ouhrouche, "MPPT Control Methods in Wind Energy Conversion Systems," [Online]. Available: <http://cdn.intechopen.com/pdfs-wm/16255.pdf>. [Accessed 2014].
- [70] J. Peralta, H. Saad, S. Denetiere and J. Mahseredjian, "Dynamic Performance of Average-Value Models for Multi-terminal VSC-HVDC Systems," in *Power and Energy Society General Meeting, 2012 IEEE*, San Diego, CA, 22-26 July 2012.
- [71] N. Lidula, A. Rajapakse and D. Muthumuni, "Implementation, Comparison and Application of an Average Simulation Model of a Wind Turbine Drive Doubly Fed Induction Generator".
- [72] A. Rajapakse, "ECE 24.7060: Power System Protection Class Notes - Chapter 7 OverCurrent Protection," Winnipeg, Fall 2010.